

Self-Supporting Straw Tube Detectors for the COSY-TOF and PANDA Experiments

Sedigheh Jowzaee

Dissertation for Doctor of Philosophy Degree

Prepared at the Institute of Physics of the Jagiellonian University, Poland
and the Institute of Kernphysik of the Jülich Research Center, Germany

Faculty of Physics, Astronomy and Computer Science
Jagiellonian University

October 2014

Accepted by the Faculty of Physics, Astronomy and Computer Science of Jagiellonian University.

International PhD program coordinator: Prof. Dr. Pawel Moskal
Scientific adviser: Prof. Dr. Jerzy Smyrski

Abstract

Self-supporting straw tube detectors, which were developed for the COSY-TOF experiment, will be also used for tracking charged particles in the PANDA experiment. We investigate the applicability of the PANDA straw tube tracker for identification of protons, charged pions and kaons based on the energy loss information. For this aim, the Garfield program is used to simulate straw tube signals which are convoluted with the transfer function of the front-end electronics. The energy losses in the straw tubes are determined using the information about the Time Over Threshold (TOT) of the straw tube signals and, independently, about the integrated charge of the signals. The separation powers of protons, charged pions and kaons based on the TOT and the integrated charge are comparable and exceed a 5σ level for particle momenta below $0.6 \text{ GeV}/c$ as required for PANDA. We simulate also the gas gain in the straw tubes with the Magboltz and Garfield program. The experimental results for the gain are reproduced after adding 34% Penning transfer rate in the simulation.

The straw tube tracker performance is also studied in the COSY-TOF experiment with analysis of the data for the $\vec{p}p \rightarrow pK^+\Lambda$ reaction measured with a proton beam at $2.95 \text{ GeV}/c$ momentum. The polarization of the beam is determined to be about 87% by analysis the pp elastic scattering events. The analysis using only the straw tube tracker information shows a high reconstruction efficiency of 20% for the $pK^+\Lambda$ events and the $p\Lambda$ invariant mass resolution of $1 \text{ MeV}/c^2$. The angular distributions of protons, kaons and Λ -hyperons are determined in the CMS and are fit with the Legendre polynomials. The fitting coefficients show that both S and D-wave contributions are dominant for the proton distribution, whereas in the Λ distribution all S, P and D-waves are significant. The Dalitz plot with the selected $pK^+\Lambda$ events shows significant enhancements due to the $p\Lambda$ -FSI and the $N\Sigma$ cusp effect. The $N\Sigma$ cusp is stronger in the region of the Dalitz plot with the Helicity angle $\cos\theta_{pK}^{Rp\Lambda} \leq -0.33$, and its angular distribution has a dominant S-wave contribution. The angular distribution of the analyzing power of the proton, kaon and Λ -hyperon is also determined and fit with the associated Legendre polynomials. In the CMS the distributions are more symmetric for the proton compared to kaon and Λ -hyperon. The (S,P)-wave interference contribution to the kaon analyzing power is determined to be about 0.04 at low $p\Lambda$ invariant mass, and it can be used to extract the $p\Lambda$ spin triplet scattering length.

Contents

Introduction	1
1 The PANDA Experiment	5
1.1 The FAIR Accelerator Complex	5
1.2 The PANDA Physics Program	6
1.3 PANDA Detector	8
1.3.1 Target Systems	10
1.3.2 Tracking Systems	10
1.3.3 Particle Identification Systems	13
1.3.4 Electromagnetic Calorimeter	14
1.4 PANDA Straw Tube Tracker (STT)	14
1.4.1 Self-Supporting Straw Tube Detectors	14
1.4.2 Central Straw Tube Tracker	17
1.4.3 Forward Tracker	19
1.4.4 Readout Electronics	20
2 Physics of Straw Tube Detectors	23
2.1 Ionization Process in Gases	24
2.2 Drift of Electrons and Ions in Gases	26
2.3 Gas Amplification	30
2.4 Signal Creation	32
2.5 Operating Gas Mixture	34
3 Simulation of the Straw Tube Detector Performance	37
3.1 Garfield Program	37
3.2 Detector Geometry	37
3.3 Electric and Magnetic Field Geometry	38
3.4 Transport Properties of Electrons and Ions Calculated with Magboltz	39
3.4.1 Ionization and Excitation Rates	41
3.4.2 Drift Velocity of Electrons and Ions in the Straw Tubes	41
3.4.3 Effect of the Magnetic Field on the Drift	43

3.4.4	Diffusion of Electrons	43
3.5	Simulation of Gas Multiplication	45
3.5.1	Townsend and Attachment Coefficients	45
3.5.2	The Penning Effect	46
3.5.3	Gain Simulation	48
4	Particles Identification with Straw Tube Detector	51
4.1	Cluster Statistics	51
4.2	Simulation of Straw Tube Output Signal	51
4.3	Convolved Signal and Transfer Function	53
4.4	Particle Identification Methods	54
4.4.1	Track to Wire Distance Correction	54
4.4.2	TOT in a Single Straw and Truncated Mean	55
4.5	Prototype Straw Tube Detector	58
4.6	Efficiency of TOT Measurement	60
4.7	$p - K - \pi$ Separation Power	61
5	The COSY-TOF Experiment	65
5.1	The COSY Facility	65
5.2	COSY-TOF Physics Program	67
5.3	COSY-TOF Detector	67
5.3.1	Start Detector	69
5.3.2	Stop Detectors	69
5.3.3	Tracking Detectors	70
5.3.4	COSY-TOF Straw Tube Tracker	71
6	Calibration of the COSY-TOF Straw Tube Tracker	75
6.1	TDC Time Correction	75
6.1.1	First Hit Selection	75
6.1.2	Signal Width Cut	76
6.1.3	Electronics Offset Correction	79
6.2	Calibration of Drift Time to Distance	82
6.2.1	“Self Calibration” Method	82
6.2.2	“Autocalibration” Method	83
6.3	Mean Residual of the STT	86
6.4	Calibration of the Straw Geometry	88
6.4.1	Calibration of the Double Layer Positions	88
6.4.2	Calibration of the Double Layer Rotations	90
6.5	Spatial Resolution of the STT	92

7	Analysis of pp Elastic Scattering and $\vec{p}p \rightarrow pK^+\Lambda$ with COSY-TOF STT Data	95
7.1	pp Elastic Scattering Analysis	96
7.1.1	pp Elastic Events Selection	96
7.1.2	Beam Direction Measurement	99
7.1.3	Vertex and Target Measurement	100
7.1.4	Beam Polarization	103
7.2	$\vec{p}p \rightarrow pK^+\Lambda$ Analysis	105
7.2.1	$pK^+\Lambda$ Event Selection	106
7.2.2	Reconstruction Efficiency and Precision	109
7.2.3	Physical Observables	113
	Summary and Outlook	135
	Appendices	139
	Acronyms	151
	Bibliography	153

Introduction

Invention of multiwire proportional chambers and drift chambers by Georges Charpak in 1968 at the European Organization for Nuclear Research (CERN) [1] revolutionized the particle tracking in the high energy physics experiments, because of the high rate capability of the chambers and their readout electronics allowing an online transfer of the measured data to computer. In the multiwire proportional chambers the arrays of anode wires placed between cathode planes are used to measure the position of charged particle tracks with a position resolution in the order of 1-2 mm which is a typical distance between the wires. In the drift chambers the position resolution is enhanced to about 0.1 mm by measurement of the drift time of the ionization electrons to the anode wire. The drift chambers can be used to build tracking systems with large active areas in the order of many squared meters and their readout requires relatively low number of electronic channels.

Straw tube detectors are a special type of the drift detectors. In these detectors, cathode wires are replaced by cylindrical tubes called “straws” which are typically made of plastic foil covered by conductive layer. The straw tube detectors provide high reliability due to the fact that a broken anode wire affects only a single straw and not a large part, or the whole detector as it can happen in the multiwire drift chambers. The straw tube detectors are used in many nuclear and particle physics experiments. The straws can be arranged in cylindrical layers as in the ATLAS TRT Barrel Detector [2] or in planar layers as in the LHCb Outer Tracker [3].

Typically, straw tube trackers require massive frames to provide the mechanical stability of the straw tubes and to support the anode wires tension. The COSY-TOF collaboration at the Jülich Research Center developed self-supporting straw tube detectors in which the wire tension and the stiffness of the straw tube is maintained by the gas overpressure of about 1 bar.

The self-supporting straw tube detectors are also proposed for the central and forward straw tube trackers of the PANDA experiment. PANDA is a large detector system which is being designed for experiments with antiproton beams at the future FAIR accelerator complex near Darmstadt, Germany. The high precision and high luminosity antiproton beam from FAIR

will allow PANDA to cover different research areas in the charmonium mass range such as the charmonium spectroscopy or a search for glueballs and hybrids. The PANDA straw tube trackers require a high counting rate capability and should provide particle identification based on the information about the energy losses of charged particles.

In the present work, the performance of the straw tubes in the PANDA experiment is simulated using the Garfield program. Separation of protons, charged pions and kaons based on measurement of the Time Over Threshold (TOT) of the straw tube signals is studied and is compared with corresponding results for measurement of integrated charges of the signals. The particle identification using the TOT information is more desirable since the required readout electronics for the time measurement is simpler compared to the electronics for measurement of the signal integral.

Because the PANDA detector is still in the construction phase, the performance of the self-supporting straw tubes is investigated at the COSY-TOF detector. The COSY-TOF experiment is mainly devoted to the measurement of the strangeness production in the proton-proton collisions in order to learn about the production mechanism and in particular about the role of N^* resonances in the strangeness production. In the present work, the data for the strangeness production in the $\bar{p}p \rightarrow pK^+\Lambda$ reaction measured with a polarized proton beam at 2.9 GeV/ c momentum is analyzed. The reconstruction of the $pK^+\Lambda$ events is done exclusively with the straw tube tracker.

In Chapter 1 of this thesis, an overview of the FAIR complex is presented and the PANDA experiment is described with focusing on the straw tube trackers.

The physics of straw tube detectors is discussed in Chapter 2 including details about the gas ionization process, drift of electrons and ions in gases and the signal creation in the detector.

Simulations of basic physical quantities in the straw tube detectors including the drift velocity of electrons, the attachment and Townsend coefficients are presented in Chapter 3, and in Chapter 4 results of simulation of the separation power for protons, pions and kaons are described.

In Chapter 5 the COSY-TOF experiment is described and the detector components are presented with emphasis on the straw tube tracker.

Chapter 6 explains the straw tube tracker calibration process in order to determine the drift time to isochrone radius $r(t)$ curve and the spatial resolution of the straw tube double layers.

Chapter 7 presents the analysis of the pp elastic scattering events which are used to determine the properties of the beam and the target dimensions. Then, the analysis of the $\bar{p}p \rightarrow pK^+\Lambda$ events is explained with presenting

the applied selection criteria of the events. The reconstruction efficiency and detector acceptance are determined by Monte Carlo simulations. Furthermore, the analysis of the angular distributions of the primary particles in both the CMS and Helicity reference frame and their analyzing power distributions are discussed. In addition, the Dalitz plot for $pK^+\Lambda$ events is presented and a signal from the $N\Sigma$ cusp effect is discussed.

Finally, a summary of this work and outlook are presented.

Chapter 1

The PANDA Experiment

1.1 The FAIR Accelerator Complex

The Facility for Antiproton and Ion Research (FAIR) is a new accelerator complex which is under construction adjacent to the GSI Helmholtz-Center in Darmstadt, Germany. It will be used for research with beams of heavy ions and antiprotons. The floor plan of the FAIR facility is shown in Figure 1.1. The main FAIR machine is the SIS100 synchrotron with a circumference of 1100 meters. It is used to accelerate high intensity proton and heavy ion beams to rigidity up to $Z \cdot 30$ GeV. Heavy ions can be further accelerated at lower intensities up to 34 GeV/u in the SIS300 synchrotron, which is housed in the same tunnel as the SIS100. The high intensity heavy ion beam from the SIS100 is also used to produce secondary beams of radioactive nuclei, which are collected, stored and cooled for further scattering experiments in a storage-cooler ring.

In the full facility the antiprotons are produced by directing the 30 GeV/ c proton beam from SIS100 onto a copper production target. Antiprotons with momentum around 3.6 GeV/ c are collected in the Collector Ring (CR). By applying strong stochastic cooling to the beam, the momentum spread of the antiprotons in the CR is reduced from $\Delta p/p \sim 3\%$ to $\sim 0.1\%$. Then, the beam is transferred to the Recuperated Experimental Storage Ring (RESR). This is repeated every 5 seconds, until the 10^{10} - 10^{11} accumulated antiprotons are injected in the High Energy Storage Ring (HESR). The HESR allows accelerating/decelerating and storing antiprotons in the momentum range from 1.5 to 15 GeV/ c . Using stochastic and electron cooling systems a high quality antiproton beam is produced by reducing the energy and emittance spread. HESR can work in two operation modes: a High Resolution (HR) mode with the beam momentum spread smaller than $\Delta p/p = 4 \cdot 10^{-5}$ for the 10^{10} stored antiprotons, and in a High Luminosity (HL) mode with a

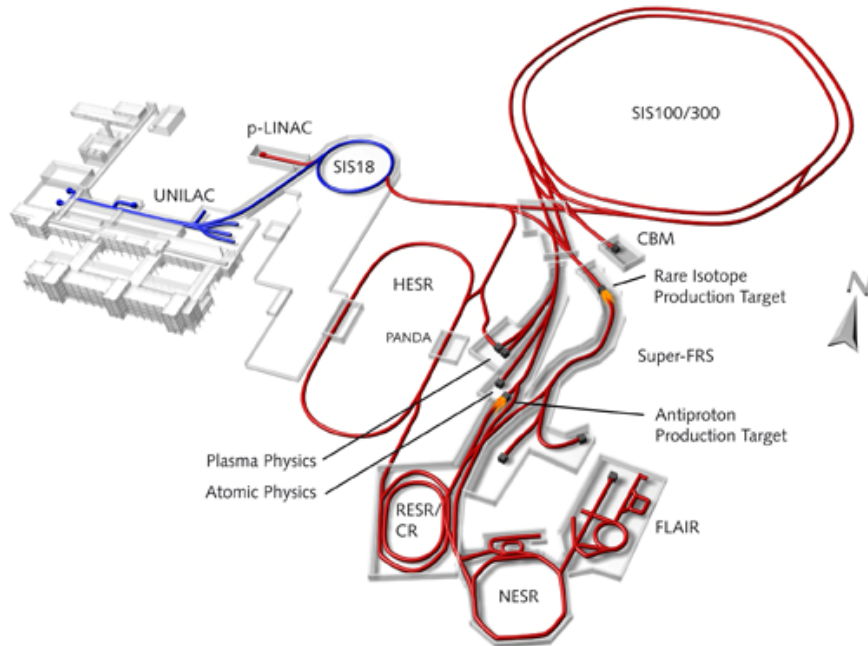


Figure 1.1: Schematic plan of the FAIR facility. The existing accelerators UNILAC and SIS18 belonging to the GSI-Darmstadt center are indicated with blue line. They are used as pre-accelerators. The new FAIR machines including the p-LINAC, SIS100 and SIS300 synchrotrons, NESR and RESR/CR cooler rings as well as the HESR synchrotron, at which the PANDA will be installed, are shown in red [4].

momentum spread of 10^{-4} but with 10^{11} antiprotons. The HR mode is used for the search of narrow states in formation reactions. The HL mode is foreseen for production reactions with small cross sections [4, 5, 6].

The FAIR facility allows several physics programs to be operated in parallel. These programs are divided into four major fields for Atomic, Plasma Physics and Applications (APPA), Nuclear Matter Physics (CBM), Nuclear Structure, Astrophysics and Reactions (NUSTAR) and physics with High Energy Antiprotons. The PANDA (antiProton Annihilation at Darmstadt) is an experiment in the field of physics with high energy antiprotons [4].

1.2 The PANDA Physics Program

The PANDA detector is an internal target experiment devoted to studies in the field of hadron physics by measuring reactions induced by scattering antiproton beams off a hydrogen target as well as off nuclear targets. The

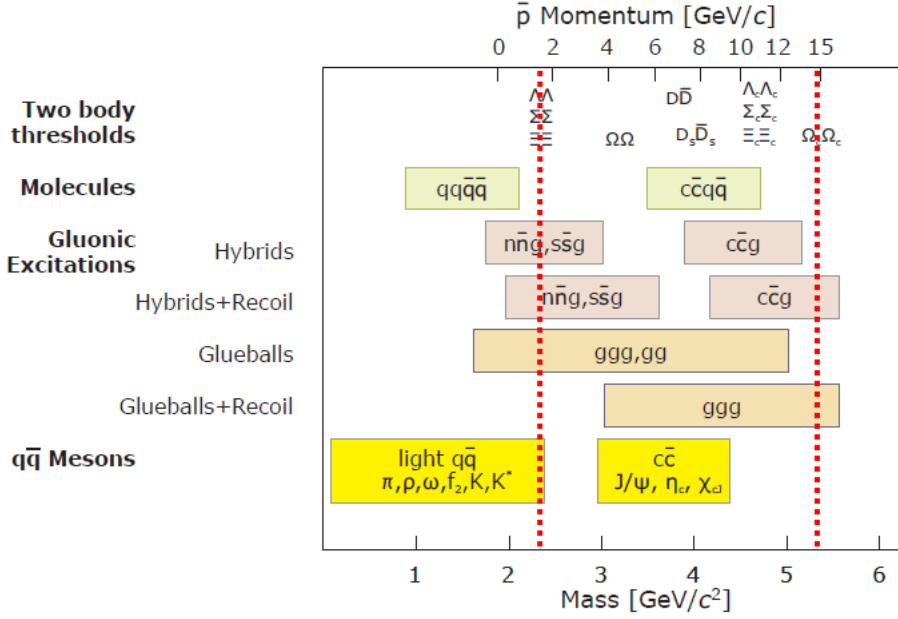


Figure 1.2: Overview of the accessible mass range (lower scale) for hadrons produced in $\bar{p}p$ collisions as a function of beam momentum (upper scale). The dashed red lines indicate the accessible momentum of antiproton beams at HESR and the corresponding mass range of the produced hadrons [7].

antiproton beam with a momentum in the range from 1.5 GeV/c to 15 GeV/c is provided by the HESR. The maximum momentum of the HESR antiproton beam corresponds to an energy in the center of mass system of 5.5 GeV and is sufficient to produce pairs of charm quarks. Therefore, one of the basic research areas of PANDA is the spectroscopy of charmonium states and of open charm mesons. Figure 1.2 shows the mass range of various states which can be investigated at PANDA.

Besides studies of conventional mesons consisting of quark-antiquark ($q\bar{q}$) pairs, PANDA will also be used for a search for exotic mesons such as glueballs (gg, ggg), hybrids ($q\bar{q}g$) and molecules or tetraquarks ($qq\bar{q}\bar{q}$). It is expected that the $\bar{p}p$ annihilation is well suited for observation of such exotic states due to the copious production of gluons. In experiments with hydrogen targets other topics such as the spectroscopy of charmed baryons and study of nucleon structure by measurements of time-like form factors is conducted. In measurements with nuclear targets, e.g. carbon or argon targets, studies of properties of mesons embedded in nuclear medium and investigations of single and double hypernuclei properties will be conducted [5, 7].

1.3 PANDA Detector

In order to pursue the planned physics program the PANDA detector has to fulfill the following basic requirements:

- high rate capability necessary for measurements at the maximum interaction rate of the antiprotons with the target $\sim 2 \cdot 10^7$ per second,
- close to 4π solid angle coverage,
- identification of charged particles including pions, kaons and protons as well as electrons and muons with a wide momentum range,
- a good momentum resolution for charged particles of about 1.5% at 1 GeV/c,
- detection of charmed meson vertices with precision of better than 100 μm ,
- electromagnetic calorimetry across a wide energy range.

PANDA is a fixed target experiment and therefore the reaction products are boosted in the forward direction. In order to provide an almost full solid angle coverage and good momentum resolution also at the most forward angles, the detector consists of two magnetic spectrometers: the Target Spectrometer (TS) which covers almost the full solid angle around the interaction point and the Forward Spectrometer (FS) which covers the very forward angles. A schematic view of the PANDA detection setup is shown in Figure 1.3.

The TS is based on a superconducting solenoid magnet with 2 T field strength with an inner radius of 1.05 m and 2.8 m length. The TS detection system is arranged in a barrel with two end-caps. The barrel covers polar angles between 22° and 140° . The region between 145° and 170° is covered by the backward end-cap detectors. The forward end-cap detectors extend the angular coverage down to $\pm 5^\circ$ and $\pm 10^\circ$ in the vertical and horizontal planes, respectively [5, 6].

The FS is located at 3 to 11 m downstream of the target and is based on a large dipole magnet. The FS covers polar angles below $\pm 5^\circ$ and $\pm 10^\circ$ in the vertical and horizontal planes, respectively [5].

The complete detection of the final state particles is possible using these two spectrometers, since both of the TS and FS are equipped with different detectors for tracking, charged particle identification, electromagnetic calorimetry and muon detection.

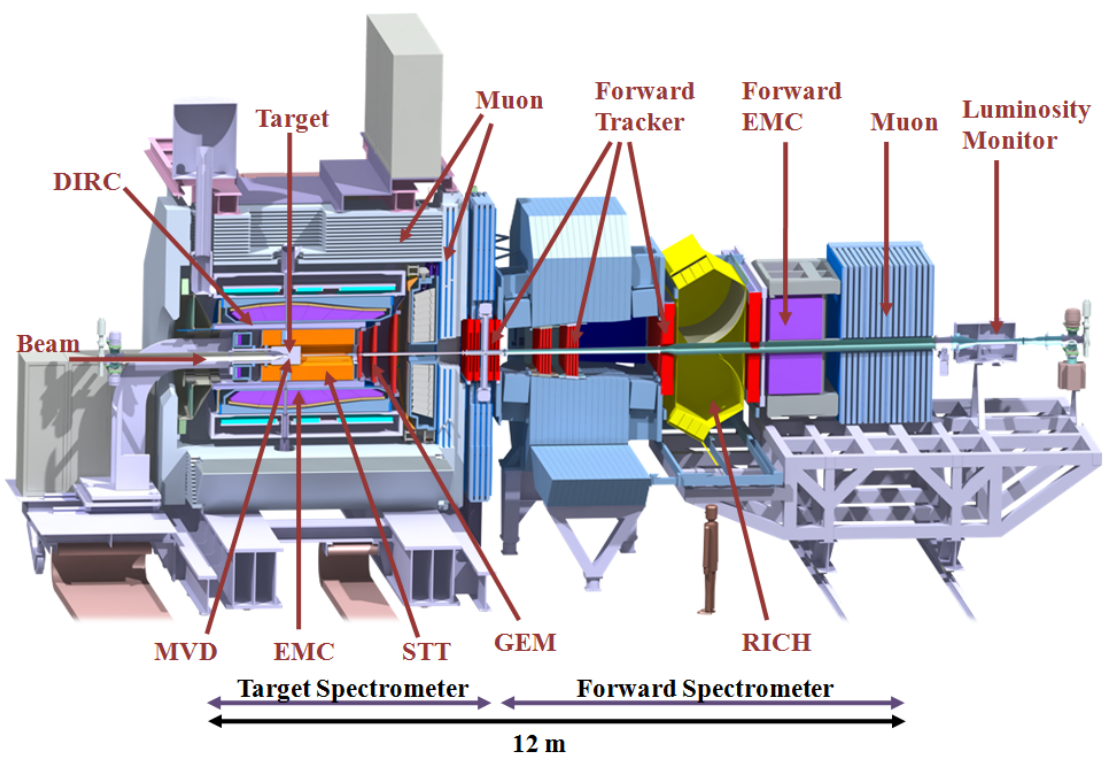


Figure 1.3: Schematic drawing of the PANDA detector [8].

1.3.1 Target Systems

The PANDA experiment uses two different internal target systems, a cluster-jet target and a pellet target [9]. In both cases the target material is injected inside a pipe which crosses the beam pipe at the interaction point.

The cluster jet target is produced by injection of pressurized cooled gas into the accelerator vacuum through a special nozzle. The injected gas immediately condenses, forming a narrow supersonic jet of nano-particles called clusters. The average number of molecules per cluster for hydrogen varies from 10^3 to 10^6 . The cluster-jet target provides a homogeneous target density of about $8 \cdot 10^{14}$ atoms/cm² with very little time dependence.

The pellet target provides a stream of frozen droplets, called pellets. The pellets with $10 - 30 \mu\text{m}$ diameter are emitted from a nozzle into the vacuum at a rate of 10^3 pellets/s. The pellet target provides high average target densities in the order of 10^{15} atoms/cm². However, the typical distance between consecutive pellets is on the order of a few millimeters, which is comparable with the diameter of the antiproton beam. Therefore, significant fluctuations of the instantaneous interaction rate in the experiment are expected.

Nuclear targets are provided by using deuterium or heavier gases like nitrogen and argon with both cluster and pellet target systems [6, 10].

1.3.2 Tracking Systems

The tracking systems in the Target Spectrometer consist of several subsystems including the silicon Micro Vertex Detector (MVD) and the cylindrical Straw Tube Tracker (STT). In the forward direction, the STT is supplemented with three planar stations of Gas Electron Multiplier (GEM) detectors. In the Forward Spectrometer, deflection of charged particles tracks in the magnetic field of the dipole magnet is measured with three pairs of planar tracking stations based on straw tubes.

The silicon Micro Vertex Detector (MVD) surrounds the interaction point and is used to improve the overall momentum resolution and to detect secondary decay vertices of charmed and strange hadrons decaying close to the interaction region. The MVD is designed based on silicon pixel detectors and silicon strip detectors with fast individual readout circuits. The MVD sensors are arranged in four cylindrical layers and six forward disks. The two inner layers in the cylindrical part contain pixel detectors and the two outer layers are made of double-sided silicon strip detectors. The position resolution of the MVD for primary and secondary vertices is better than $100 \mu\text{m}$ [10, 11].

The central STT which is used for the momentum analysis of charged particles in the field of the TS solenoid magnet consists of 4,636 self-supporting

straw tubes having a diameter of 1 cm and a length of 150 cm. The straws are arranged in a hexagonal shape of 24 layers around the MVD. The STT covers a polar angle range from about 10° to 140° . The full azimuthal angle coverage is only limited by the gap for the target pipe at $\pm 90^\circ$. A 3D schematic view of the STT is shown in Figure 1.4. A further description of the PANDA STT is given in Section 1.4.

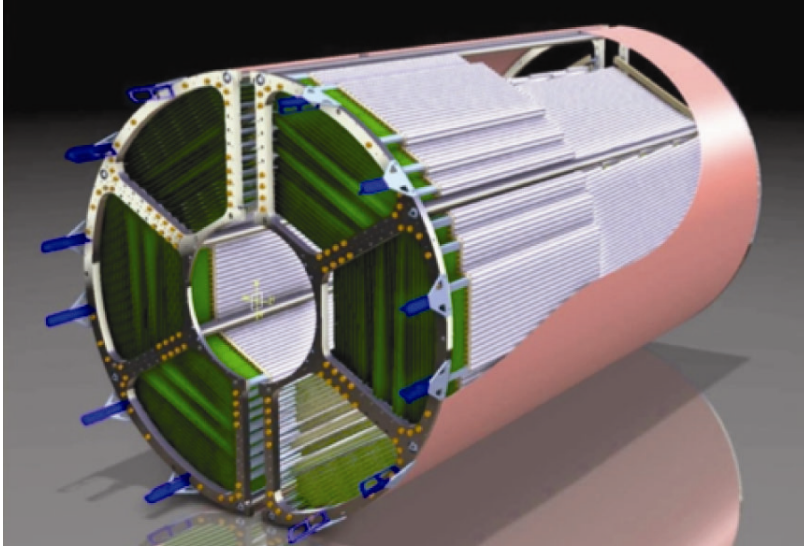


Figure 1.4: A schematic view of the central Straw Tube Tracker [10].

In addition to the STT there are three planar stations of Gas Electron Multiplier (GEM) placed at 1.1 m, 1.4 m and 1.9 m downstream of the target to track charged particles emitted at polar angles below 22° which cannot be measured by the STT alone. Each of the stations contains a double-sided readout plane in the center to measure the track position. On both sides of it there are three GEM foils used for electron multiplication. The stations have to tolerate a high counting rate of particles which are peaked at the most forward angles due to the relativistic boost of the reaction products [10]. Figure 1.5 shows the layout of the tracking system in the Target Spectrometer.

The Forward Tracker is foreseen for momentum analysis of charged particles in the Forward Spectrometer on the basis of deflection of their trajectories in the magnetic field of the dipole magnet. The field lines inside the dipole magnet gap are oriented vertically. The integral bending power of the dipole is scaled according to the beam momentum and at the maximum momentum of $15 \text{ GeV}/c$ it equals to 2 Tm . The measurement of the particle trajectories deflection in the dipole magnet field is performed with two pairs of planar tracking stations, one pair before and one behind the

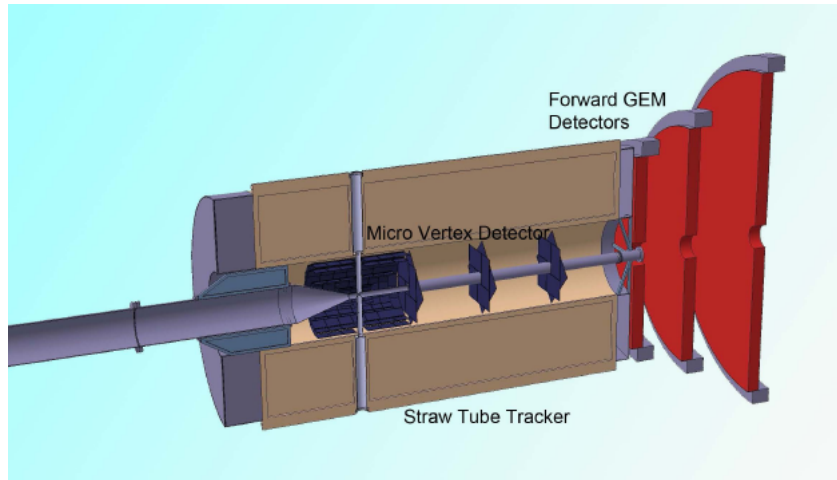


Figure 1.5: The tracking system of the Target Spectrometer including MVD, STT and forward GEM stations [10].

magnet. Additionally, a third pair of tracking stations is placed inside the gap to track low momentum particles, which hit the inner walls of the dipole gap. The tracking stations in the FT are based on the same type of straw tube detectors as the ones in the central STT [6, 8, 10]. In total there are 6 independent tracking stations in the Forward Tracker shown in Figure 1.6. Further details of the FT design are given in Section 1.4.

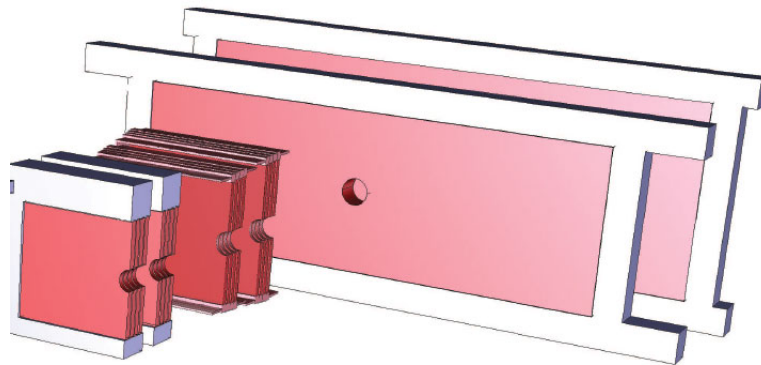


Figure 1.6: Schematic view of the Forward Tracker comprising three pairs of tracking stations. The hole at the center of each station is foreseen for the beam pipe [8].

1.3.3 Particle Identification Systems

Identification of charged pions, kaons and protons at high momenta is performed at PANDA with Cherenkov detectors, and at lower momenta with Time Of Flight (TOF) detectors as well as using the dE/dx information provided by the tracking detectors. There are also muon detectors for muon identification in both the TS and FS.

In the TS, two Cherenkov detectors of the DIRC (Detection of Internally Reflected Cherenkov) type are used: the barrel DIRC covering polar angles between 22° and 140° and the disc DIRC with acceptance corresponding to angles below 22° . The barrel DIRC consists of 96 radiator slabs manufactured of artificial quartz called fused silica with an index of refraction $n = 1.47$. The slabs are 1.7 cm thick and are arranged around a cylindrical surface with a radius of 48 cm. A charged particle passing through the slab with velocity $\beta > 1/n$ emits Cherenkov photons at the Cherenkov angle $\theta_c = \arccos(1/\beta n)$. The photons propagate along the slab via internal reflection and the light is focused by lenses onto Micro-Channel Plate Photo Multiplier Tubes (MCP PMTs). The pattern of photons registered in the array of PMTs allows to reconstruct the Cherenkov angle and thereby to calculate the particle velocity. This information combined with the result of the momentum reconstruction from the tracking system allows to determine the mass of the particle and thus to identify the particle type. In the disc DIRC the radiator is also made of fused silica and has a diameter of 2 m and a thickness of 2 cm. The Cherenkov light propagates via internal reflection to photo multiplier tubes which are placed on the circumference of the disc [8, 10].

In the FS, a Cherenkov detector of the RICH (Ring Imaging Cherenkov) type is foreseen. Application of two radiators - silica aerogel and C_4F_{10} - with two different indexes of refraction $n = 1.03$ and 1.0037 , respectively, provides pion, kaon and proton separation in a broad momentum range from 2 to 15 GeV/c. A lightweight mirror focuses the Cherenkov light onto an array of PMTs placed outside the active area [6, 10].

PANDA contains two Time Of Flight (TOF) systems, a barrel hodoscope in the TS and the forward wall in the FT. The barrel hodoscope is made of small plastic scintillator tiles which are read out by silicon photomultipliers. It has a form of a cylinder and it is located in front of the barrel DIRC. The PID performance of this detector is very limited due to its relatively small radius of 45 cm which corresponds to a time of flight of only 1.5 ns for highly relativistic particles. Therefore, an independent method based on the energy loss measurements in the STT is foreseen for the PID at low momenta in the Target Spectrometer.

The forward TOF wall consists of vertical plastic scintillator bars read

out at both ends by photomultipliers. The wall is located 7 m downstream of the target and the TOF measurement with an expected resolution of about 100 ps provides PID for momenta below 2 GeV/ c which are not covered by the Forward RICH [10].

For identification of muons the yoke of the solenoid magnet consists of layers of iron interleaved with Mini Drift Tubes (MDTs). Also in the FS a muon range system consisting of iron plates and layers of MDTs is placed at a distance of about 9 m from the target. The system provides the discrimination of pions from muons, detection of pion decays and the energy determination of neutrons scattered in the forward direction [10].

1.3.4 Electromagnetic Calorimeter

The Electromagnetic Calorimeter (EMC) based on lead tungsten (PbWO₄) crystals is used for photon and electron detection in the TS. Due to the fast response of this scintillator (less than 20 ns) and its high radiation hardness, the EMC is well suited for the high rate environment of the PANDA experiment. The crystals have a length of 20 cm corresponding to 22 X_0 . The front face of the crystals is $2 \times 2 \text{ cm}^2$. By cooling the crystals to -25°C the light yield is increased by a factor four compared to the yield at room temperature. The EMC in the target spectrometer consists of three different parts: the barrel, the backward end-cap and the forward end-cap. Figure 1.7 shows a view of the EMC used in the PANDA detector. There are 15,552 PbWO₄ crystals which are read out by avalanche photodiodes. The e/π^- separation can be done by the EMC for momenta above 0.5 GeV/ c [8, 10].

In the FS, a Shashlyk-type calorimeter is used. It is placed 7.5 m downstream of the target. It consists of 374 super modules arranged in 27 rows and 13 columns. Each super module consists of four modules with transverse size of $55 \times 55 \text{ mm}^2$. The module contains 380 layers of 0.3 mm thick lead absorber interleaved with 1.5 mm plastic scintillator plates. Scintillation photons produced in the modules are collected on a photomultiplier by means of 36 wave length shifter fibers penetrating the layers through 1 mm openings [8, 10].

1.4 PANDA Straw Tube Tracker (STT)

1.4.1 Self-Supporting Straw Tube Detectors

The STT and the Forward Tracker at PANDA have to fulfill similar requirements:

- low mass $X/X_0 \sim 1\%$,

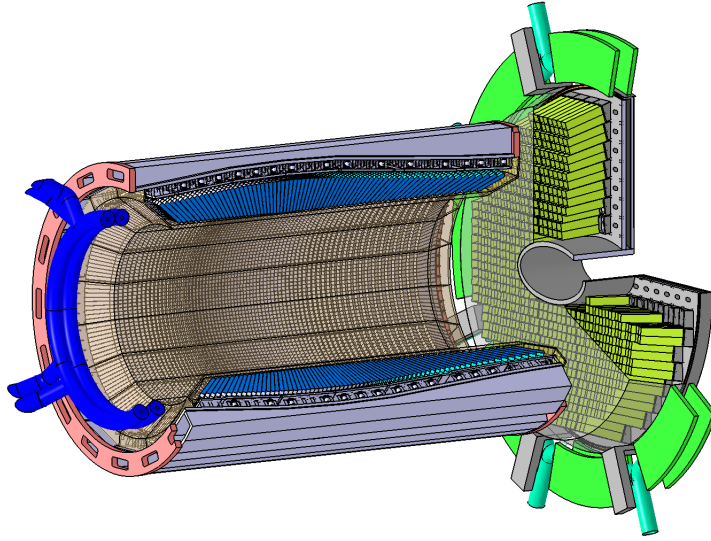


Figure 1.7: A view of the barrel and the forward end-cap of the EMC in the Target Spectrometer. The barrel has an inner diameter of 57 cm. The solid angle coverage of the EMC is 96% of 4π [8].

- high momentum resolution $\Delta p/p \sim 1.5\%$,
- high rate capability up to 10^4 tracks/cm²s⁻¹,
- radiation hardness 0.1 – 1 C/cm per year.

These requirements are well fulfilled by self-supporting straw tubes developed for the COSY-TOF experiment [12], and they are chosen for the PANDA trackers. In the self-supporting straw detectors, the mechanical tension of the anode wire and of the straw tubes is maintained by gas overpressure and not by support frames which are typically used for this purpose. It allows to construct very light tracking detectors since massive support frames are not needed. Besides, the chosen straw tubes have a very low material budget, since very thin Mylar foil is used as the straw tube material. The straw tubes have a diameter of 10 mm and total wall thickness of $27\ \mu\text{m}$. They consist of two $12\ \mu\text{m}$ thick layers of aluminized Mylar film twisted around a rotating mandrel and glued together where they overlap. The tubes are aluminized at the inner surface, which is used as the cathode, and also on the outer surface in order to prevent light from entering the detector. Mylar is an appropriate material because of its low density and suitable mechanical properties that prevent large changes of the tube length at high gas pressure. A gold-plated tungsten wire with $20\ \mu\text{m}$ diameter is used as the anode.

The straw tubes are closed at both ends with end-plugs that are made of ABS plastic. The end-plugs have a wall thickness of 0.5 mm and they are glued to the Mylar film leaving a 1.5 mm film overlap on both ends. The overlap is used for placing a gold-plated copper-beryllium spring wire which is used to provide the electric cathode contact. The end plugs have a central hole with a 3 mm thick cylindrical nose to insert a copper pin that is crimped around the anode wire. The wire is stretched along the straw tube axis by a weight of 50 g at 1 bar gas overpressure in the straw tube and crimped in the copper pins. The anode wire is kept at positive high voltage and the cathode is at ground potential. A micro PVC tube is fed through another hole and glued in the end-plugs to enable a gas flow through the tube. As the working gas a mixture of Ar + CO₂ with the volume ratio (90 : 10) is chosen to provide good spatial resolution, high rate capability and low aging. A fully assembled straw tube detector has a weight of 2.5 g. An average thickness of the straw tube in its sensitive area corresponds to $X/X_0 = 0.044\%$ ($= 0.03\%$ Mylar + 0.013% gas + 0.00086% wire) [10, 12, 13]. Figure 1.8 shows the construction of a straw tube with different elements used in its structure.

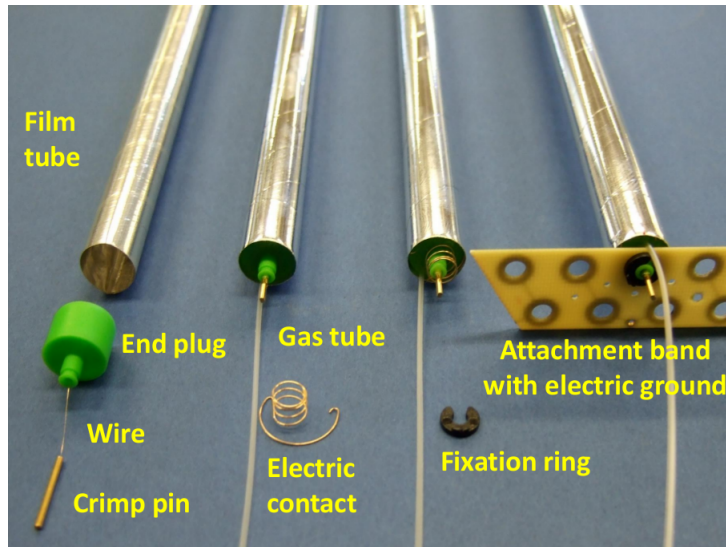


Figure 1.8: Different components used in the straw tube detector and four assembly steps (from left to right) of the straw tube [10].

Single straw tubes are glued together in multilayer modules (see Figure 1.9). Such modules show a very high rigidity when the gas overpressure is applied in the straws. The modules contain a different number of straws depending on the location in the STT. In the Forward Tracker all modules consist of 2×16 straws.



Figure 1.9: (Left) gluing of straw tubes in a double layer on a reference table, (Right) a straw tube double layer. Two layers of straws in a double layer are shifted with respect to each other by half of the distance between the straws in order to resolve the “left-right” ambiguity of the track position with respect to the anode wires [10].

1.4.2 Central Straw Tube Tracker

The central STT in PANDA has a cylindrical structure with an inner radius of 150 mm, outer radius of 420 mm which is placed from -550 mm to $+1100$ mm in z -direction relative to the target. The total cylindrical volume is cut into two semi-cylinders with a gap of 42 mm for the vertical target pipe. The front-end electronics cards and other services of the STT are placed at the backward end of the detector. Each of the two semi-cylindrical volumes of the STT is filled by three sectors of straw tubes aligned in the beam direction (z -axis) and arranged in planar multi layer modules as shown in Figure 1.10. The hexagonal layout of both volumes together makes an almost cylindrical shape for the STT.

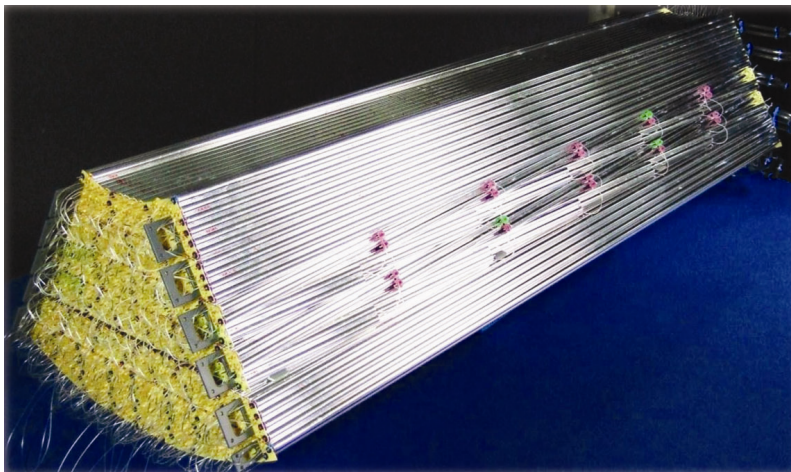


Figure 1.10: Photograph of one hexagonal sector [10].

In each sector the innermost 8 straw layers are parallel to the beam axis. These layers are followed by a block of 4 straw double layers which are skewed by $\pm 2.9^\circ$ relative to the axially aligned straw layers. Then, there are again 4 straw layers parallel to the beam axis and another 7 layers aligned parallel to the beam with a decreasing number of straws per layer to achieve the outer cylindrical shape of the STT. A schematic plan of the central STT projection on the x-y-plane perpendicular to the beam axis is shown in Figure 1.11.

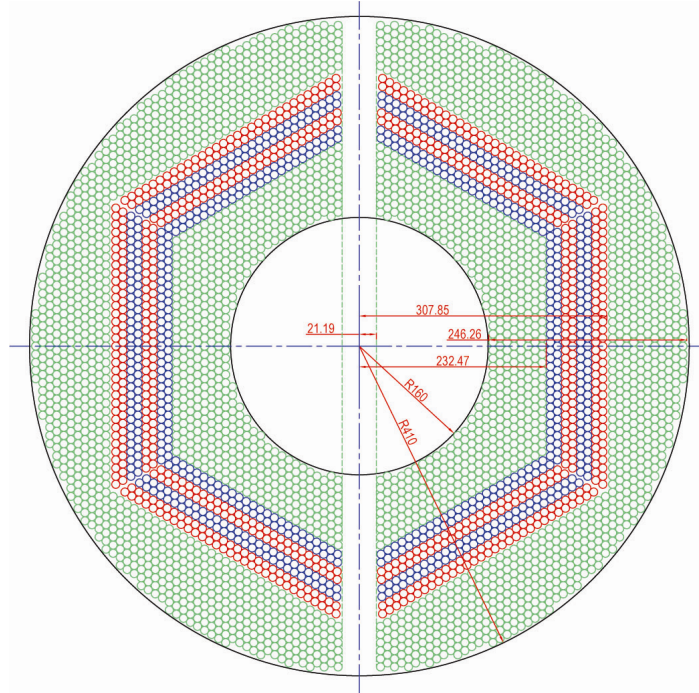


Figure 1.11: x-y-view of the straw tubes layout in the STT. The green marked straws are parallel to the beam axis. The blue and red marked ones are skewed by $+2.9^\circ$ and -2.9° relative to the axially aligned straws, respectively [10].

Because the solenoid magnetic field is parallel to the beam axis, charged particles follow helix trajectories, corresponding to a circle in the x-y projection and a line relative to the z-direction. In order to do a spatial reconstruction of the charged particle tracks, the straws aligned parallel to the magnetic field are used to measure the helix circle and the skewed straws are used to measure the helix slope.

There are in total 4,636 straws in the STT, each with a diameter of 10 mm and a length of 1500 mm, except some of the skewed tubes in each hexagon sector which have shorter lengths. By using self-supporting straws in each module, no extra support is needed for the STT [10].

1.4.3 Forward Tracker

The Forward Tracker performs momentum analysis of charged particles in the Forward Spectrometer by measuring the deflection of their trajectories in the dipole magnetic field. The FT consists of three pairs of planar tracking stations: one pair is placed before the dipole magnet, the second pair inside the magnet gap and the third pair after the magnet. The FT uses the same straw tubes as the ones chosen for the central STT. Each tracking station contains four double layers of straw tubes. The first and the fourth double layer contains vertical straws and the two intermediate double layers are tilted by $\pm 5^\circ$ to achieve sufficient position resolution in the vertical direction. Each double layer consists of straw tube modules. Each module contains 32 straws arranged in a double layer. It has its own high voltage supply, gas supply and front-end electronics card. The modules forming one double layer of straws are mounted side by side on a support frame. One support frame is used for two double layers (see Figure 1.12 top). A module can be easily mounted and dismantled from the support frame without affecting on neighboring modules as shown in Figure 1.12 (bottom).

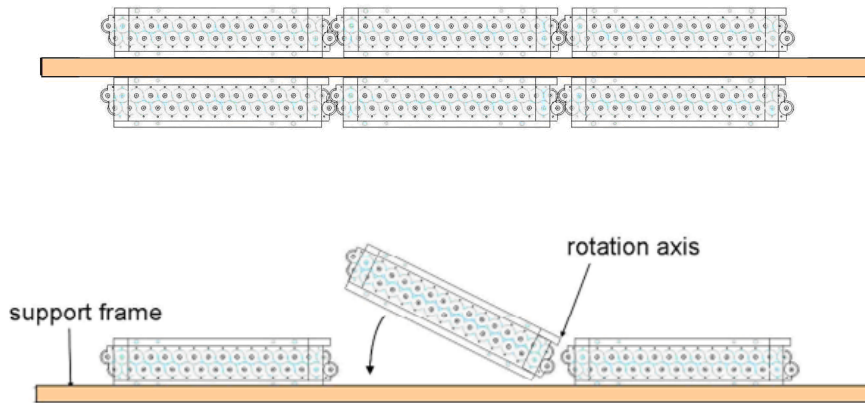


Figure 1.12: (Top) schematic view of two double layers of straw tubes mounted on a common support frame. For simplicity only three modules in each layer are shown. (Bottom) method of placing a single straw module on the support frame. In order to avoid clashes with neighboring modules, the module is rotated around the axis defined by one of the edges of its housing [8].

Each tracking station is supported by a rectangular chassis for installation in the detector. The two tracking stations before the dipole magnet have an active area of 134 cm horizontally and 64 cm vertically and are the smallest ones in the FT. A view of these two tracking stations equipped with front end electronics cards and mounted on a common platform is shown in

Figure 1.13. The tracking stations placed after the dipole magnet have an active area of $392 \times 120 \text{ cm}^2$ and are the largest ones in the FT. There are 12,224 straw tubes in the full Forward Tracker [8].

The expected position resolution of this system is about 0.1 mm per detection layer and the material budget in each tracking station is 0.3% of a radiation length X_0 . A momentum resolution better than 1% is expected to be achieved with the Forward Tracker [8].

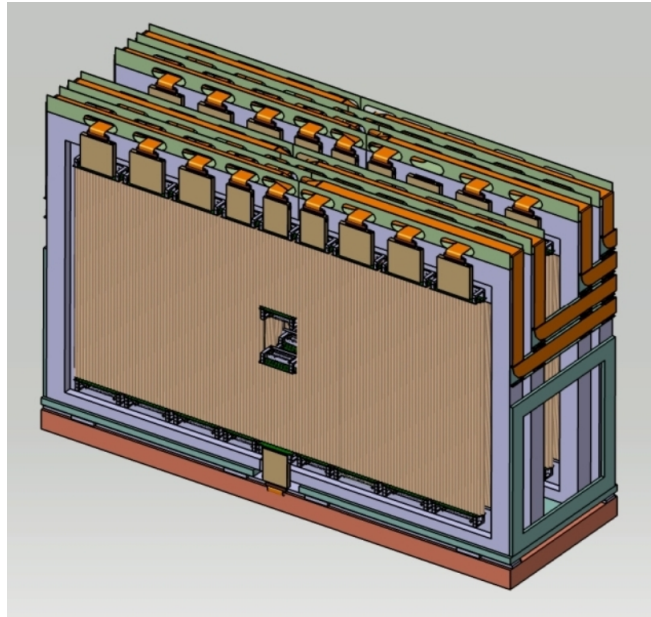


Figure 1.13: A schematic view of two tracking stations located before the dipole magnet. The stations are placed on a common platform. An opening in the central region of the stations is foreseen for the beam pipe [8].

1.4.4 Readout Electronics

The readout electronics for the PANDA straw tube trackers should allow to measure the drift time as well as the ionization density in the straw tubes, which is needed for identification of low momentum particles. The electronics should work properly at the expected high counting rates, reaching 1 MHz/channel for straw detectors located close to the beam pipe. The drift time has to be measured with moderate resolution of 1 ns. This accuracy is sufficient for precise tracking since the expected drift velocity is roughly $30 \mu\text{m}/\text{ns}$, corresponding to an uncertainty of the track distance to the anode wire of $30 \mu\text{m}$ which is substantially smaller than the expected position resolution of about $100 \mu\text{m}$ for the straw tubes. The straw tube readout consists

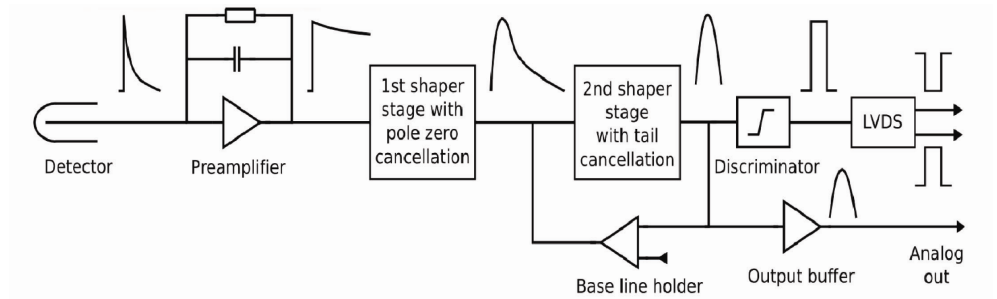


Figure 1.14: Block diagram of the developed front-end readout electronics for the PANDA straw tube trackers [10].

of analog front-end electronics and of digitizing electronics. A prototype front-end circuit is developed at the AGH University [10].

At present two alternative concepts of the digitizing electronics are studied. One concept is based on the application of the Time Over Threshold (TOT) measurement of the straw tube pulses to determine their amplitudes. For this measurements, time to digit converters of the TRB.v3 type [14] are proposed. The second concept is based on fast sampling ADCs which are developed in the Jülich Research Center for the measurement of the amplitudes of the straw tube pulses [15].

A new ASIC (An Application Specific Integrated Circuit) [16] is being developed in order to read out the straw tube signals in the PANDA experiment. The first prototype ASIC containing four channels is designed at the AGH University [10, 13, 17] and fabricated in the AMS $0.35\ \mu\text{m}$ technology. Each channel includes a charge preamplifier with variable gain, a CR-RC² shaper with variable peaking time, a tail cancellation network with changeable parameters and a baseline stabilizer. Furthermore, a leading edge discriminator circuit with a fast differential LVDS (Low-Voltage Differential Signaling) [18] output and an analog output provide both timing and amplitude information, respectively. Figure 1.14 shows the schematic plan of the designed front-end readout electronics developed for the PANDA straw tube trackers. Since several parameters of the front-end chip are programmable, the optimum configuration of these parameters is determined using the straw tube signals from ⁵⁵Fe X-ray and ⁹⁰Sr radioactive sources. Moreover, a high rate test has been performed at the COSY accelerator with a $2.7\ \text{GeV}/c$ proton beam at a rate of $1.2\ \text{MHz}$ per single straw tube in order to check the optimum setup of the circuit. The produced straw signals are recorded by a fast sampling ADC in a long time window of $5\ \mu\text{s}$ [10]. The test result in Figure 1.15 shows that the baseline remains stable and the resolution of the straws is not affected at high counting rates.

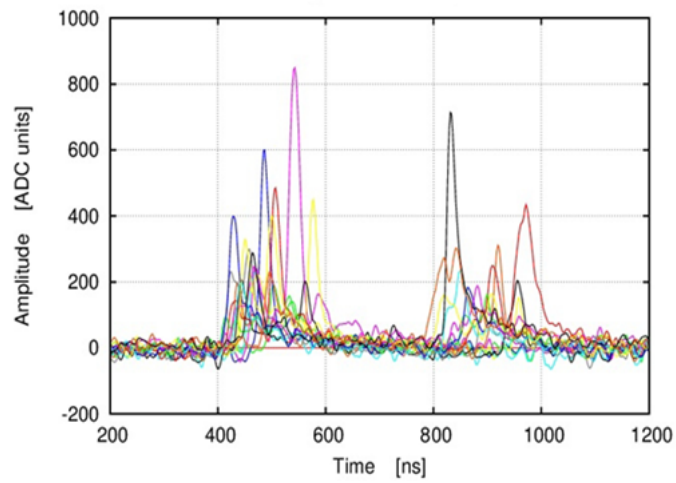


Figure 1.15: The straw signals of a proton beam at $2.7 \text{ GeV}/c$ at a rate higher than 1 MHz per single straw recorded by the designed readout electronics for the PANDA straw tube trackers [10].

Chapter 2

Physics of Straw Tube Detectors

Straw tubes are proportional gaseous drift detectors. They consist of a gas filled conducting tube and a wire stretched along the tube axis. When charged particles pass through the straw tube, they interact electromagnetically with the gas atoms and molecules. These Coulomb interactions result in the creation of electron-ion pairs. Applying an electric field between the wire and the tube causes the electrons and ions to drift through the gas. The wire is usually biased to a positive voltage of a few kV and collects the electrons while the ions drift toward the tube wall as the cathode. The electric field strength near the anode wire is strong enough so that primary electrons obtain enough energy between collisions to produce secondary ionization electron-ion pairs in the gas. The produced electrons continue to drift and ionize more gas molecules and hence form an avalanche. When this avalanche reaches the anode wire it is large enough to produce a measurable signal to be recorded by the readout electronics. Because the straw tubes operate in the proportional region, the size of the signal is proportional to the originally deposited charge.

Charged particles that traverse the straw tubes are tracked by measuring the drift time information of the ionization electrons to the anode wire. The drift time measurement is usually done together with additional timing detector such as scintillation detector. Therefore, the measured arrival time of electrons at the anode wire relative to the time t_0 from a scintillator determines the drift time of the electrons in the straw tubes. Using this drift time information, the distance of closest approach of the charged particle track to the anode wire is determined. This distance is the main information for charged particles tracking using straw tube detectors [10, 19, 20]. A sketch of the straw tube operation for tracking is shown in Figure 2.1. Further discus-

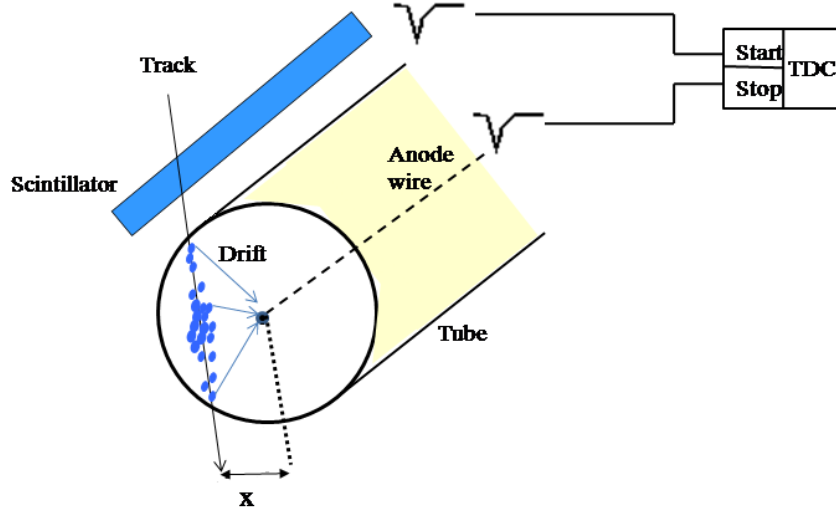


Figure 2.1: Schematic drawing of a straw tube operation for charged particle tracking. Distance of closest approach of particle track to anode wire is indicated as x .

sion about different processes involved in the operation of gaseous detectors are presented in the next sections of this chapter.

2.1 Ionization Process in Gases

Charged particle passing through the gas, loses energy due to ionization and excitation of gas molecules along its path. The average specific energy loss per unit path length (dE/dx) is given by the *Bethe-Bloch* formula (see e.g. Ref. [21]). In argon at standard temperature and pressure (STP), minimum ionizing particles lose 2.44 keV/cm of track length and in CO_2 the specific energy loss is 3.01 keV/cm [20]. In the $\text{Ar} + \text{CO}_2$ mixture with the volume ratio $f_{\text{Ar}} : f_{\text{CO}_2} = 90 : 10$, the energy loss can be determined by calculating the weighted average of the energy losses in pure gases:

$$\begin{aligned} \frac{dE}{dx} &= f_{\text{Ar}} \left(\frac{dE}{dx} \right)_{\text{Ar}} + f_{\text{CO}_2} \left(\frac{dE}{dx} \right)_{\text{CO}_2} = 0.9 \cdot 2.44 \text{ keV/cm} + 0.1 \cdot 3.01 \text{ keV/cm} \\ &= 2.50 \text{ keV/cm} \end{aligned} \tag{2.1}$$

In the PANDA straw tube detectors, the specific energy loss is two times higher, because gas has a pressure of 2 bar. In this way, minimum ionizing particles passing through the straw tube close to the anode wire lose on average 5 keV.

The creation of electron-ion pairs due to the interaction of the incident particle with the gas atoms or molecules is called the primary ionization. The number of primary electron-ion pairs (n_p) depends on the atomic number, density and ionization potential of the gas, and on the energy and charge of the incident particle. If the ejected electron has an energy larger than the ionization potential of the medium, it can further ionize the medium producing secondary ion pairs. The sum of the primary and secondary ionization processes is called the total ionization. The total number of electron-ion pairs can be calculated as $n_t = \Delta E/W$, where ΔE is the total energy loss in the gas volume and W is the average effective energy necessary to produce an electron-ion pair in the gas medium [19, 20, 22]. Table 2.1 lists the values of dE/dx , W , n_p and n_t for argon and CO₂. The number of primary electrons in the Ar + CO₂ (90 : 10) mixture at STP is calculated to be:

$$n_p = f_{Ar}n_{pAr} + f_{CO_2}n_{pCO_2} = 0.9 \cdot 29.4 \text{ cm}^{-1} + 0.1 \cdot 34 \text{ cm}^{-1} \cong 30 \text{ cm}^{-1} \quad (2.2)$$

and the total number of ionization electrons is determined to be:

$$n_t = f_{Ar}n_{tAr} + f_{CO_2}n_{tCO_2} = 0.9 \cdot 94 \text{ cm}^{-1} + 0.1 \cdot 91 \text{ cm}^{-1} \cong 94 \text{ cm}^{-1}. \quad (2.3)$$

For the Ar + CO₂ (90 : 10) mixture at 2 bar pressure, as foreseen for the PANDA straw tube detectors, the number of primary (total) ionization electrons equals 60 (188) cm⁻¹. Therefore, it can be concluded that on average one primary ionization electron produces two electrons due to secondary ionization. Furthermore, the average distance between the primary ionizations is about 170 μm. This value sets a limit on the position resolution in the straw tubes for tracks passing in the vicinity of the anode wire.

Table 2.1: Energy loss per unit length, average energy to create one ionization electron, number of primary electrons and total number of ionization electrons per unit length for a minimum ionizing particle in argon and CO₂. All numbers are given for standard temperature and pressure [20].

Gas	dE/dx [keV/cm]	W [eV]	n_p [ion-pairs/cm]	n_t [ion-pairs/cm]
Ar	2.44	26	29.4	94
CO ₂	3.01	33	34	91

The energy loss and the numbers of total and primary ionization electrons calculated above are average values, and they can substantially vary from event to event due to statistical fluctuations. It is possible that a relatively large energy loss happens in a central collision of the passing particle with an electron in an atom or molecule of the gas. These central collisions lead to

the production of energetic δ -electrons and result in a strong asymmetry in the statistical distribution of the energy loss, with a tail extending towards high energies. The distributions of the energy loss and the total number of ionization electrons can be well described by the *Landau-Vavilov* function [20]. The number of primary ionizations follows the Poisson distribution, since they can be considered as statistically independent events.

2.2 Drift of Electrons and Ions in Gases

In the absence of an electric field, the free electrons in the gas move randomly and collide with the gas molecules with an average thermal energy of $(3/2)kT \approx 0.035 \text{ eV}$ at room temperature. When an electric field is applied, electrons gain extra velocity from the field in addition to their random thermal velocity. In elastic collisions with gas atoms or molecules, electron loses only a small fraction of its kinetic energy due to its smaller mass compared to the mass of atom. Therefore, in the presence of a strong electric field, the average kinetic energy of free electrons in gas is much higher than the thermal energy. The presence of electric field results also in the drift of electrons along the field lines. The drift is superimposed on the random movement. The mean drift velocity of electrons between the collisions is determined by the acceleration of electrons along the field (eE/m) and the mean time between the collisions (τ) and is given by [20]

$$v_d = \frac{eE\tau}{2m}, \quad (2.4)$$

where m is the electron mass, E is the electric field strength. Generally, τ is related to the collision cross section σ , the total velocity u and the number of molecules per unit volume N :

$$\tau = \frac{1}{N\sigma u}. \quad (2.5)$$

The total velocity u is related to the kinetic energy of the electrons in an electric field which is the sum of the energy received from the electric field and the thermal energy. The energy of electrons is much higher than the energy of thermal motion, and the drift velocity can be expressed as a function of the collision cross section σ and the average fractional energy loss per collision λ by [23]

$$v_d^2 = \frac{eE}{mN\sigma} \sqrt{\frac{\lambda}{2}}. \quad (2.6)$$

The drift velocity approaches zero when λ vanishes. The behavior of the collision cross-section σ and the fractional energy loss λ are shown in Figure 2.2 for argon and methane gas as a function of the total kinetic energy ε .

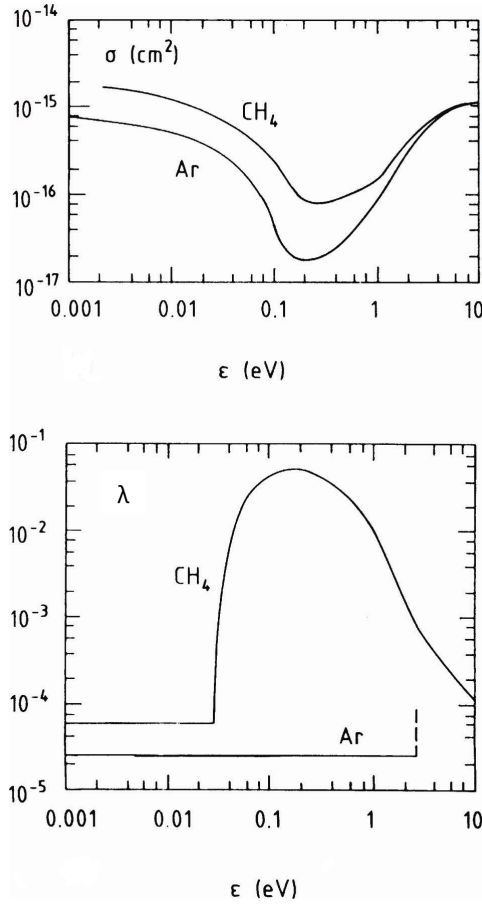


Figure 2.2: (Top) collision cross section $\sigma(\epsilon)$ as a function of the total kinetic energy ϵ for argon and methane. There is a minimum near $\epsilon \approx 0.25$ eV for argon and $\epsilon \approx 0.30$ eV for methane due to the quantum-mechanical process called the Ramsauer effect. (Bottom) fractional energy loss per collision $\lambda(\epsilon)$ as a function of the total kinetic energy ϵ for argon and methane [23].

As shown in Figure 2.2 (bottom), methane molecules are excited at 0.03 eV and in contrast argon atoms are excited above 11.5 eV. Due to a high excitation energy in argon, electrons scatter predominantly elastically from atoms. In such a case the fractional energy loss per collision λ is very small since it is proportional to the mass ratio of electrons and atoms which is about $2 \cdot 10^{-5}$. The small value of λ results in high energies of the random motion of electrons in the presence of electric field since the kinetic energy of electrons which is gained by acceleration in the electric field is dissipated very ineffectively in single collisions. Therefore, gases with small value of λ resulting in high energy of the random motion are called “hot”. In molecular gases such as methane or carbon dioxide the excitation energies of molecules

are very low and the fractional energy loss λ is high due to inelastic collisions of electrons with molecules. Gases with high values of λ in the order of $10^{-3} - 10^{-1}$ with resulting small energy of the random motion of electrons are called “cold”.

By adding a small fraction of molecular gases to a noble gas the fractional energy loss λ increases at low energies. This effect enhances the fraction of electrons with energy close to the Ramsauer minimum. Since the cross section σ at the Ramsauer minimum decreases (see Figure 2.2 top), the drift velocity of electrons grows significantly at low energies [23]. Results of calculations of the drift velocity for different fractions of CO₂ in argon gas are presented in Section 3.3.

Due to the high mass of the ions, they move much slower than electrons along the electric field direction. The ions lose a significant fraction of their energy gaining from the electric field in the collisions with gas molecules due to comparable masses of the collision partners. Therefore, the ions energy is mostly thermal. The drift velocity of ions W^+ is linearly proportional to the reduced field E/P , where P is the gas pressure. The proportionality coefficient of the ion drift velocity W^+ and the reduced electric field is called the mobility μ^+ ,

$$W^+ = \mu^+ \frac{E}{P}. \quad (2.7)$$

For typical electric field strengths in gaseous detectors the average energy of ions does not change up to very high fields. Therefore, the ion mobility does not vary much with the electric field strength [20, 23].

In gas mixtures, the charge-exchange process can influence the transport of charges carried by ions. The charge-exchange takes place for a drift ion when it collides with a molecule that has an ionization potential smaller than the ion itself. As a result, the drift ion is neutralized and creates a new ion. In the Ar + CO₂ mixture the charge-exchange process takes place from produced Ar⁺ ions to the CO₂ molecules, and hence the CO₂⁺ ions are created. Therefore, the CO₂⁺ ions are the main carriers of positive charges in Ar + CO₂ mixtures. In typical drift detectors, the electron mobility is on the order of $10^4 \text{ cm}^2\text{V}^{-1}\text{s}^{-1}$, whereas for the ions the mobility is about $1 \text{ cm}^2\text{V}^{-1}\text{s}^{-1}$ [23].

In gases, the drift path of the electrons diverges from the electric field direction due to multiple collisions with gas molecules. For originally point-like distribution of electrons the space distribution after time t along any direction is described by a Gaussian function. The standard deviation of the distribution for a drift path x is related to the drift velocity v_d as follows:

$$\sigma_x = \sqrt{\frac{2Dx}{v_d}}, \quad (2.8)$$

where D denotes the diffusion coefficient. The diffusion width of electrons is also related to their energy ε by [23]

$$\sigma_x^2 = \frac{4\varepsilon L}{3eE} \quad (2.9)$$

where L is the distance travelled by the electrons. From this formula it follows that for electrons moving with high energy ε in “hot” gases, the diffusion width is much larger compared to the case of “cold” gases with small values of ε .

Diffusion is usually presented in two directions: parallel to the electric field E called longitudinal diffusion ($D_L \parallel E$) and perpendicular to the electric field E called transverse diffusion ($D_T \perp E$), which is typically larger than D_L . In tracking detectors the diffusion decreases both the time and spatial resolution, therefore, it is desirable to reduce this effect. The diffusion of electrons can be reduced by adding “cold gases” to the operating gas mixture. Due to the high fractional energy loss per collision for electrons in “cold gases”, they decrease the electron kinetic energy between collisions and keep them in thermal equilibrium with the gas, hence reducing the electrons diffusion [20, 23].

The presence of a magnetic field affects electrons and ions drifting in an electric field by applying the Lorentz force to them. The effect of the magnetic field is proportional to the drift velocity of the electrons and ions. Since the drift velocity of the electrons is about 10^4 times higher than for the ions, the effect of the magnetic field on drifting ions is negligible compared to the electrons. When the magnetic field B is present, the electrons move along a direction which is different from the electric field lines due to the Lorentz force and their drift velocity is reduced. The drift path of the electrons is longer than in the absence of magnetic field, and therefore, the drift time of the electrons increases. In a constant electric and magnetic field, the deflection of the drift lines relative to the electric field lines is defined by the so called Lorentz angle α_H . The drift velocity of electrons and the Lorentz angle in the presence of a magnetic field B oriented in a direction perpendicular to the electric field is given by [20]

$$v_B = \frac{v_d}{\sqrt{1 + \omega^2 \tau^2}}, \quad \omega = \frac{eB}{m} \quad (2.10)$$

$$\tan \alpha_B = \omega \tau, \quad (2.11)$$

where v_B is the new drift velocity of the electrons which is different from the drift velocity v_d , ω is the Larmor frequency and τ is the mean time between collisions [20, 23].

2.3 Gas Amplification

In a straw tube the electron drifts to the anode wire in an increasing electric field E given by

$$E(r) = \frac{CV_0}{2\pi\epsilon_0} \frac{1}{r}, \quad (2.12)$$

where r is radial position in the tube, V_0 is the potential difference between the cathode and the anode wire, C is the capacitance per unit length of the straw tube and ϵ_0 is the dielectric constant. In the PANDA straw tubes the electric field increases from about 3 keV/cm at a distance $r = 1$ mm from the wire up to about 300 keV/cm at the wire surface ($r = 0.01$ mm). Then electrons pick up sufficient energy between the collisions with the gas atoms or molecules to initiate inelastic interactions such as excitation and ionization. If the energy of the electron exceeds the ionization potential of the gas, ionization occurs and another electron-ion pair is produced. The average distance an electron travels between the ionizing collisions is called the mean free path of the ionization. The inverse of the ionization mean free path is called the first Townsend coefficient, α , which represents the number of ion pairs produced per unit length of drift. The multiplication of the number of electrons in the avalanche region continues in the longitudinal direction until all the electrons are collected on the wire. The multiplication M for a path r is given by

$$M = \frac{n}{n_0} = \exp(\alpha r), \quad (2.13)$$

where n_0 is the original number of electrons produced by the traversed charged particle and n is the number of electrons after the path r . Generally, there is a non-uniform electric field in the straw tube and α is not a constant. Therefore, the multiplication M is modified as

$$M = \exp\left(\int_{r_0}^{r_1} \alpha(r) dr\right). \quad (2.14)$$

There is a limit for the multiplication factor because of space-charge effects which grow in the avalanche region and reduce the gas gain. In addition, operating with high gas gain reduces the effective operational life time of the detector in high radiation environments due to aging effects. Therefore, the gas amplification is usually in the range of $10^4 - 10^6$ [20, 23].

Since the drift velocity of the electrons is higher than that for the ions in gases and due to the electrons diffusion, a typical drop-like shape of the ionization distribution appears during the avalanche as shown in Figure 2.3. All electrons are located at the front of the drop-like charge distribution due to their higher drift velocity, whereas the positive ions are behind and

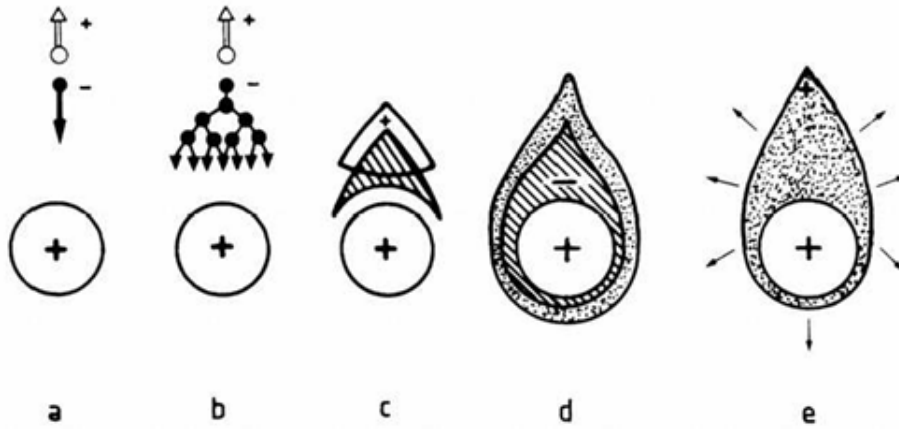


Figure 2.3: Time development of the ionization distribution in a gaseous detector. The avalanche region has a drop shape around the wire (showed with plus circle). When the ionization starts the electron and ion move toward the anode wire and the cathode, respectively (a). The electron gains enough energy for further ionization when it reaches the region close to the wire (b). The multiplied electrons are on the front of the drop toward the wire surface, and they initiate more ionization. The ions are more outside toward the cathode (c, d). Since the drift velocity of electrons is higher than the ions, the electrons are collected in a few nanoseconds, but the ions move slowly toward the cathode (e) [20].

produce a tail. A high number of ions are in the front part of the ionization cloud, since they have been produced in the last mean free path.

The amplification process is closely connected to the voltage difference V between the anode and cathode. The collected charge as a function of the voltage difference V in a gaseous detector is shown in Figure 2.4. At very low voltages the recombination process of charges is dominant so that it reduces the collected charge. The full collection of charges begins in the ionization chamber region as the voltage is increased. Above a threshold voltage, the electric field is large enough to start the multiplication process. In this region the amount of collected charge is proportional to the original deposited charge. With even higher voltage the region of limited proportionality is entered due to growing non-linear processes like the space charge and the streamer effect around the anode wire. At yet higher voltages the Geiger-Mueller region starts, where the number of collected charges becomes independent of the original charge and the full length of the anode wire is surrounded by the created electrons and ions. The number of collected charges continues to rise more slowly up to the general breakdown [20, 23].

Since straw tube detectors work in the proportional mode, the collected

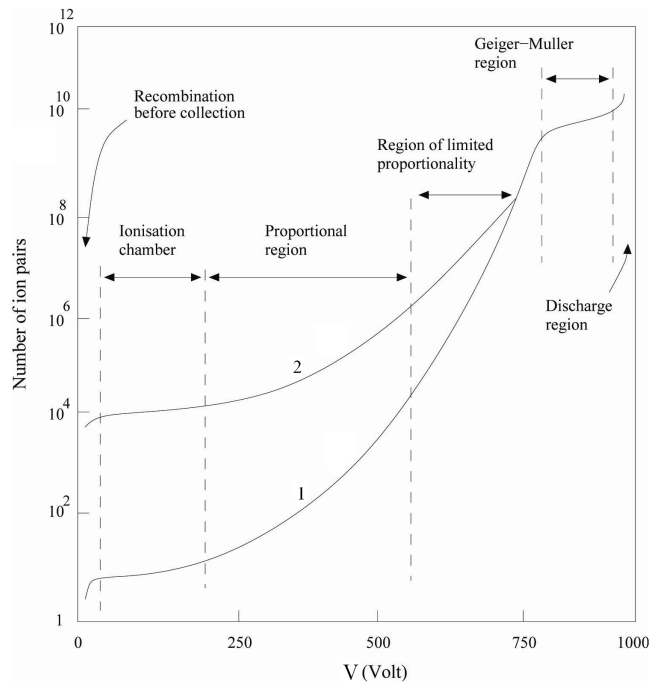


Figure 2.4: The number of collected charges as a function of the operating voltage for two different ionization densities ($2 > 1$). Different operation regions of gaseous detectors are indicated as a function of the applied voltage difference between the cathode and anode [24].

charge is directly proportional to the energy loss of the traversing particle.

2.4 Signal Creation

A charged particle traversing a straw tube makes an ionization trail of electron-ion pairs in the detector. The created charges are multiplied in the avalanche region which is in the order of $50 \mu\text{m}$ around the anode wire. Electrons are collected on the anode wire in a short time of about 1 ns. In contrast, the collection time of the ions is on the order of hundred μs . This difference is due to the low drift velocity of ions and their long distance from the avalanche region to the cathode. When the electrons and ions move toward the electrodes they cross difference of potentials. Therefore, the electric energy of the system changes, which induces a signal in the detector. Most of the electrons are produced very close to the anode in the avalanche region and they have a small contribution to the total signal compared to the ions. The ions drift a long distance from the avalanche region toward the cathode and they produce most of the signal. The ions contribution in the induced

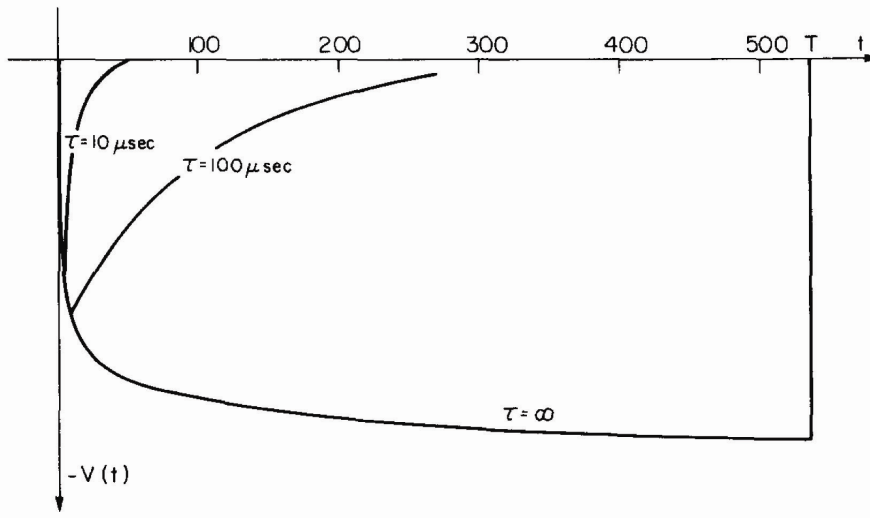


Figure 2.5: Time development of the induced voltage signal in a gaseous detector. The signal grows very fast at the beginning and continues up to the total drift time T of positive ions from the anode surface to the cathode. In order to increase the rate capability of the detector and to decrease the dead time, the differential circuit with a time constant $\tau = RC$ is used to terminate the detector. Therefore, shorter signals are obtained using a low time constant τ . Different pulse shapes with various time constants τ are shown [20].

signal is about 99% of the total signal and electrons contribution is only 1% [20]. Therefore, the time development of the signal is usually calculated only with the ions contribution. The induced signal on the anode is given by [20]

$$V(t) = -\frac{Q}{4\pi\epsilon_0 l} \ln\left(1 + \frac{t}{t_0}\right), \quad (2.15)$$

where Q is the total charge of ions, l is the detector length, ϵ_0 is the dielectric constant. The value t_0 ($= \frac{\pi\epsilon_0 P a^2}{\mu^+ C V_0}$) is a constant including the gas pressure P , the anode wire radius a , the ion mobility μ^+ , the detector capacitance per unit length C and the applied voltage V_0 between the cathode and anode. The time development of the signal induced by the drifting ions is shown in Figure 2.5. A corresponding current signal calculated as $i = dQ/dt = lC dV/dt$ is given by

$$i(t) = -\frac{QC}{4\pi\epsilon_0} \frac{1}{t + t_0}. \quad (2.16)$$

Unlike the induced voltage signal which is maximal at the end of the total drift time of the ions, the induced current signal is maximal at $t = 0$ and has a long tail due to the ions movement toward the cathode.

The induced signals in the detectors are treated by suitable front-end readout electronics. Choosing the appropriate readout electronics depends on the applications of the detector. For timing measurements fast amplifiers are needed, whereas charge measurement applications require long integration times with slower amplifiers. Signal tail cancellation and baseline restoration are also essential for high-rate applications to reduce signal pileup and baseline fluctuations [23]. Generally, most gaseous detectors need the readout electronics to satisfy the following main requirements:

- amplifying the induced signal,
- shaping the amplified signal and removing the ion tail,
- applying a threshold for timing,
- and/or integrating the signal in order to determine the collected charge.

The front-end electronics of gaseous detectors are usually composed of linear signal processing units which result in an output pulse shape $V_{out}(t)$ independent of the amplitude of the input signal $I_{in}(t)$, i.e., $V_{out}[c \times I_{in}(t)] = c \times V_{out}[I_{in}(t)]$. An amplifier is used to produce an amplified signal from the input signal. Subsequently, the amplified signal is processed by some filters called shapers to shape the output signal in order to increase the signal-to-noise ratio and decrease the pulse length. Since the long ion tail increases the dead time of the detector, an essential issue of the front-end electronics is removing the ion tail. The ion tail of the signal is usually canceled by applying pole-zero cancellation filters [23]. The tail canceled signal is then ready for timing measurement by applying a low threshold with a discriminator. The timing information is then recorded by a TDC. The information measured in TDC channels represents the response of the detector to the incident charged track and can be used later to determine the track position (see Section 6.1). To measure the charge information another circuit is needed to integrate the entire signal and the result is stored in different channels of an ADC.

2.5 Operating Gas Mixture

A suitable gas mixture for the operation of straw tube detectors should satisfy different physics requirements and environmental concerns. The operating gas mixture should provide good spatial resolution, high rate capability, long radiation length X_0 and low aging. The aging occurs due to the plasma-chemical processes in the detector during the gas amplification which deposit impurities on the electrodes. Aging causes a gradual gas gain

reduction, signal loss and finally detector breakdown. There are two main sources of aging in the straw tubes which are trace contaminations on the sub-ppm level in the gas and oxidation of the anode wire. The contaminations can be further polymerized in the high gas gain and are deposited on the electrodes. Afterwards, the increase of polymeric deposits on the electrodes can change the electric field and create sparking. The oxidation of the anode wire happens due to the penetration of oxygen through the gold cover of the wire. The oxidation increases the radius of the wire. Therefore, the gas gain decreases due to the lower electric field strength on the anode wire surface.

It is also desirable that the operating gas mixtures have some properties for safety such as chemical inactivity, non-inflammability and non-toxicity.

Noble gases satisfy most of the requirements as the basic component of the detector operating gas. Noble gases are not reactive, inflammable and toxic and they do not cause aging. Although helium as the lightest noble gas has the longest radiation length, it is not suitable for straw tubes due to its high leak rate and low drift velocity. The heavier noble gases, krypton and xenon, are not common in the atmosphere and hence they are expensive, and radon is radioactive. However, argon is more than 500 times as abundant as neon and it is the 3rd most common gas in the atmosphere which makes it cheaper than neon. Therefore, argon is one of the appropriate base gases for the operation of straw tube detectors. In addition to noble gases, polyatomic and organic gases are added to the operating gas mixture. These gases work as a quencher by absorption of the UV photons, which are produced in the avalanche region and can eject electrons from the cathode due to the photoelectric effect. The polyatomic gases used as a quencher effectively absorb the electron kinetic energy since they have different molecular vibrational and rotational modes of excitation, which result in a large mean fraction energy loss of electrons. In “cold gases” such as polyatomic gases the diffusion is small. In contrast, “hot gases” like argon have higher diffusions and hence it is difficult to obtain high spatial resolution with them. When the “hot gases” are mixed with “cold gases”, diffusion is reduced in most cases, and the drift velocity increases which is desirable in straw tube detectors.

Traditionally, a fraction of organic gases such as methane (CH_4) and ethane (C_2H_6) were used in the operating gas mixture of gaseous detectors as quenchers. However, they cause aging effects due to their polymerization on electrodes [10, 22, 25]. The polymerization does not occur for carbon dioxide. In the aging test of straw tubes at COSY for Ar + CO_2 (90 : 10) mixture no ageing has been observed up to the accumulated charge of 0.72 C/cm [10].

The gas mixture Ar + CO_2 has excellent drift properties by providing a constant drift velocity over a large electric field range, low longitudinal

diffusion and low aging. Therefore, argon as a base component and carbon dioxide as the quencher are chosen as the operating gas mixture in the straw tube detectors at the PANDA and COSY-TOF experiments.

Chapter 3

Simulation of the Straw Tube Detector Performance

3.1 Garfield Program

The simulations of the straw tube detector presented in this work are performed with the Garfield program [26]. Garfield was developed at CERN and is a tool for detailed simulations of drift chambers. It is widely used to study the properties of drift detectors as well as for their design and optimization. Garfield was developed to calculate various quantities in drift detectors such as electric field maps between electrodes, or drift of electrons and ions in electric and magnetic fields. It can be also used to simulate the charge multiplication process and the creation of signals at the detector electrodes.

Garfield has an interface to the Magboltz program [27] which calculates the electron transport properties in various gas mixtures. Garfield also has an interface to the Heed program [28] which simulates the gas ionization by traversing charged particles and the clusters statistics. In the present work, the Garfield version 7.40, the Magboltz versions 7 and 8.9.5 and the Heed version 1.01 are used to simulate operation of the straw tube detector. These versions are publicly available from CERN.

3.2 Detector Geometry

In the simulations, the straw tube is defined as a cylindrical electrode with 1 cm diameter and 150 cm length set to 0 V potential. The anode wire has a diameter of 20 μm and is placed concentrically with the straw tube. It is set to a potential of +1800 V. Figure 3.1 shows a cross section view of the straw tube with the defined structures. These structures determine the active

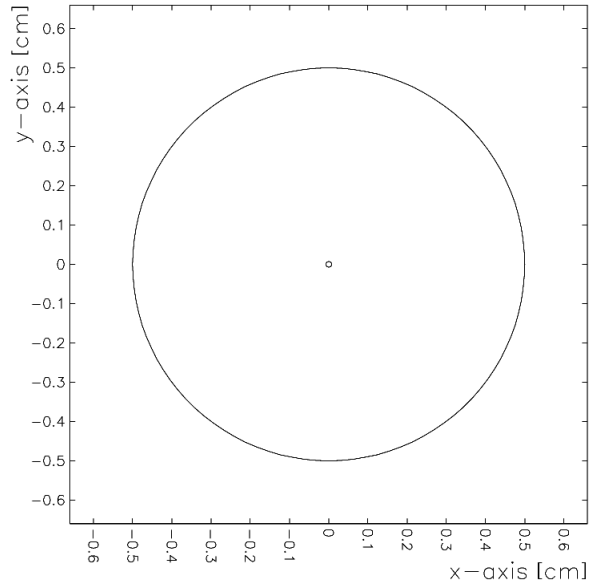


Figure 3.1: A layout of the defined straw tube which determined the active area of the simulations.

volume of the straw tube detector for further simulations of such processes as drift of electrons or avalanche development.

Ar + CO₂ mixture with a (90 : 10) volume fraction percent at 2 bar pressure and at a temperature of 300 K is chosen as the detector operating gas.

3.3 Electric and Magnetic Field Geometry

The electric field map inside the straw tube calculated with Garfield is presented in Figure 3.2. The field is cylindrically symmetric, and its strength rises rapidly in the vicinity of the anode wire. It varies inversely proportional to the distance from the wire ($E \sim \frac{1}{r}$) [20]. At the wire surface it reaches a value of about 300 kV/cm which is sufficient for avalanche development. The field strength equals 1.2 kV/cm in the drift region at half of the straw tube radius ($r/2 = 0.25$ cm) .

The magnetic field is defined for some of the simulations in this work to be 2 T oriented along the straw tube axis to take into account the PANDA solenoid field at the position of the straw tube tracker.

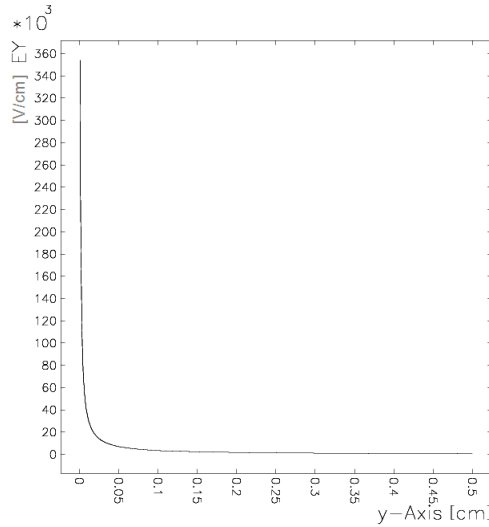


Figure 3.2: The electric field strength along the straw tube radius.

3.4 Transport Properties of Electrons and Ions Calculated with Magboltz

The components of the operating gas mixture are defined in Magboltz 7 in order to calculate the transport properties of drifting electrons and ions. The base component of the gas mixture in this study is 90% Ar in combination with 10% CO₂ which is foreseen for the PANDA straw tube tracker. The electron-impact cross sections of these components are shown in Figure 3.3. The elastic collision cross section of argon in Figure 3.3 (top) shows the Ramsauer-Townsend minimum at 0.25 eV. It also shows that the elastic collision probability for the electrons increases with higher energies. The carbon dioxide electron-impact cross section presented in Figure 3.3 (bottom) shows more different excited states and vibrational modes compared to argon.

The Magboltz program takes into account the temperature and pressure of the operating gas and the applied magnetic field to compute the transport properties of the electrons. The temperature 300 K and pressure 2 bar have been chosen in this work. The Magboltz program was used to compute for electrons the drift velocity, the longitudinal and transverse diffusion coefficients, the Townsend and attachments coefficients. Moreover, the excitation and ionization rates for the gas components are calculated. These properties are discussed in the following sections of this chapter.

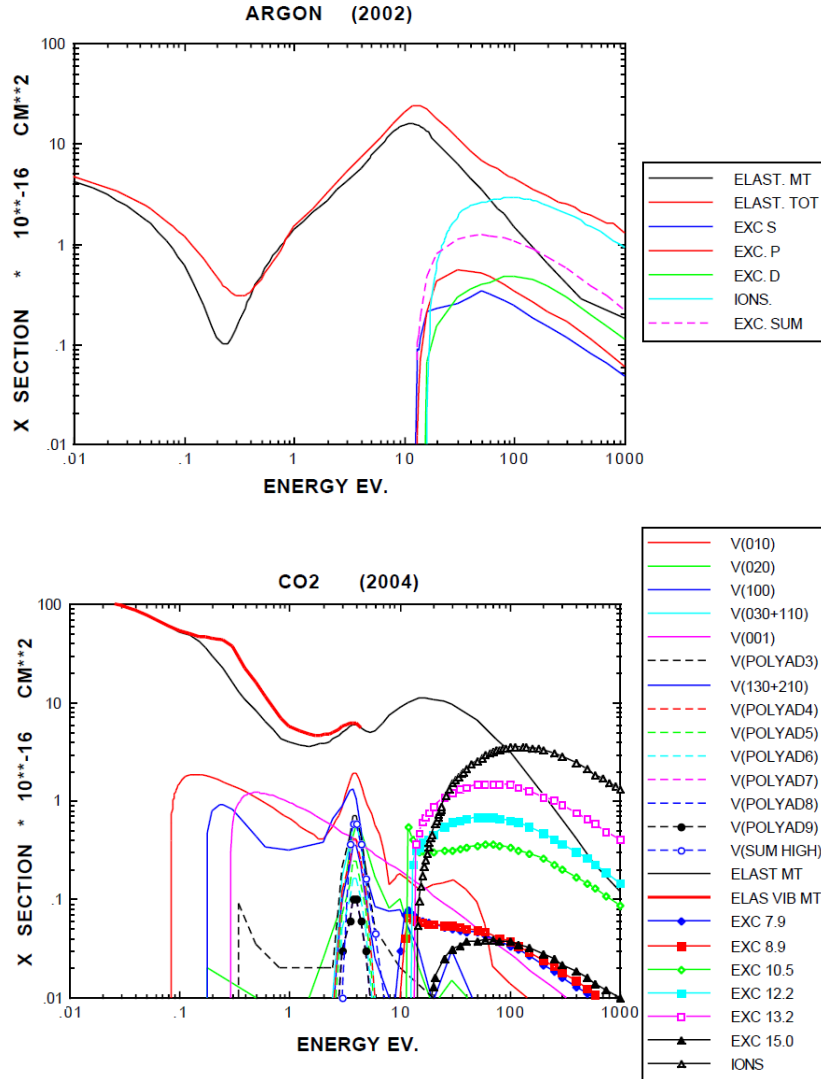


Figure 3.3: Electron-impact cross sections including the elastic scattering (momentum transfer and total), ionization and different excitations levels of argon (top) and carbon dioxide (bottom). In the top figure, the red solid line presents the total elastic cross section with visible Ramsauer minimum at around 0.3 eV. The black solid line corresponds to the momentum transfer cross section. The solid light blue line describes the ionization cross section and the remaining solid lines correspond to cross sections for excitation of different levels in Argon. The carbon dioxides electron-impact cross sections shows more excitation levels and numerous vibrational modes [26].

3.4.1 Ionization and Excitation Rates

The ionization rates and excitation rates of different states of Ar and CO₂ are simulated with Magboltz for the Ar + CO₂ (90 : 10) mixture for strong electric field in the vicinity of the anode wire with the strength up to 300 kV/cm. The ionization rates of Ar and CO₂ presented in Figure 3.4 (right) show that argon is the component which is more often ionized than CO₂ in this gas mixture. Although the ionization threshold of argon, 15.7 eV, is higher than that for the carbon dioxide, 13.8 eV, the ionization cross section for argon rises faster than CO₂, so that it slightly exceeds the cross section of CO₂. Because of the higher cross section and higher volume fraction of argon compared to CO₂, argon shows a higher ionization rate than CO₂. However, due to the charge-exchange process (see Section 2.2) CO₂⁺ is the main ion species in this gas mixture. Figure 3.4 (left) shows that also the excitation rates of argon are higher than for CO₂, but CO₂ possesses additional excitation states compared to argon since CO₂ is a molecular gas with different vibrational and rotational modes of excitation.

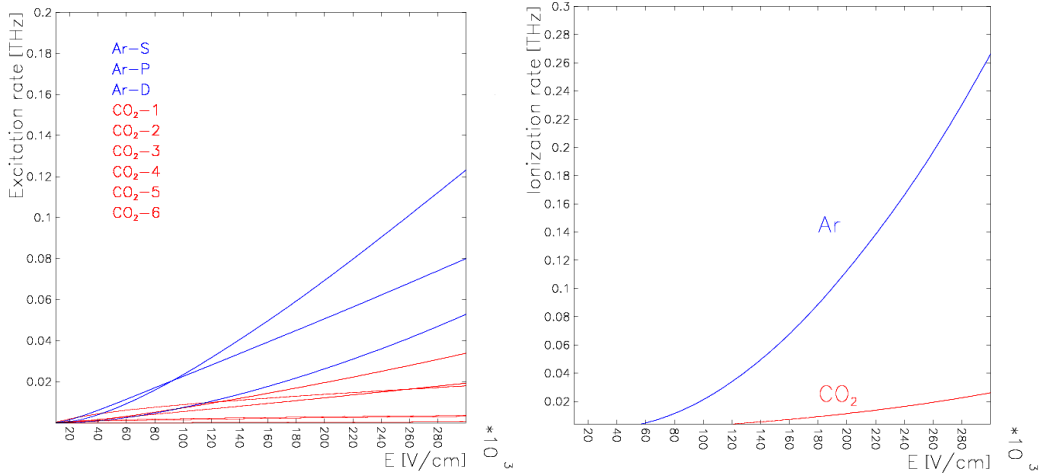


Figure 3.4: The excitation rates of different levels of the argon atoms and CO₂ molecules (left), and the ionization rates of argon and CO₂ (right) in Ar + CO₂ (90 : 10).

3.4.2 Drift Velocity of Electrons and Ions in the Straw Tubes

The simulated drift velocity of the electrons as a function of electric field for Ar+CO₂ (90 : 10) is presented in Figure 3.5 (left). The electron drift velocity

increases approximately linearly with the electric field for high electric fields in the range 20 – 340 kV/cm corresponding to the vicinity of the anode wire. However, the linear behavior of the electron drift velocity changes at lower electric field in the order of 1 kV/cm typical for the drift region in the straw tube. The Ramsauer minimum in the elastic electron-impact cross section of argon allows larger energies to be gained between collisions by electrons, and therefore, the electron drift velocity increases at low electric field. The computed drift velocity of electrons at low electric field for argon mixed with different fractions of carbon dioxide is shown in Figure 3.5 (right). Adding small amounts of CO₂ to argon leads to a significant increase of the drift velocity. This is due to the change of fractional energy loss of electrons (see Section 2.2). In addition, the Ramsauer minimum is shifted to higher energies by adding CO₂ to argon and hence the saturated drift velocity of electrons at the Ramsauer minimum is moved to higher electric fields.

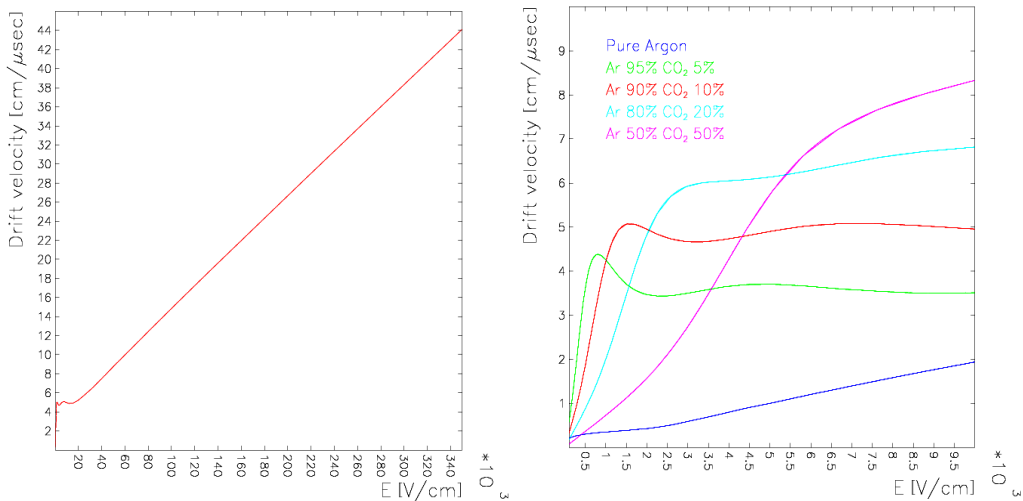


Figure 3.5: (Left) computed drift velocity of the electrons as a function of the electric field for Ar + CO₂ (90 : 10) gas mixture. (Right) drift velocity of the electrons at low electric field for argon and different fractions of CO₂.

Magboltz can only compute the transport properties for electrons, therefore the data existing for CO₂⁺ ion mobility in argon [29] is added to the gas file produced by the Magboltz program. Figure 3.6 shows that the ion mobility does not change in a wide range of the electric field since the average energy of ions is almost constant up to very high fields (see Section 2.2). In the straw tube detector with Ar + CO₂ (90 : 10) at $E = 1$ kV/cm, the CO₂⁺ ions mobility is about $0.78 \text{ cm}^2 \text{ V}^{-1} \text{ s}^{-1}$ corresponding to a drift velocity of $0.78 \cdot 10^{-3} \text{ cm}/\mu\text{s}$, and the drift velocity of electrons is about $5 \text{ cm}/\mu\text{s}$.

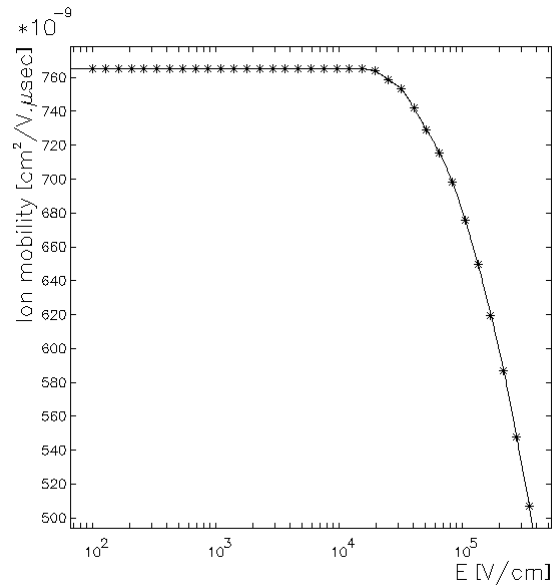


Figure 3.6: The CO_2^+ ion mobility in argon gas as a function of the electric field [29].

3.4.3 Effect of the Magnetic Field on the Drift

Applying a magnetic field changes the drift path of the electrons, so that the electrons do not follow the electric field lines due to the Lorentz force. The effect of the magnetic field on the drift path of the electrons is displayed in Figure 3.7 for $B = 0$ (left) and $B = 2$ T perpendicular to the electric field (right) in a straw tube. In this figure, a proton track of 1 GeV kinetic energy crosses the straw tube with the same direction in both cases and the drift path of the produced electrons is simulated with a Monte Carlo method in the Garfield program. The drift path of the electrons is strongly bent due to the magnetic field (Figure 3.7, right).

The minimum drift time of the electrons in the straw tube is an important parameter which is strongly affected by applying a magnetic field. Figure 3.8 shows the minimum drift time of the electrons as a function of the track distance to the straw wire called R-t curve without (left) and with (right) applying a 2 T magnetic field perpendicular to the electric field. These R-t curves show that the minimum drift time increases by about 70 ns due to the presence of the 2 T magnetic field.

3.4.4 Diffusion of Electrons

Computed standard deviation of longitudinal and transverse diffusion for 1 cm drift in argon with different admixture of carbon dioxide gas is pre-

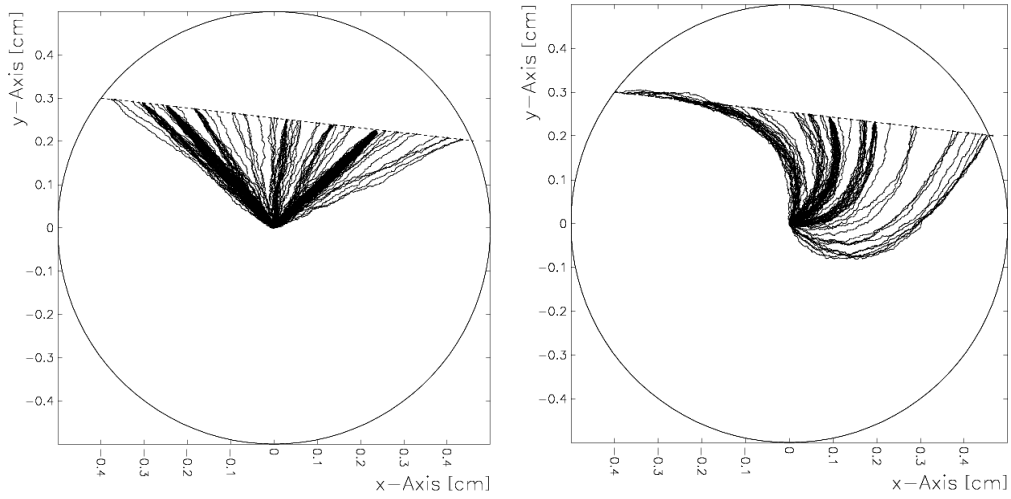


Figure 3.7: Drift path of electrons created by a 1 GeV proton in the straw tube without (left) and with applying an axial 2 T magnetic field (right).

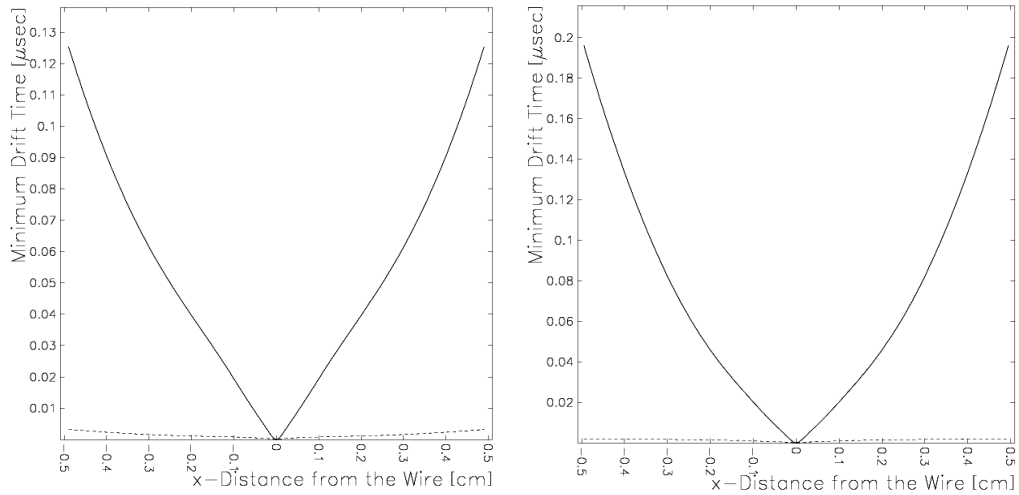


Figure 3.8: Minimum drift time of electrons vs. the radial distance to the wire in the straw tube, without (left) and with an axial 2 T magnetic field (right).

sented in Figure 3.9. The electron diffusion perpendicular to the electric field is larger than in the longitudinal direction. As Figure 3.9 shows, adding CO₂ quencher to the argon gas is an effective way to reduce both longitudinal and transverse diffusion coefficients of the electrons as explained in Section 2.2. The results show that the standard deviations of longitudinal and transverse diffusion for 1 cm drift of electron in Ar + CO₂ (90 : 10) at 2 bar and 300 K at $E = 1 \text{ kV/cm}$ is about $175 \mu\text{m}$ and $190 \mu\text{m}$, respectively.

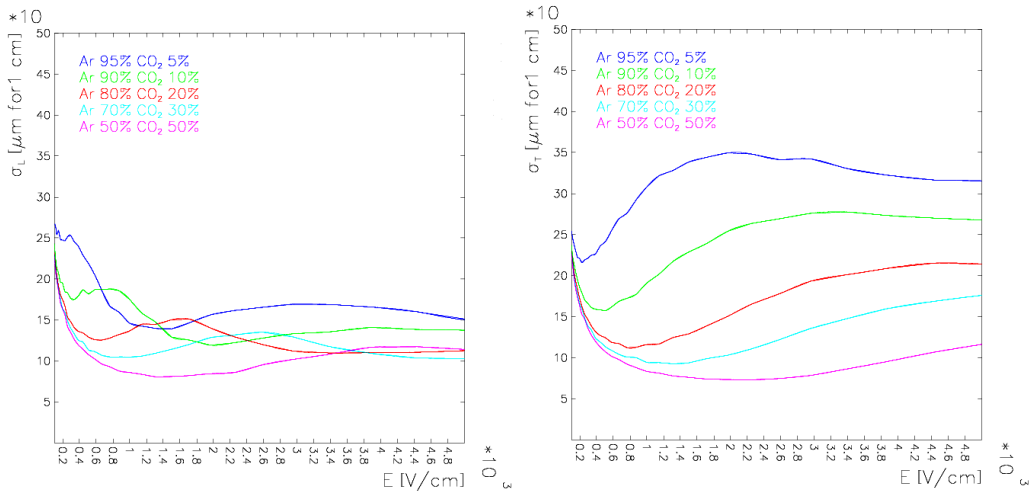


Figure 3.9: Standard deviation of electron diffusion in longitudinal direction (left) and in transverse direction (right) for argon mixed with different fractions of CO₂.

3.5 Simulation of Gas Multiplication

3.5.1 Townsend and Attachment Coefficients

In order to calculate the gas gain, the Townsend coefficient, which represents the number of ion pairs produced per unit length of drift should be known. Figure 3.10 indicates the Townsend coefficient for different ratios of argon and carbon dioxide computed with Magboltz 7. Adding CO₂ to the argon gas reduces the Townsend coefficient due to the quenching properties of CO₂, however this decline is needed in order to avoid gas discharges.

In addition to the Townsend coefficient, there is another important parameter for the gas gain calculation called the attachment coefficient, which is related to the loss of electrons drifting in gas due to attachment to gas molecules. The number of electrons is reduced by [20]

$$\frac{n}{n_0} = \exp\left(\int_{r_0}^{r_1} (\alpha(r) - h(r)) dr\right), \quad (3.1)$$

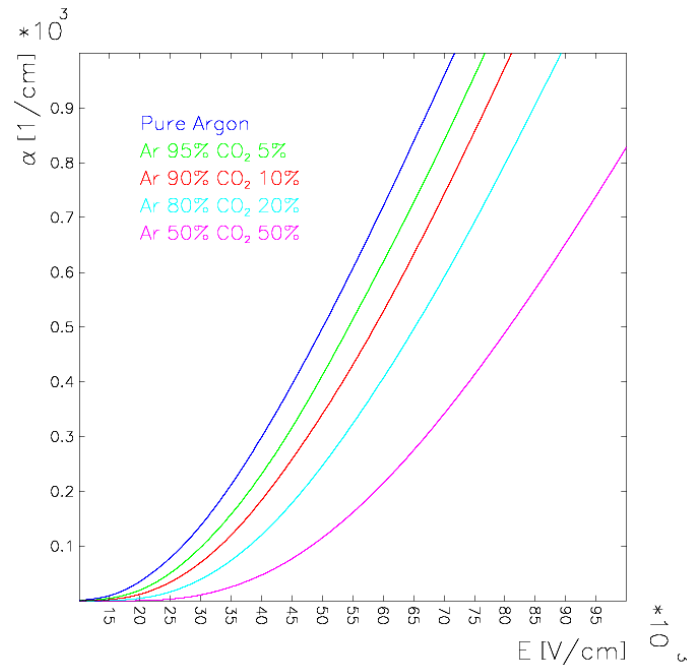


Figure 3.10: Computed Townsend coefficient for different fractions of argon and carbon dioxide using Magboltz 7 without including the Penning transfer.

where n_0 is the original number of electrons, n is the number of electrons after the path r , α is a Townsend coefficient and h is the attachment coefficient. Noble gases do not attach electrons, but CO_2 molecules attach electrons if their energy is in the range of 4–10 eV [25]. In Ar+ CO_2 (90 : 10) this energy is reachable for electrons at distances from anode wire smaller than $r = 0.1$ cm corresponding to electric field strength higher than $E = 2.8$ kV/cm, hence the attachment losses are significant in the avalanche area. Since the electron attachment losses start at larger distances from the wire than the avalanche, the ionization electrons can be lost by attachment before reaching the avalanche region. Therefore, it is important to use a gas mixture with low attachment coefficient. Figure 3.11 presents the computed attachment coefficient in Ar with different fractions of CO_2 . As Figure 3.11 shows adding CO_2 to the argon gas increases the attachment coefficient.

3.5.2 The Penning Effect

The Townsend coefficient computed with the Magboltz program underestimates experimental values of the gas gain. This is due to neglecting some indirect ionizations called the Penning effect involved in the gas multiplication process. In addition to the direct ionization of the components in the

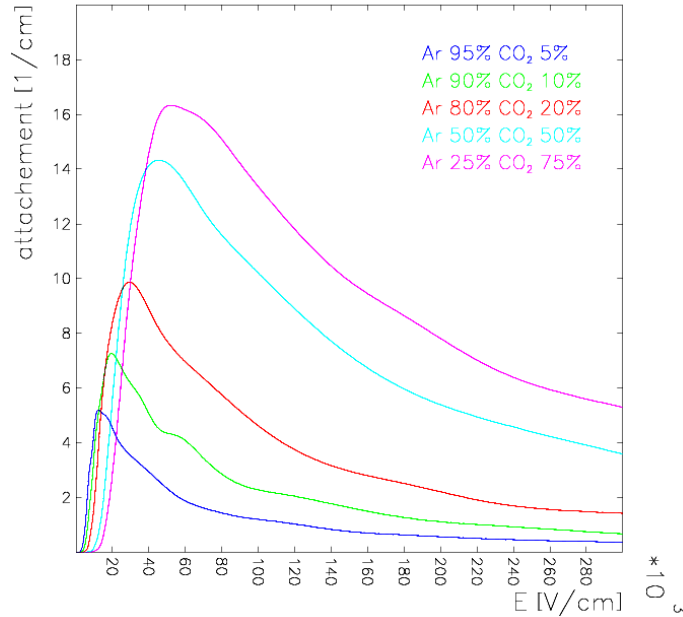


Figure 3.11: The attachment coefficient for argon mixed with different fractions of CO₂, computed with Magboltz 7.

gas mixture, the excitations of gas atoms or molecules also happen. The Penning effect converts a fraction of the energy, lost in excitation, into ionization. If the excited atoms or molecules have a higher energy than the ionization threshold of the gas components, their excitation energy can be transferred to ionization. This energy transfer can be done locally by direct collisions between particles within a few nanometers surrounding the original excitation point, or non-locally by photon emission with absorption lengths of about $1 \mu\text{m}$ [30, 31]. These two energy transfer processes are indistinguishable in the simulation. In Ar + CO₂ (90 : 10) the excitation energy of D-level of Ar, 14 eV, exceeds the ionization threshold of the CO₂ molecules, 13.77 eV. Hence the Ar* transfers its excess energy to CO₂ molecules which in turn become ionized. The Penning effect for Ar + CO₂ (90 : 10) is estimated to be about 30% between excited argon and carbon dioxide molecules [31].

The Penning effect can be accounted in the Magboltz simulation by applying a correction to the Townsend coefficient. The excitation collision frequencies of argon with energies above the ionization threshold of CO₂ molecules are included in the Townsend coefficient calculation. The Townsend coefficient α^{corr} corrected for Penning transfer effect is given by

[31]

$$\alpha^{corr} = \alpha \left(1 + \frac{\sum_i r_i v_i^{exc}}{\sum_i v_i^{ion}} \right), \quad (3.2)$$

where α is the uncorrected Townsend coefficient, r_i is the Penning transfer rate and v_i^{exc} (v_i^{ion}) are the excitation (ionization) frequencies of argon for different levels. Only the excitation frequencies of states eligible for transfer are considered in Equation 3.2. The complete argon excitation frequencies can be computed only by Magboltz version 8.9.5 updated for the argon cross section. The Penning effect rate is calculated to be 34% in this work for Ar + CO₂ (90 : 10) at 2 bar pressure and 300 K temperature. Using this transfer rate a good agreement is achieved between simulated gas gain and the available experimental data which is shown in the next section. The computed Townsend coefficient without the Penning transfer rate and including the Penning effect is shown in Figure 3.12 for Ar + CO₂ (90 : 10). Since the Penning transfer is dependent on the electric field, it starts to effect on the Townsend coefficient at $E \approx 30$ kV/cm in this gas mixture.

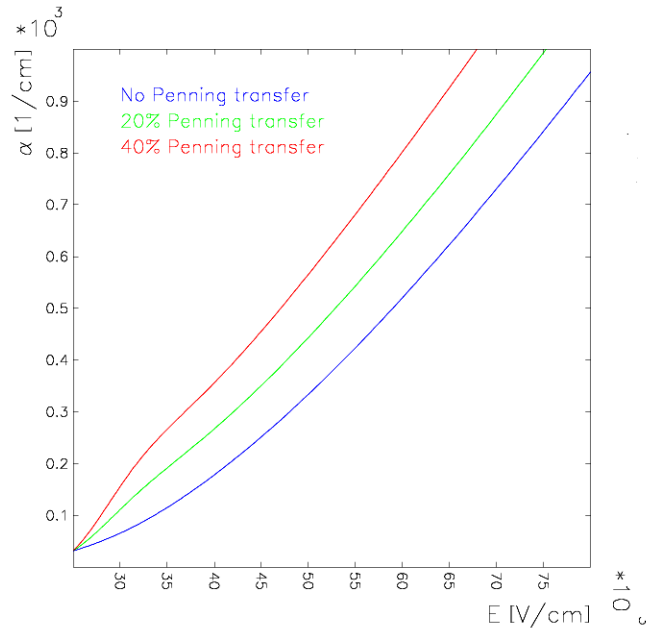


Figure 3.12: The Townsend coefficient without and with 20% and 40% Penning transfer rate for the Ar + CO₂ (90 : 10) mixture.

3.5.3 Gain Simulation

The computed gas gain for Ar + CO₂ (90 : 10) is presented in Figure 3.13 without the Penning effect and including 34% Penning transfer rate. The

computed gains are compared with the experimental gain data at the same temperature and pressure. The experimental gain is determined by simultaneous measurement of the current of single straw tube and the count rate from the ^{55}Fe source. An agreement between experimental data and computed gain is found with about 34% Penning rate contribution.

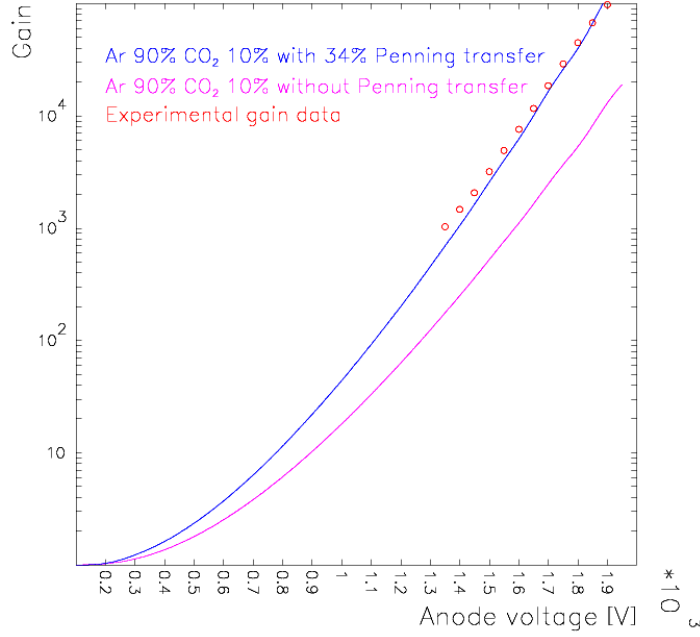


Figure 3.13: The gas gain curves for Ar + CO₂ (90 : 10) without and with 34% Penning transfer rate, purple and blue curves, respectively. The computed gains are compared with experimental data (open red circles).

In addition, the experimental gain data and computed gas gains are compared with the Diethorn gas gain parametrization as a function of the applied high voltage to the anode wire. The Diethorn gas gain is given by [23, 32]

$$G = \left(\frac{V}{a \ln(b/a)} \frac{1}{E_{min}} \right)^{\frac{\ln 2}{\Delta V} \frac{V}{\ln(b/a)}}, \quad (3.3)$$

where V is the anode voltage, a and b are the wire and tube radius, respectively. E_{min} and ΔV are Diethorn's parameters for Ar + CO₂ (90 : 10) mixture [33]. As Figure 3.14 shows, there is a good agreement between the obtained gas gains from the results of the Garfield simulation, the Diethorn formula and experimental measurement at low voltages. However, the agreement is lost at higher voltages above +1850 V due to the growth of space

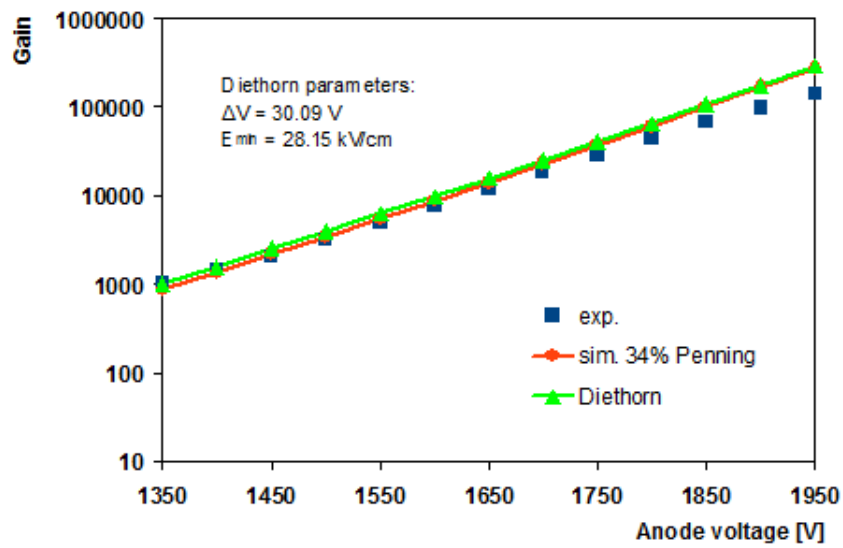


Figure 3.14: The gas gain in a straw tube filled with $\text{Ar} + \text{CO}_2$ (90 : 10) computed with Garfield (red), Diethorn formula (green) and the experimental measurement (blue). The parameters used in Diethorn formula are indicated in the plot.

charge effect that reduces the experimental gas gain and is not included in the simulations.

Chapter 4

Particles Identification with Straw Tube Detector

4.1 Cluster Statistics

Secondary electrons released by a primary ionization electron are localized close to the point of the primary ionization. Therefore, such a group of secondary electrons together with the primary electron is called a cluster. The cluster statistics is computed with Heed through the Garfield program. Figure 4.1 shows the number of clusters per cm of track and the cluster size distribution for $0.5 \text{ GeV}/c$ proton tracks crossing a straw tube filled with Ar + CO₂ (90 : 10) at 300 K and 2 bar. The number of clusters in Figure 4.1 (left) follows Poisson statistics and indicates that about 60 clusters are created per cm of a $0.5 \text{ GeV}/c$ proton track. The cluster size distribution in Figure 4.1 (right) shows a rapid fall at small sizes and after that there are other bumps. The second bumps are related to the interactions with electrons in the K, L and M shells. Even larger cluster sizes correspond to δ -electrons.

4.2 Simulation of Straw Tube Output Signal

A detailed simulation is performed to determine the induced currents from different tracks traversing the straw tube. The induced current in the straw wire is simulated with Garfield. The script to simulate the straw tube signal is presented in appendix A. The simulation of the induced signal of a proton track at $0.5 \text{ GeV}/c$ in a single straw tube with a high voltage of +1800 V applied to the anode wire corresponding to a gas gain of $4.4 \cdot 10^4$ is presented in Figure 4.2. The simulated signal indicates very fast electron component and a long ion tail showed up to $1 \mu\text{s}$. The long ion tail in the straw signal

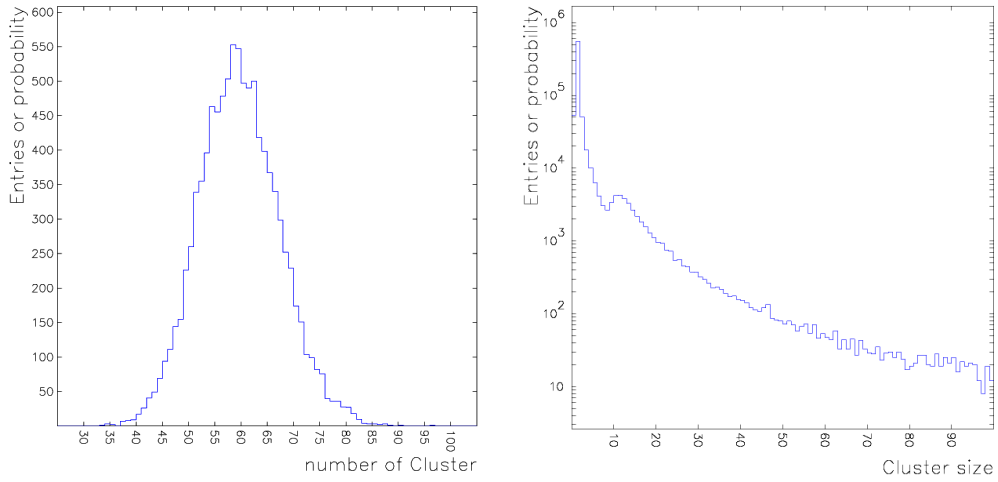


Figure 4.1: (Left) number of clusters per cm produced by a $0.5 \text{ GeV}/c$ proton track in $\text{Ar} + \text{CO}_2$ (90 : 10) at 2 bar and 300 K. About 60 clusters per cm are produced on average. (Right) cluster size distribution is shown; most of the clusters have a size smaller than 10 electrons.

has to be removed using appropriate front-end electronics, since it leads to pileup and results in baseline shift and increases the dead time of the detector. The amplitude of the straw output signal is small. Therefore, suitable front-end electronics is needed to amplify the output signal of the straw tube and to shape it.

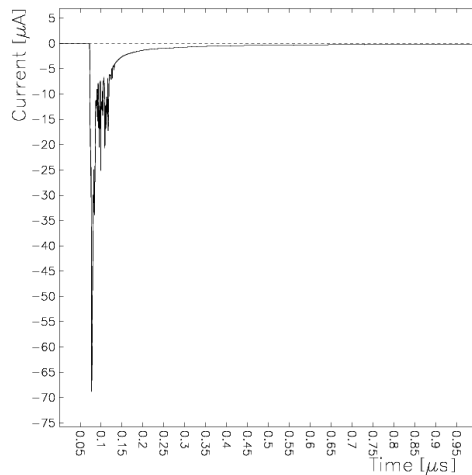


Figure 4.2: The simulated induced current signal in the straw wire by a proton track at $0.5 \text{ GeV}/c$. The long tail is related to the ions moving slowly toward the cathode. The ion tail is indicated up to $1 \mu\text{s}$.

4.3 Convoluted Signal and Transfer Function

In order to include the front-end electronics response in the simulations, straw tube signals simulated with Garfield are convoluted with the transfer function of the front-end electronics. The transfer function in the Fourier domain is equal to the ratio of the Fourier transforms of the output and input signals as

$$w(i\omega) = \frac{V_{out}(i\omega)}{I_{in}(i\omega)}. \quad (4.1)$$

In the time domain the output signal can be expressed as a convolution of the transfer function and the input signal as

$$V_{out}(t) = \int_0^{\infty} w(t-t')I_{in}(t') dt'. \quad (4.2)$$

The transfer function is determined experimentally by injection of a “delta-like” pulse into the front-end channel. The response of the front-end electronics to the delta pulse is directly the transfer function, since for $I_{in}(t) = \delta(t)$ the integration in Equation (4.2) results in $V_{out}(t) = w(t)$. The

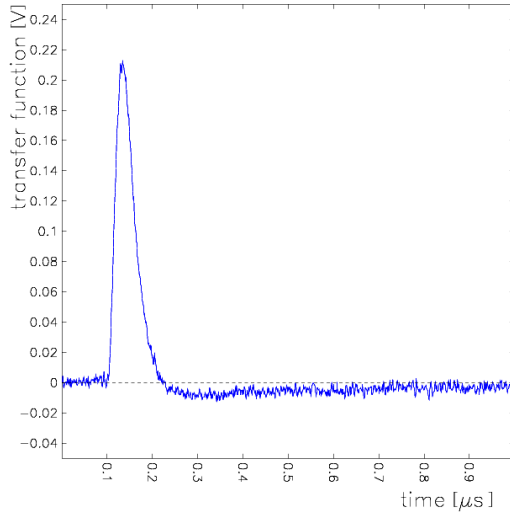


Figure 4.3: Transfer function of the first prototype front-end electronics developed for the PANDA straw tube tracker and used in the simulations in this work.

transfer function of the prototype front-end electronics for the straw tubes in the PANDA experiment is shown in Figure 4.3.

4.4 Particle Identification Methods

The particle identification in a straw tube detector is done based on the specific energy loss information. For registration of the energy losses in the PANDA trackers we consider usage of the Time Over Threshold (TOT) technique as an alternative to more conventional method of integration of the straw tube signal. Using the TOT technique for particle identification in straw tubes is discussed for the first time in the ATLAS experiment [34]. This technique is based on the fact that the energy loss of charged particles in a straw tube is related to the width of the signal above a given threshold, so that the signals with larger amplitudes have larger widths. Therefore, the TOT can be used for particle identification. The TOT technique is desirable because the readout electronics can be restricted simply to the time measurements, whereas the charge measurement needs a more complicated readout electronics with a large data band width and with more power consumption. The TOT measurement might be disturbed by pile-up and fluctuation of the baseline in the front-end electronics which result from imperfect ion tail cancellation. However, using an appropriate front-end electronics TOT can work very well even in high rate experiments such as PANDA with counting rates reaching up to 800 kHz per straw tube [17].

4.4.1 Track to Wire Distance Correction

The TOT depends on the track distance to the anode wire. When a charged particle passes the straw tube far from the anode wire, the produced clusters along the track have similar drift times to reach the wire, and therefore, the produced signal is narrow. On the other hand, for charged particles that pass close to the anode wire the drift time to the wire is shorter for the clusters created close to the center of tube than that ones created close to the tube wall. Hence the produced signal width is wide. Figure 4.4 shows a sketch of the signals and the time over thresholds created by charged particles crossing a straw tube close and far from the anode wire.

In order to use the TOT information for particle identification, the TOT has to be corrected for the track to wire distance using the procedure described in Ref. [34]. For this aim, the TOT is simulated for pseudo-tracks created by randomly combining 24 hits generated with Garfield, assuming a uniform distribution of the track distance to the anode wire. A Gaussian function is fitted to the TOT distribution to determine the mean and the standard deviation of the distribution. The TOT dependence to the track positions in the straw tube is then parameterized using a second order polynomial function $p_0 + p_1 \cdot x + p_2 \cdot x^2$ fit to the TOT values which are within $\pm 2\sigma$ of the mean TOT. Subsequently, all TOT data are normalized to the

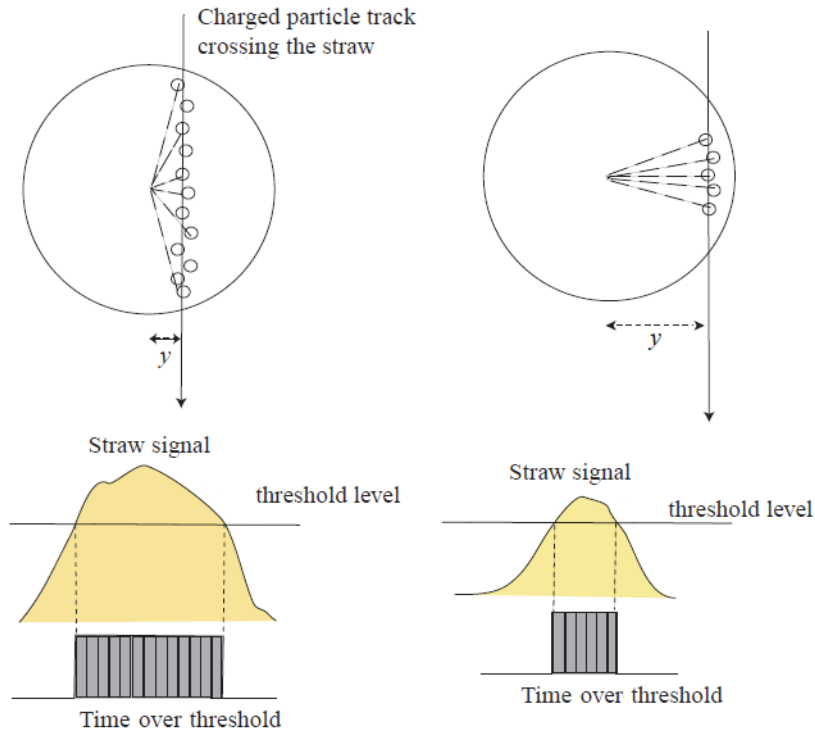


Figure 4.4: Signal created by a charged particle crossing the straw tube close to the anode wire (left) and far from the wire (right). In the first case the TOT is longer than in the second case [35].

fitting parameter p_0 in order to apply the correction for the track distance to wire. Figure 4.5 shows the simulated TOT distribution as a function of the track distance to the anode wire for protons, charged kaons and pions at $0.5 \text{ GeV}/c$ before and after applying the distance correction. The time over threshold distributions after applying the track to wire distance correction have the same average value for all distances.

4.4.2 TOT in a Single Straw and Truncated Mean

Studying the single straw response shows that even after applying the distance correction it is impossible to identify particles due to too high statistical fluctuations of the energy loss. However, performing a multiple measurement of the energy loss of a charged track significantly reduces these fluctuations. In addition, the truncated mean procedure is applied to reject a fraction of tubes with the highest values of the energy loss corresponding to the tail of the Landau distribution. Therefore, particle identification in straw tubes is studied by taking the responses of 24 straws hit by charged

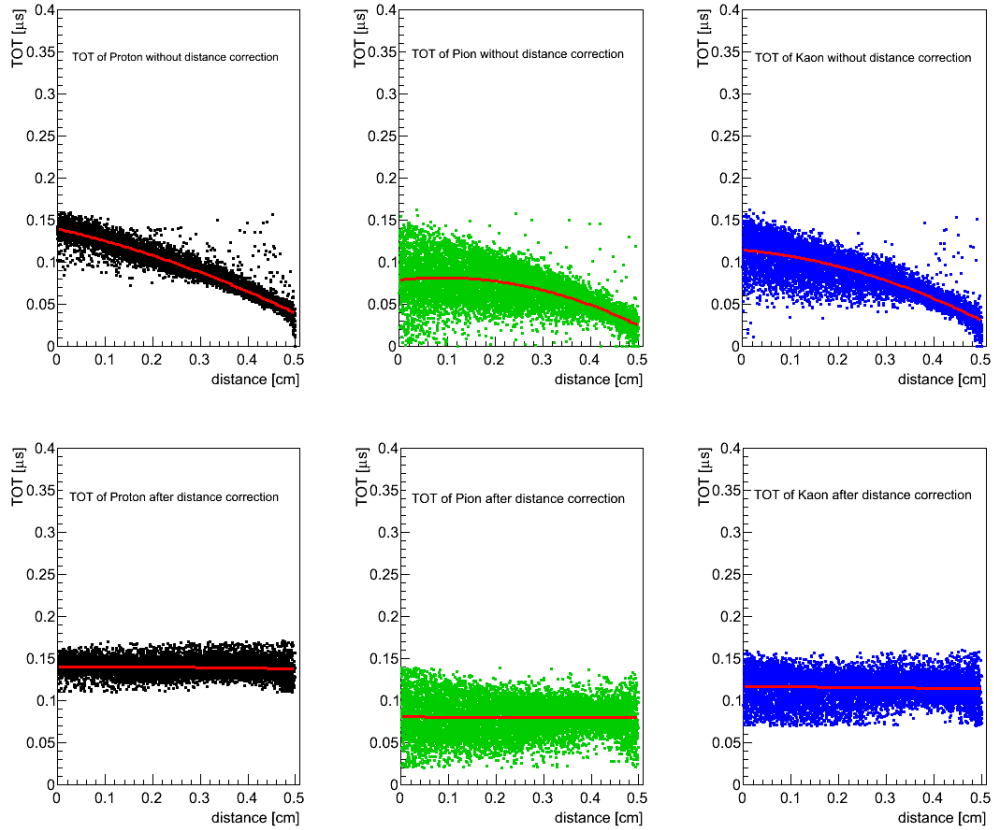


Figure 4.5: TOT vs. distance between the track and the anode wire for protons (left), pions (middle) and kaons (right) at $0.5 \text{ GeV}/c$, before (top) and after applying the distance correction (bottom). The simulations are done for the anode wire at $+1800 \text{ V}$ and a discrimination threshold for the TOT measurement equivalent to 20 primary electrons. The solid red lines indicate the second order polynomial fits to the TOT distributions.

tracks which is close to the numbers of straw tube layers in the PANDA straw tube trackers. Figure 4.6 (top) shows the time over threshold simulation for a single straw tube for protons, pions and kaons at $0.5 \text{ GeV}/c$ after applying the distance correction. The truncated mean of TOT for 24 straw tubes after discarding the 30% with the highest values is presented in Figure 4.6 (bottom). The mean and sigma values of the Gaussian fit to the TOT distributions for the single straw tube and the truncated mean for 24 straws are summarized in Table 4.1. The results show that application of the truncated mean substantially improves the TOT resolution compared to the results for single straws. Besides, it allows a very good separation of the $0.5 \text{ GeV}/c$ protons, kaons and pions.

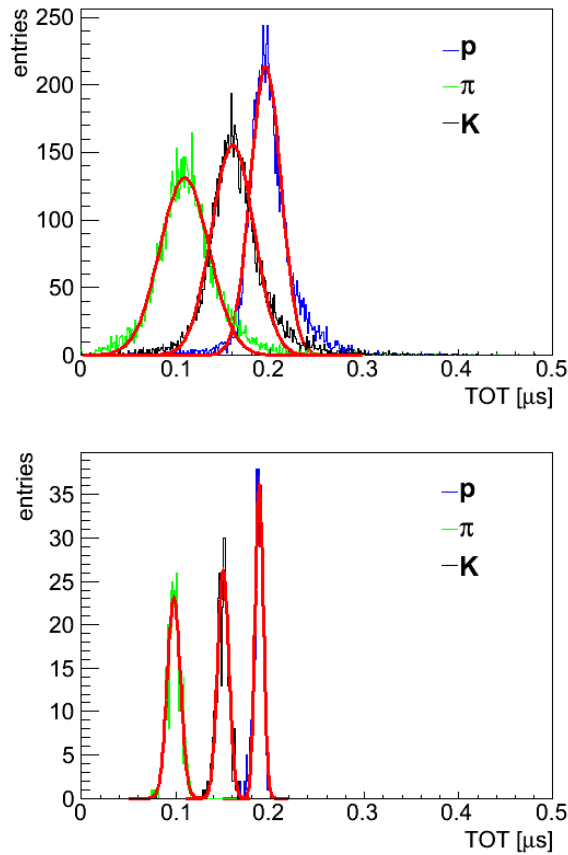


Figure 4.6: TOT simulation with single straw response (top) and truncated averaged on 24 straws (bottom) for proton and charged pion and kaon with $0.5 \text{ GeV}/c$ momentum. Solid red lines show the Gaussian fit to the distributions. The protons, charged kaons and pions are well distinguished using distance corrected TOT after applying the truncated mean by discarding the 30% of the largest values.

Table 4.1: The Gaussian fit parameters to the TOT distributions of a single straw and the truncated mean of 24 straws.

particle	TOT [μs]	σ [μs]	$\overline{\text{TOT}}_{24}$ [μs]	$\bar{\sigma}_{24}$ [μs]
π	0.109	0.026	0.979	0.007
K	0.160	0.022	0.150	0.006
p	0.195	0.016	0.188	0.004

4.5 Prototype Straw Tube Detector

In order to examine the simulation results, test measurements have been done with prototype straw tube detector developed at the Jagiellonian University for the PANDA Forward Tracker. It consists of 32 straw tubes in a double layer structure.

Figure 4.7 shows the prototype straw tube detector which is set up with scintillators to provide timing measurements. The prototype straw tube is read out by the new front-end electronics designed for the PANDA STT. The drift time and the TOT information are registered with the TRB.v2



Figure 4.7: Prototype straw tube tracker developed at the Jagiellonian University for the PANDA Forward Tracker. The scintillator detectors are used to provide timing measurements.

time-to-digit converter [36]. The TOT measurement is done using an ^{55}Fe radioactive source placed several cm from the straw tubes. The results of measurements are compared with the TOT simulated with Garfield. The discrimination threshold level in the front-end discriminator is set to 10% of the ionization corresponding to 20 electrons for both the simulation and the experiment. A voltage of +1800 V is applied to the anode wire which corresponds to a gas gain of $4.4 \cdot 10^4$. In addition, a Gaussian electronic noise with a level observed in the measurements is added to the simulated signals. A comparison between the simulated TOT spectrum and the measured one for ^{55}Fe is shown in Figure 4.8. A reasonable agreement is observed between the simulated and measured TOT spectra. The narrower distribution of the simulated TOT compared to the measured one is presumably due to imperfect approximation of the electronic noise.

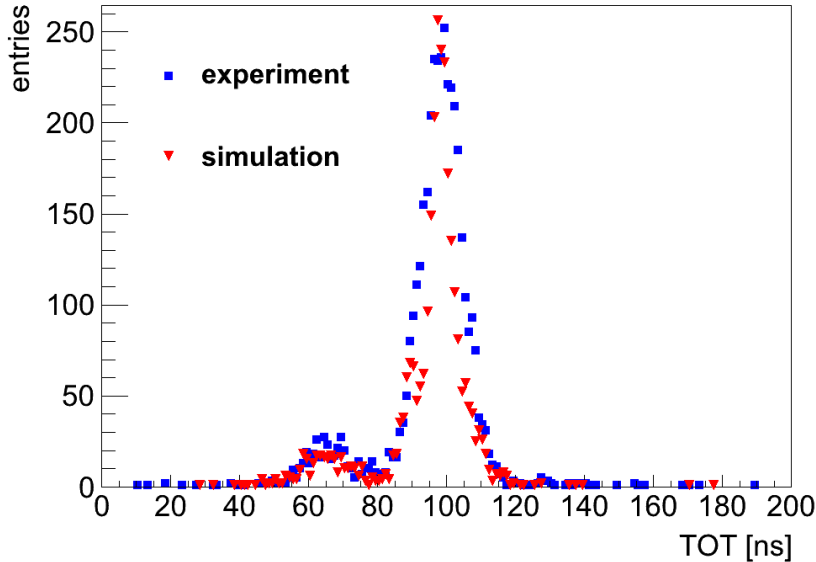


Figure 4.8: TOT spectrum measured and simulated for ^{55}Fe with the discrimination threshold set at about 10% of the primary ionization. The strong right peak corresponds to the full absorption of the 5.9 keV X-rays from the ^{55}Fe , and it is clearly separated from the 2.9 keV argon escape peak on the left [17].

Furthermore, the simulated TOT as a function of the integrated charge is compared to the test results for different high voltages in the range of 1600 V to 2000 V (see Figure 4.9). The charge information is obtained by integrating the convoluted straw signals over a time interval of $1 \mu\text{s}$. As Figure 4.9 shows, the dependence between the time over threshold and the integrated charge is nonlinear. This is because contrary to the integrated charge, the TOT is not linearly proportional to the energy loss. The TOT versus dE/dx (or Q)

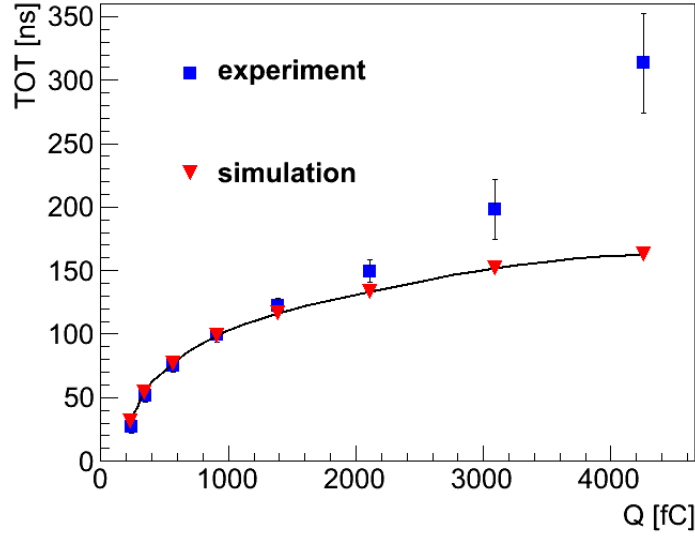


Figure 4.9: TOT vs. the integrated charge for ^{55}Fe for voltages from 1600 V to 2000 V. The integration of charge is done up to $1\ \mu\text{s}$. Due to saturation of the signals in the shaper, the experimental results deviate from the simulation.

relation depends on the pulse shape and on the setting of the discrimination threshold. At low integrated charges there is a good agreement between the simulation and the experimental results of the TOT. However, the agreement is lost for large amount of charges due to the saturation of the signals in the shaper stage, which is not included in the TOT simulation with Garfield.

4.6 Efficiency of TOT Measurement

The efficiency of the TOT measurement is given by the fraction of charged particles producing signals above the defined threshold level according to formula

$$Eff_{TOT} = \frac{(N_t - N')}{N_t}, \quad (4.3)$$

where N_t is the total number of signals and N' is the number of signals that do not pass the threshold. In order to determine the TOT efficiency the straw tube radius is divided into 10 bins with 0.5 mm width each. The TOT for pseudo-tracks of $0.5\ \text{GeV}/c$ protons, charged kaons and pions at thresholds equivalent to 10 and 20 primary electrons is simulated for each tube radius bin and the TOT efficiency is calculated using Equation 4.3. The TOT efficiencies for $0.5\ \text{GeV}/c$ proton, kaon and pion tracks are shown in Figure 4.10. Most of the signals produced by these tracks pass the defined

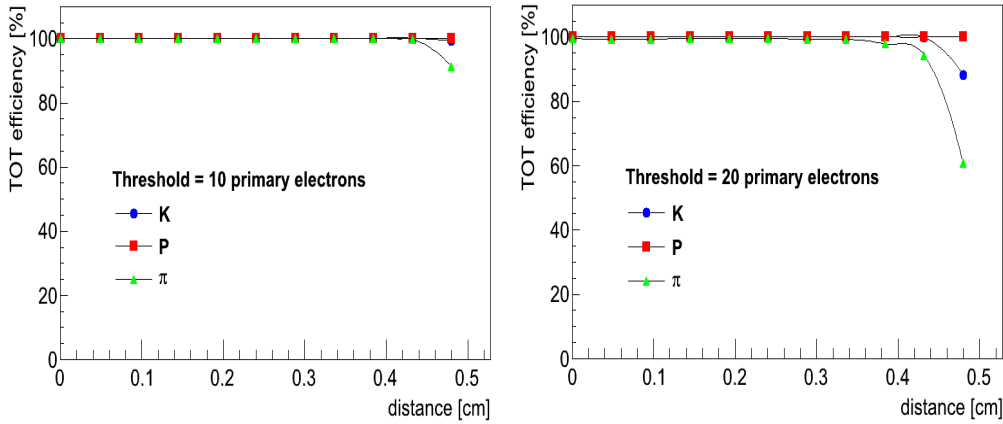


Figure 4.10: Simulation of TOT efficiency for proton and charged kaon and pion tracks at 0.5 GeV/c as a function of distance to anode wire at a threshold level equal to 10 primary electrons (left) and 20 primary electrons (right).

thresholds and the efficiency is close to 100% at all distances. However, the efficiency drops close to the tube wall as expected, since the path length of the tracks is small in this area and low height signals are produced. This is more significant for low ionizing particles as charged pions than for protons and kaons.

4.7 $p - K - \pi$ Separation Power

The particle identification capability of the straw tubes is based on the fact that the response of the detector is sufficiently different for particle species. The particle identification capability of straw tubes with TOT and integrated charge technique is quantified by the separation power defined as [17, 37]

$$\text{separation} = \frac{|\langle M_A \rangle - \langle M_B \rangle|}{(\sigma_A + \sigma_B)/2} \quad (4.4)$$

where $\langle M_A \rangle$ and $\langle M_B \rangle$ are the mean TOT (or integrated charge) values for the tracks and $\sigma_{A,B}$ are the corresponding standard deviations.

Simulation of the particle identification in the straw tubes is performed for the TOT and the integrated charge information from pseudo-tracks of protons, charged kaons and pions. The simulations are done for 24 straw hits and the TOT is measured at a threshold equivalent to 20 primary electrons. Both TOT and integrated charge are corrected for the distance of the track to the wire, and the truncated mean is calculated for each track by removing

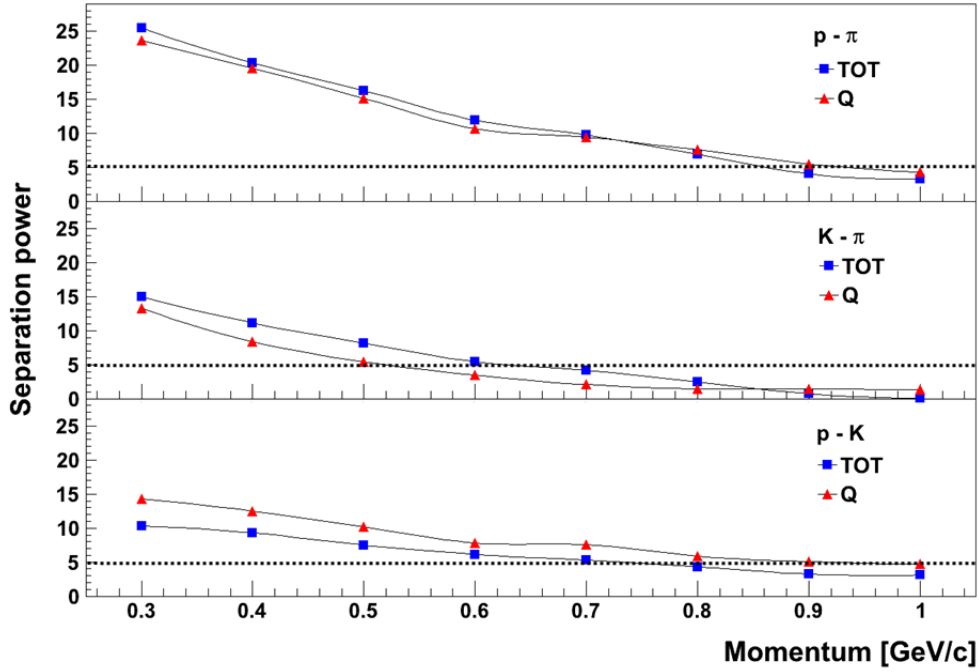


Figure 4.11: Separation power for $p - \pi$, $\pi - K$ and $p - K$ pairs based on time over threshold and charge integration methods for tracks in the momentum range 0.3 – 1.0 GeV/c. The dashed lines show the required 5σ separating to identify the particles in the PANDA experiment [17].

the 30% of hits with the largest values. The truncated mean values are then used to calculate the separation power for the TOT and integrated charge measurements with Equation 4.4. The separation power results for $p - \pi$, $p - K$ and $\pi - K$ pairs are shown in Figure 4.11 as a function of the particle momentum in the range of 0.3 GeV/c to 1.0 GeV/c.

The results indicate that the $p - \pi$ separation power is comparable for both TOT and charge methods in the momentum range 0.3 – 1.0 GeV/c. However, there are some differences between the separation power calculated using TOT and charge for $\pi - K$ and $p - K$ pairs. These differences are mainly due to the saturation of TOT as a function of the integrated charge for the large energy deposits of proton and kaon tracks in the straw tubes. The TOT vs. integrated charge for proton and charged kaon and pion at 0.3 GeV/c and 0.7 GeV/c is shown in Figure 4.12. The saturation of the TOT leads to the smaller smearing of the TOT mean values than for the charge, and therefore increases the separation power calculated with the time over threshold method.

The TOT from the kaon and proton tracks is saturated in the momentum

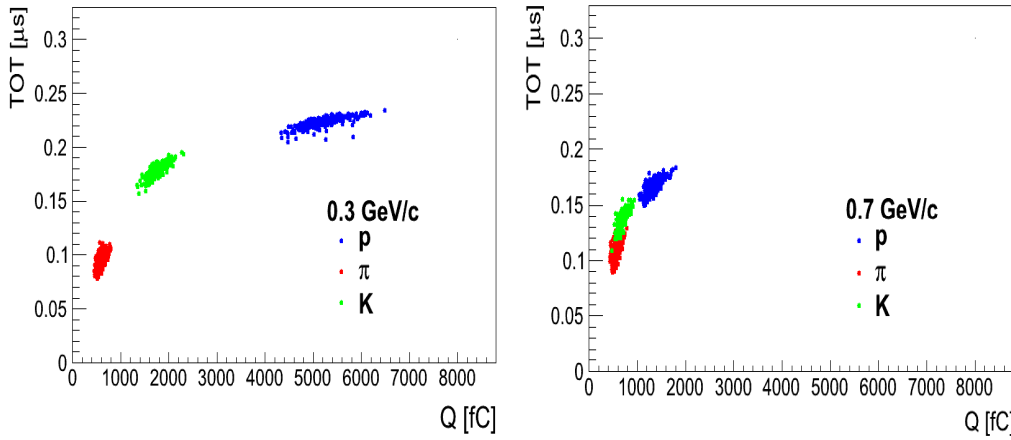


Figure 4.12: TOT as a function of the integrated charge for protons, charged kaons and pions at $0.3 \text{ GeV}/c$ (left) and $0.7 \text{ GeV}/c$ (right) [17].

range of $0.3 - 0.7 \text{ GeV}/c$ due to the relatively large deposited energy of these particles in the straw tubes compared to pions. For the $\pi - K$ pairs, the TOT from kaons is close to saturation which results in increasing the separation power for the TOT compared to that for the integrated charge. On the other hand, for two particles with TOT in the saturation region, the differences between the TOT mean values become small compared to the charge which lead to a decline in the separation power based on TOT. In the case of the $p - K$ pair, the separation power of TOT falls behind that for the integrated charge due to the saturation of both protons and kaons [17].

Although the saturation effects in the TOT measurements, the particles identification with the TOT and the integrated charge method presents similar performance for the straw tube detector in the range below $0.6 \text{ GeV}/c$ for the $\pi - K$ and below $0.8 \text{ GeV}/c$ for the $p - \pi$ and $p - K$ with a 5σ separating as required in the PANDA experiment.

Chapter 5

The COSY-TOF Experiment

The main application of straw tube detectors in experiments such as PANDA and COSY-TOF is tracking of charged particles. Because the PANDA detector is still under construction, the tracking performance of the self-supporting straw tube detectors is studied in the COSY-TOF experiment with data taken for hadron physics measurements. The following chapters focus on the COSY-TOF experiment and the analysis of data from measurements of the $pp \rightarrow pK^+\Lambda$ reaction using the straw tube tracker in the COSY-TOF detector.

5.1 The COSY Facility

The COSY accelerator facility is a COoler SYnchrotron and storage ring located at the Jülich Research Center in Germany. COSY delivers high precision beams with up to $3 \cdot 10^{10}$ protons and covers the momentum range from $300 \text{ MeV}/c$ up to $3.7 \text{ GeV}/c$ for medium energy physics experiments [38, 39, 40]. COSY is designed to study the production of hadrons close to the production threshold and at higher excess energies above threshold [41, 42]. Hadron physics studies provide information about the structure, the interaction and the decay of hadrons, which lead to a better understanding of the quark interactions, as well as the symmetries of nature and their breakings [38, 40, 43, 44].

COSY can accelerate both unpolarized and polarized proton and deuteron beams. The particles are preaccelerated in the injector cyclotron JULIC up to a momentum of $0.3 \text{ GeV}/c$ for protons and $0.55 \text{ GeV}/c$ for deuterons. COSY subsequently accelerates these particles up to $3.7 \text{ GeV}/c$. Furthermore, two cooling systems are used to improve the phase space density and to reduce the momentum spread of the circulating beam. The electron cooling is used at injection energy and the stochastic cooling above $1.5 \text{ GeV}/c$.

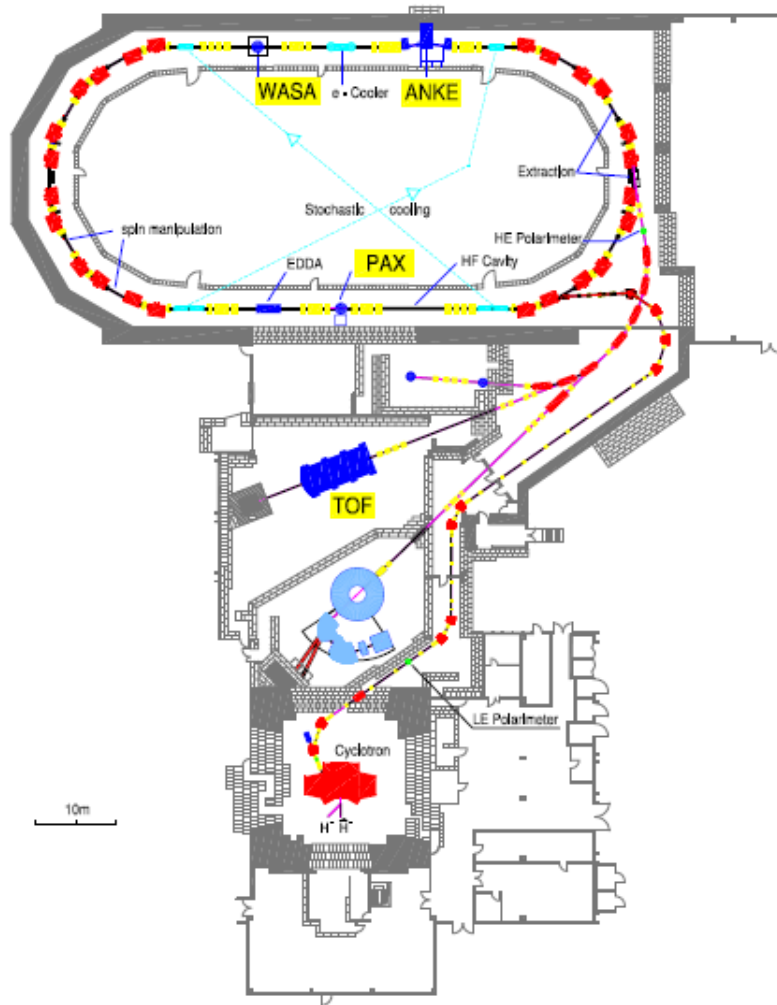


Figure 5.1: The floor plan of the COSY facility [38].

The accelerated beam has a typical momentum spread of $\Delta p/p \sim 10^{-4}$ and an emittance of 0.4π mm mrad [45, 46, 47]. Figure 5.1 shows the schematic plan of the COSY accelerator complex which consists of the injector cyclotron with a 100 m long transfer beam line to the ring, the cooler synchrotron with a circumference of 184 m, three extraction beam lines and different experimental areas. COSY prepares a beam for two different types of target stations: internal experiments with thin or thick targets in the beam line and external target experiments with slow extraction that has times between 20 s and 5 minutes [48, 49]. The current operating experiments at COSY are ANKE (Apparatus for studies of Nucleon and Kaon Ejectiles), EDDA (used as a polarimeter), PAX (Polarized Antiproton EX-

periment) and WASA-at-COSY (Wide Angle Shower Apparatus) as internal experiments, and COSY-TOF (Time Of Flight) as an external experiment [40, 42, 50].

5.2 COSY-TOF Physics Program

The COSY-TOF detector with excellent tracking capability, large acceptance and full azimuthal symmetry is ideal for strangeness physics studies. The main part of the physics program at the COSY-TOF experiment is the production of Λ and Σ hyperons in proton-proton collisions. The $pp \rightarrow pK^+\Lambda$ reaction is one of the main channels which is measured in the COSY-TOF experiment [40, 50, 51]. This reaction has been investigated at several beam momenta between 2.7 GeV/ c and 3.3 GeV/ c [52, 53, 54], covering the energy range from close to threshold up to the COSY limit for the external beam (3.3 GeV/ c). One of the main reasons to measure the associated strangeness production in the $pp \rightarrow pK^+\Lambda$ reaction is to determine the role of N^* resonances in the production mechanism. The coupling of the N^* resonances to the $K\Lambda$ channel is not completely known. In the case of a strong influence of N^* resonances the reaction is used to investigate the resonance parameters and to search for unknown resonances. The $S_{11}(1650)$, $P_{11}(1710)$ and $P_{13}(1720)$ resonances are clearly identified in the experimental studies of the unpolarized measurements of the $pp \rightarrow pK^+\Lambda$ reaction at the COSY-TOF experiment [54, 55]. Moreover, the $pp \rightarrow pK^0\Sigma^+$ reaction is studied to check whether N^* resonances also couple to the ΣK channel [55, 56]. Furthermore, the hyperon-nucleon (Λp) final state interaction is studied which allows to extract the spin dependent scattering length, i.e. the interaction strength in the $p\Lambda$ system.

5.3 COSY-TOF Detector

COSY-TOF is a non-magnetic spectrometer which is made of a cylindrical tank with 3 m length and 2.5 m diameter. All the components of the detector are placed in this tank. The tank is evacuated to $\leq 10^{-3}$ mbar and the material budget of the components is minimized in order to reduce the rate of secondary interactions and multiple scattering of the beam particles and reaction products to have a precise tracking [19, 56, 57]. A schematic plan of the COSY-TOF detector is shown in Figure 5.2.

The COSY-TOF detector setup covers the full azimuthal angle and polar angles from 2° to 60° and provides a full phase space coverage for most of the hyperon production reactions. The COSY-TOF detector is organized in

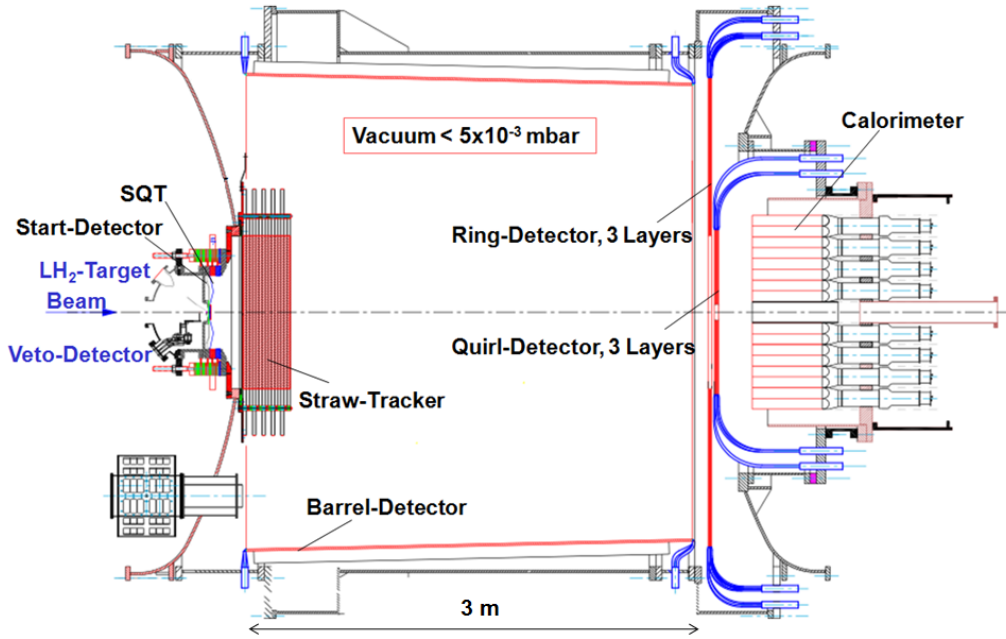


Figure 5.2: Schematic drawing of the COSY-TOF detector.

three main parts for particle detection including the start detector for time of flight (TOF) measurements, tracking part and the TOF stop detectors [56, 58, 59].

There is a target system installed in the entrance of the COSY-TOF tank in a section with vacuum of 10^{-6} - 10^{-7} mbar separated by a $20 \mu\text{m}$ thick Mylar foil from the vacuum inside the tank. The COSY-TOF uses liquid hydrogen or deuterium to achieve a high density target material. The high quality beam with a diameter of < 1 mm from COSY in addition to a target cell with 6 mm in diameter and 4 mm in length provides a small interaction region so that a good definition of the interaction vertex is possible. A small target volume also reduces systematic errors due to multiple scattering and secondary interactions in the target [19, 60].

There is a veto system before the target to exclude reactions which take place outside the target. The veto system consists of three scintillators. The first and second scintillators are placed 1 m and 50 cm upstream of the target and have a hole with 8 mm and 5 mm diameter, respectively. The third scintillator is located 50 mm upstream of the target and has five holes with different diameters from 1.5 mm to 3.5 mm. Position of the last scintillator can be adjusted to choose a hole with the most appropriate diameter for the beam focussing [61].

5.3.1 Start Detector

The start detector is located ≈ 2 cm behind the target center and provides the start signal for the time of flight measurements and the triggering of charged particles of the primary reaction products. The start detector consists of two discs of plastic scintillator with an outer radius of 76 mm and 1 mm thickness which are divided into 12 wedge shaped sectors with 30° azimuthal angle coverage each. There is a hole of 2 mm diameter at the center of the discs to allow the beam to pass without interaction. The discs are rotated azimuthally by 15° against each other. A start signal is created if two signals from partially overlapping sectors of two discs are measured in coincidence [58, 62].

5.3.2 Stop Detectors

System of the stop detectors consists of a cylindrical barrel hodoscope and a circular end-cap. The end-cap is built up by the quirl and the ring hodoscope. All stop detectors are housed in the vacuum tank.

The barrel detector is a cylinder with 96 scintillator bars with a length of 2.85 m which are read out on both sides. If there is a coincidence between the signals from both ends of the scintillator modules, a stop signal is created. The time difference of the signals is used to determine the z-coordinate of a passed charged particle. Figure 5.3 shows a photo of the barrel detector of the COSY-TOF experiment.

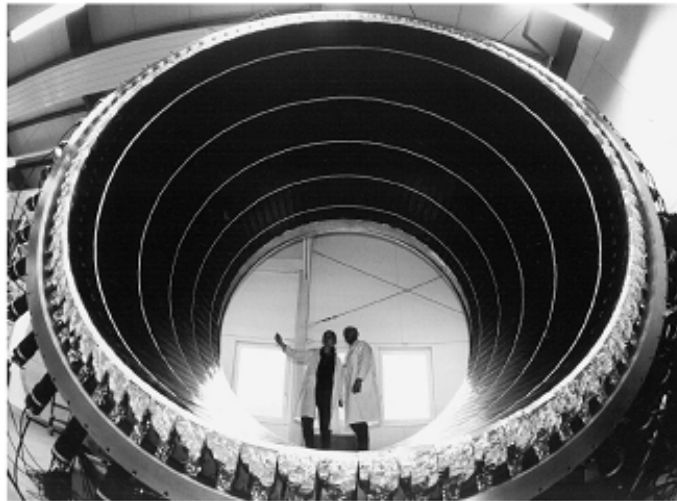


Figure 5.3: The cylindrical barrel detector. The inside white circles are the plastic bands to attach the scintillator bars to the support frames [63].

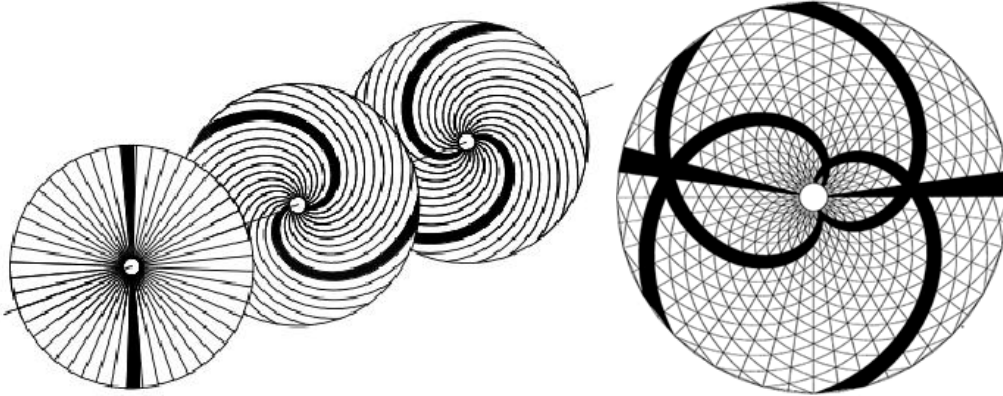


Figure 5.4: A schematic drawing of the three different layers of the quirl and ring hodoscopes [64].

Both the quirl and the ring hodoscopes consist of three layers of plastic scintillator read out by photo multiplier tubes mounted outside the vacuum tank. The structure of the three layers of scintillators is shown in Figure 5.4. Each hodoscope is structured in straight, left and right bended elements of scintillators. Each single scintillator element covers the full polar angle range of detector and is read out by photo multiplier with a light guide glued to it. The active part of all three layers has a thickness of 1.5 cm. The coincidence of two or three detector signals from different layers produces the stop signal for the time of flight measurement [64, 65]. The stop detectors have only been used for triggering in this work, because the time of flight information has not been recorded.

5.3.3 Tracking Detectors

There are two tracking detectors in the COSY-TOF spectrometer, the Silicon Quirl Tracker (SQT) and the Straw Tube Tracker (STT). They are used for both track and vertex reconstruction.

The SQT is the first tracking detector located ≈ 2.6 cm behind the target. It is a semiconductor silicon detector with a diameter of 70 mm and a thickness of $300\ \mu\text{m}$. There is a beam hole with 5.5 mm in diameter at the center of SQT layer to avoid beam interactions with the detector. The position sensitivity is provided by dividing each side of the detector into 256 Archimedean spiral shaped segments with counter-rotating spirals on the front and the backside [66]. For the readout 16 preamplifier boxes are arranged on a mounting frame of the vacuum tank [12, 56]. The SQT structure is shown in Figure 5.5.

The straw tube tracker as the main tracker in the COSY-TOF detector

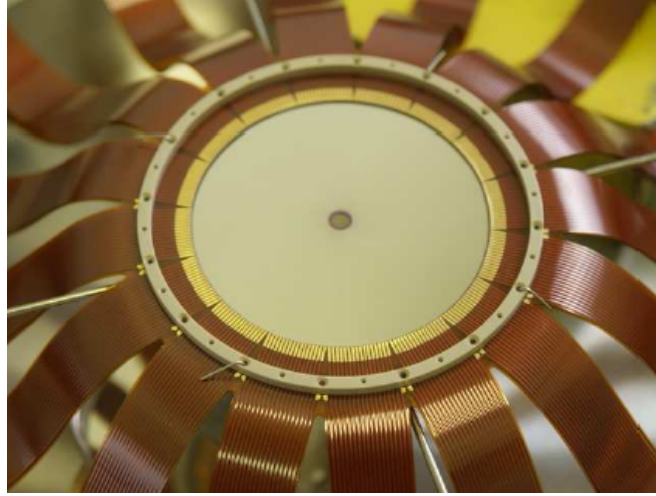


Figure 5.5: Photo of the SQT wafer and readout cables [56].

is described in more detail in the next section.

5.3.4 COSY-TOF Straw Tube Tracker

The STT is the second and the main tracking detector which gives the most precise information for the track direction and the position of the vertices. The STT is placed about 30 cm behind the target in the vacuum tank. It consists of 2704 straw tubes in 26 layers which are arranged in 13 double layers and fixed in three orientations with an angle of 60° to each other to enable 3D track reconstruction. Figure 5.6 shows the straw double layers mounted inside the COSY-TOF vacuum tank. A single straw has a length of 1050 mm, 10 mm diameter and $30 \mu\text{m}$ wall thickness. Apart from the length, the COSY-TOF straw tubes are the same as the straws which are used for the PANDA STT. The active detector volume of the 13 double layers is about 1 m in diameter and 30 cm in depth. An inner beam hole in each double layer with 15 mm diameter avoids beam interactions with the detector. Each straw tube is made of aluminized Mylar film and filled with $\text{Ar} + \text{CO}_2$ (80 : 20) gas mixture at 1.2 bar pressure. The straws are self-supporting to provide sufficient mechanical stability despite the low material budget of $X/X_0 \approx 1\%$ for 26 layers of straws. The anode is a $20 \mu\text{m}$ thick gold plated tungsten wire which is stretched along the straw axis and held at a potential of +1820 V. Thus, the wall of the straw tube acts as the cathode [12, 68]. More details of the straw tube structure are given in Section 1.4.

The COSY-TOF STT front-end electronics consists of a preamplifier and the ASD-8 chip containing amplifier, two stage shaper and discriminator.

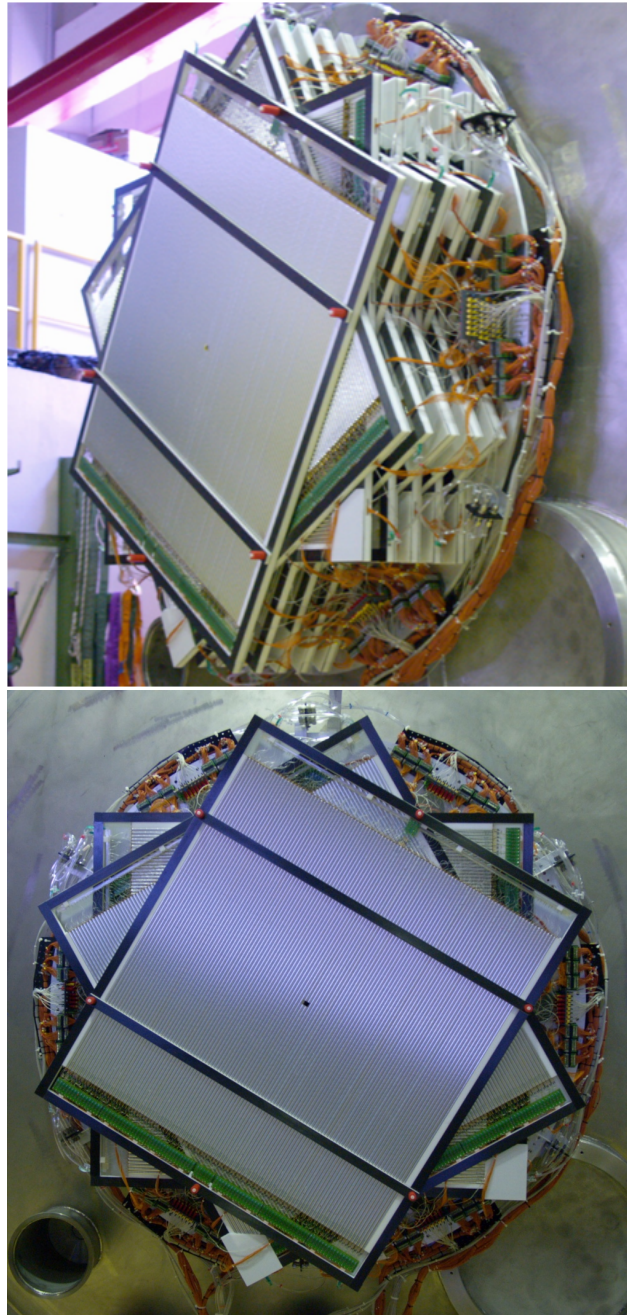


Figure 5.6: Photo of the COSY-TOF straw tube tracker with its double layer structure from side view (top) and front view (bottom). The general arrangement of the double layers in three rotational orientations for 3D tracking is visible. The preamplifier boards and cables to transfer the straw signals to ASD-8 chips are also visible [67].

The preamplifier boards are much smaller than the 1 cm diameter of the straw tubes and mounted directly to the straw tubes inside the vacuum tank. The ASD-8 chips are placed outside of the vacuum tank in order to achieve sufficient cooling and to minimize the material budget inside the active area of the detector. A front-end board containing two ASD-8 chips is shown in Figure 5.7. The analog signal from the straw tube is transmitted to the ASD-8 chip via 5 m long thin coax cables. To avoid a worsening of the signal to noise ratio in the cables between the straw tubes and the ASD-8 chip, the signal of the straw tube is fed into a preamplifier. The signal amplitude from the preamplifier at the end of the 5 m cable is shaped using an input board in front of the amplifier and the discriminator chip. The ASD-8 chip has a short peaking time (≈ 10 ns) with good double pulse resolution (≈ 25 ns) and low threshold (≈ 2 fC). A two-stage shaper using the pole zero cancellation technique removes the signal tail [19]. The timing information of the signal is finally recorded in the TDC channels for the further analysis.



Figure 5.7: (Left) Front-end board with two ASD-8 chips. (Right) the input board to match the amplitude of the signals from the preamplifier and shape them for the ASD-8 chip [19].

Chapter 6

Calibration of the COSY-TOF Straw Tube Tracker

The Straw Tube Tracker (STT) is the main detector for reconstruction of charged particle tracks in the COSY-TOF detector. In order to do a precise track reconstruction, the STT has to be carefully calibrated. This chapter explains the calibration steps of the COSY-TOF STT.

6.1 TDC Time Correction

In the first step of the calibration, some corrections are applied to the raw TDC spectrum of each single straw including the first hit selection, signal width cut and electronics offset correction [69].

When a charged track passes through the straw tube, gas molecules in the tube are ionized. The drift time information of the ionization electrons is stored in TDC channels. The drift time is measured by using the trigger signal as the start time and the straw hit signal as the stop time. The TDC channel numbers are related to the time information expressed in nanoseconds by multiplying a factor of 0.09259 ns which is defined by the readout electronic system. The left plot in Figure 6.1 displays the typical TDC time spectrum of all straws in a double layer, while the number of hits per straw is shown in the right plot.

6.1.1 First Hit Selection

In each straw tube several ionization clusters are created along the track of a charged particle. Most of these clusters can be recorded by using fast shaping electronics. However, the main timing information is contained in the cluster which is closest to the wire and corresponds to the shortest drift

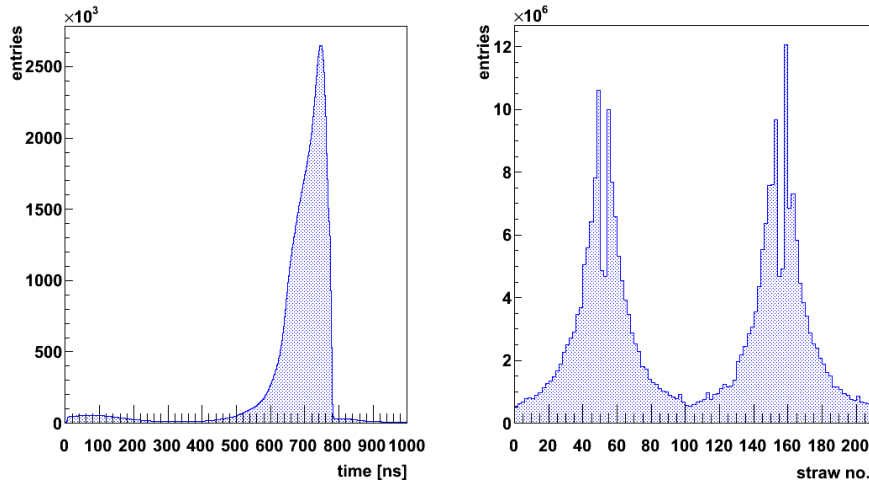


Figure 6.1: (Left) TDC time spectrum of all straws in double layer 9. (Right) number of hits per straw in a double layer. There are 208 straws in a double layer, therefore the numbers from 0 to 103 are related to the straws in the first layer and from 104 to 208 to the straws in the second layer. The first and the last straws in a layer receive less hits compared to the central straws which are located close to the beam hole. The reduction at the middle of each peak is a consequence of the shorter straws at the position of the beam hole.

time. In order to choose the first hit, the TDC times related to the leading and trailing edges of the signals are sorted and the first one is taken for the calibration. This correction to the raw TDC spectra makes it cleaner for further analysis, as shown in Figure 6.2.

The horizontal white lines in Figure 6.2 are related to empty spectra of single nonoperating straws. This problem originates from mechanical damage of the straws or a problem in their readout electronics. The distribution of inefficient straw tubes in all 13 double layers is shown in Figure 6.3. The Monte Carlo simulation in the ideal case is also shown for comparison.

6.1.2 Signal Width Cut

After selection of the first hit, the TDC spectra for single straws still show some noisy channels, for example the straws 768 and 793 in Figure 6.4 (left). In order to remove the remaining noise hits, the width between the leading and following trailing edge time is checked. The readout electronics needs at least 5 ns pulse width to record correctly the trailing edge time. Therefore, the noise events with small pulse height are recorded with a leading edge time without the following trailing time and with a signal width of 5 ns set by the TDC logic. Therefore, a threshold above 5 ns is selected for the width

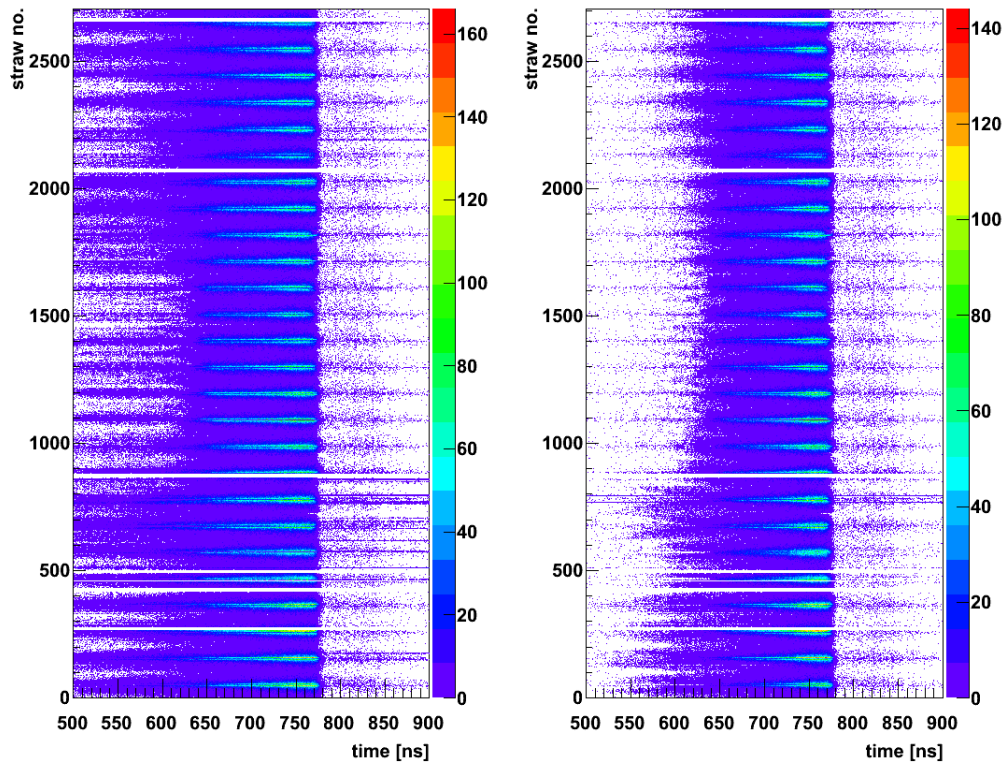


Figure 6.2: (Left) raw TDC spectra containing $5 \cdot 10^6$ hits in 2704 single straw tubes in 13 double layers. Using the common-stop mode in the readout of the TDCs, higher values correspond to shorter drift times. (Right) TDC spectra after removing multiple hits. The plot only shows the first leading times.

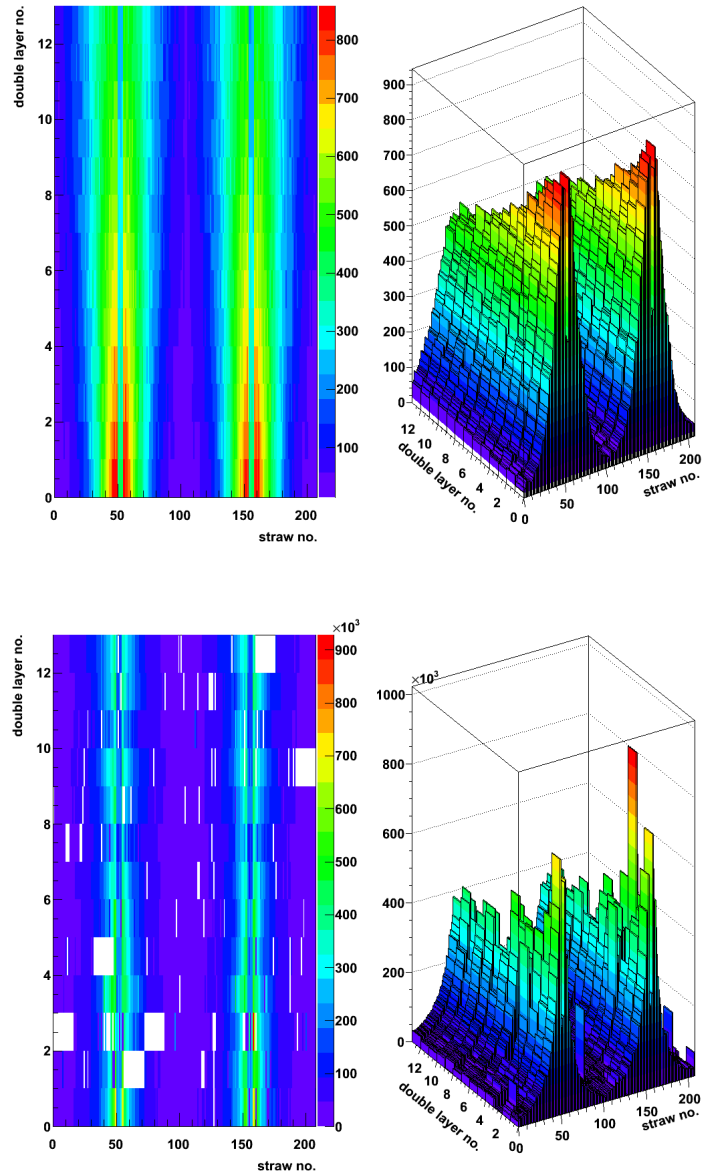


Figure 6.3: Hit distribution of straw tubes in different double layers in a 2D and 3D profile for Monte Carlo simulated events in the ideal case (top) and experimental data (bottom). The white areas in the 2D plot are related to inefficient elements. The 3D plot shows some noisy straws which are removed for the further analysis.

spectrum and only hits with larger widths than this limit are chosen. The effect of the width cut is shown in Figure 6.4 (right).

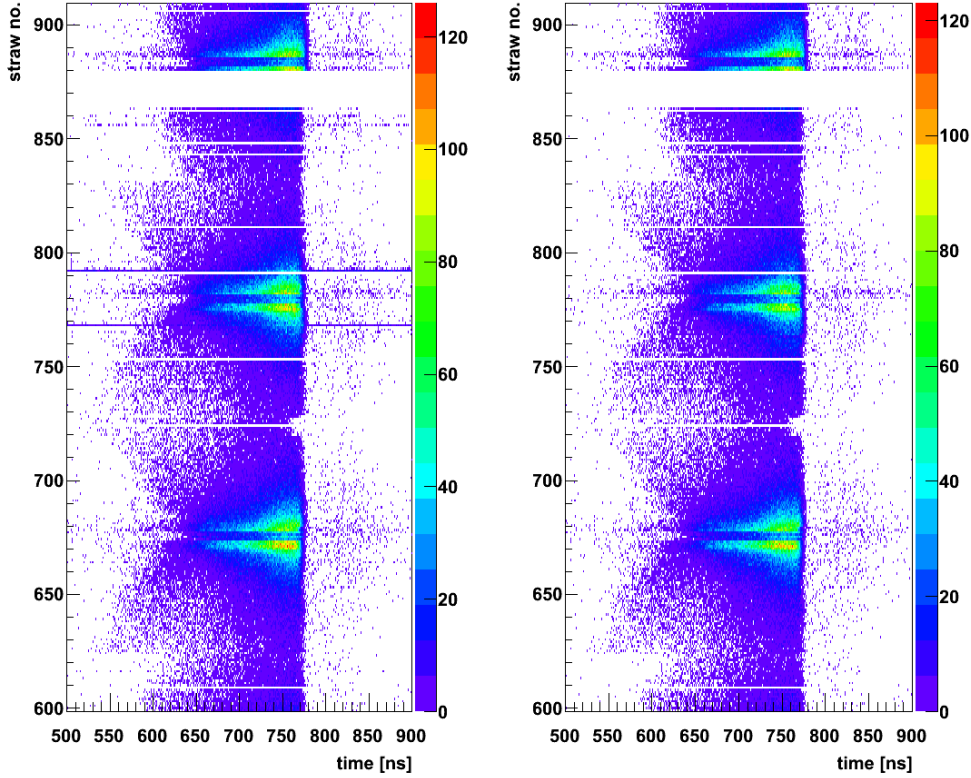


Figure 6.4: (Left) TDC spectra for 332 single straw tubes after removing multiple hits. (Right) TDC spectra for the straw tubes after applying the width cut. The noise visible in the channels 768 and 793, disappears after applying the cut.

6.1.3 Electronics Offset Correction

The TDC spectra are also corrected for the electronics time offsets. The irregular shape of the upper edge in the TDC spectra (see Figure 6.4) is largely due to an electronics offset related to different readout modules and time of flight effects in the double layers. In order to correct these effects a fit function is defined which describes the leading edge of the TDC spectrum of each single straw as shown in Figure 6.5. The fit function is defined as [70]

$$f(t) = \frac{a}{2} \left(1 - \operatorname{Erf} \left(\frac{t - t_p}{\sqrt{2}\sigma} \right) \right) + n, \quad (6.1)$$

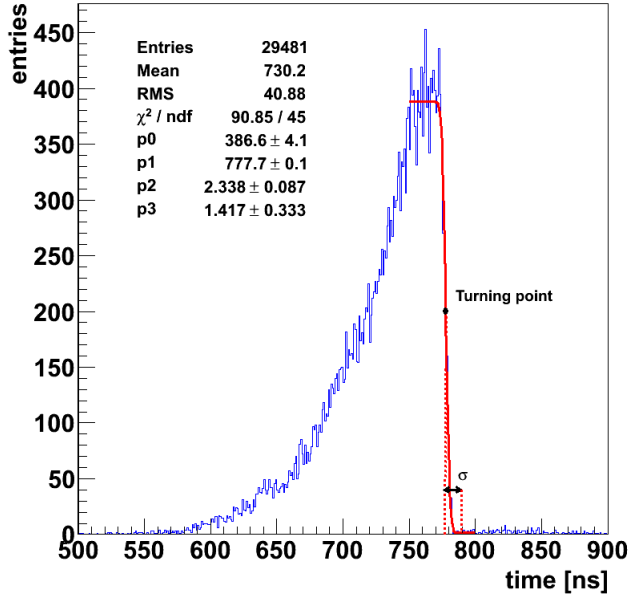


Figure 6.5: A complementary error function fitted to the leading edge of the TDC spectrum of a single straw to define the offset correction value for each single straw. For the straws with a small number of entries, the offset is determined by a linear interpolation between the neighbouring straws.

where a is the amplitude, t_p is the turning point, σ is the width of the slope, n is the background level and Erf is an error function. The complementary error function is given by

$$1 - \text{Erf}(x) = \frac{2}{\sqrt{\pi}} \int_x^{\infty} \exp(-t^2) dt. \quad (6.2)$$

Then a reference point is determined as the sum of the turning point of the fit function and one sigma (σ). This reference point is corrected to an arbitrary time (780 ns) for each single straw to remove the electronics offset. The irregular shape of the upper edge of the TDC spectra and offset corrected spectrum is presented in Figure 6.6.

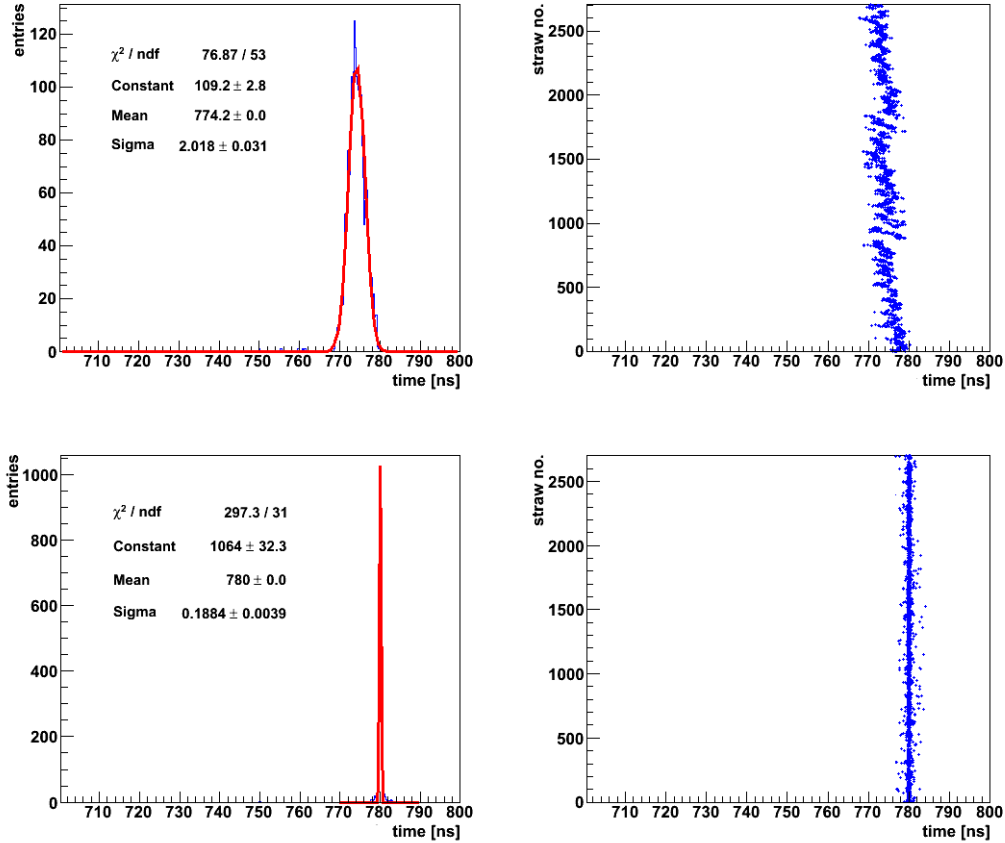


Figure 6.6: (Top right) position of upper edge of the TDC spectra for single straw. The irregular shape is predominantly a result of electronics offset from different boards of the readout system. The three different parts in the spectrum are due different delays connected with the presence of three electronic racks, the slope in each part is due to the positioning of the readout electronic boards in each rack, and the semilunar shape is related to time of flight effects resulting from the positioning of straw tubes in the double layers. (Top left) the distribution of the maximum TDC time before the correction of the electronics offset. The distribution is fit with a Gaussian function (red line) with a sigma of about 2 ns. (Bottom right) position of upper edge of TDC spectra after the correction for the straw electronics offsets. (Bottom left) distribution of the offset corrected maximum TDC time fit with a Gaussian function (red line) with a width of less than 0.2 ns, which demonstrates the effectiveness of the offset correction.

6.2 Calibration of Drift Time to Distance

The main goal of the calibration is the determination of the correlation between the drift time and the track distance to anode wire, because the hit position information is needed for the tracking in the further analysis. The drift time spectrum of a double layer of straws after applying the TDC corrections and subtraction from 785 ns (reference point $780 \text{ ns} + 2 \cdot \text{width of the slope}$) is shown in Figure 6.7. The drift time interval from 0 up to 145 ns corresponds to the TDC time interval from 785 ns down to 640 ns. The drift time of 145 ns corresponds to the straw radius $r = 0.5 \text{ cm}$. The spectrum in Figure 6.7 shows a tail part with drift times longer than 145 ns. This tail, which contains $\sim 1\%$ of the total number of entries is related to an improper recognition of the first hits and events pile up, and it is ignored in the calibration process in order to have clean hits.

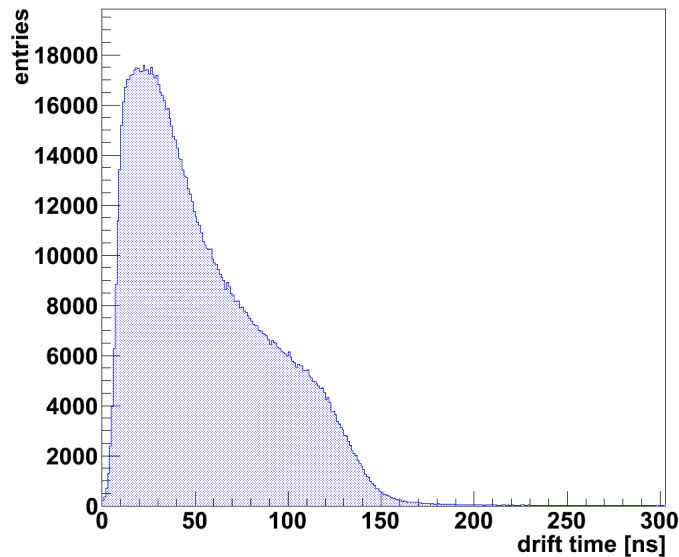


Figure 6.7: Drift time spectrum of all straw tubes of double layer 9.

6.2.1 “Self Calibration” Method

The hit position information in each straw tube is determined by a parameter called the isochrone radius. An isochrone radius defines a circle of the smallest distance of a particle track to the straw wire. A sketch of the isochrone circles associated to one track is shown in Figure 6.8.

To find the correlation between the drift time and the isochrone radius, the drift time distribution is divided into 145 bins of 1 ns width each, and

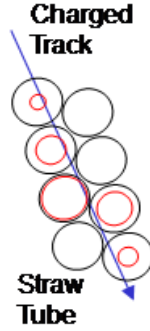


Figure 6.8: Schematic drawing of the isochrone circles (red circles) corresponding to a charged track passing through straws in a double layer.

the isochrone radius is calculated for each bin using the following formula [10]:

$$r(t_i) = \int_{t_0}^{t_i} v_{drift}(t) dt = (R_{tube} - R_{wire}) \frac{\sum_i N_i}{N_{tot}} + R_{min}, \quad (6.3)$$

where R_{tube} and R_{wire} are the straw tube radius (0.5 cm) and anode wire radius (10 μm), respectively. N_i is the number of hits between t_0 to t_i where t_0 correspond to the shortest drift time and $R_{min} = 20 \mu\text{m}$ is the minimum radius around the wire defined by the inefficiency of a straw tube in the avalanche region close to the straw wire. This method, which is called the “self calibration” method, assumes that there is a homogenous distribution of track hits along the straw radius and the detection efficiency is constant over the straw tube diameter [10, 56, 57, 69].

Ideally the $r(t)$ curve should be the same for all straw tubes. However, the analysis shows that there is a difference in the $r(t)$ curves of some double layers due to a lower sensitivity of their readout electronics. Therefore, the averaged $r(t)$ curves from 3 groups of double layers (1,2,3,4), (6,7,8,9,10) and (5,11,12,13) are used for all straw tubes in the corresponding group. The first estimation of the $r(t)$ curve for a group of straw double layers is shown in Figure 6.9.

6.2.2 “Autocalibration” Method

The first approximation of the $r(t)$ curve is used for the track reconstruction to find the most probable correlation between the drift time and the track to wire distance. This is done by an iterative procedure called the “autocalibration” method [10]. Tracks with at least 17 hits are reconstructed and fit by applying the $r(t)$ curve from the self calibration method. After that, the track to wire distances are calculated for all hits of the track. Figure 6.10

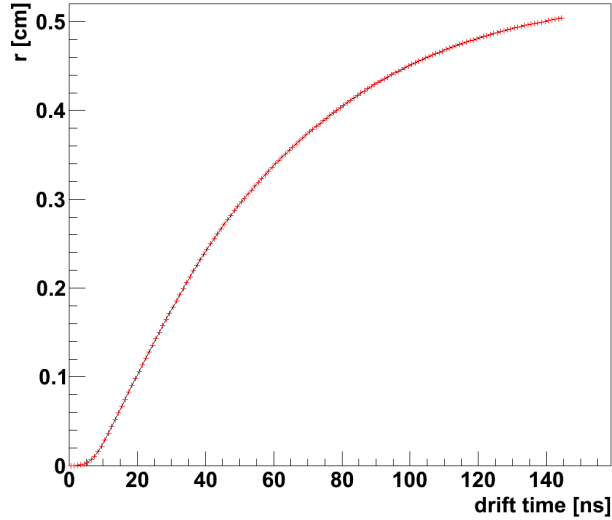


Figure 6.9: Isochrone radius as a function of drift time determined with the self calibration method for double layer 9.

(top) shows the distances of the track to the wire versus the measured drift times for the reconstructed tracks.

To find the most probable $r(t)$ curve, the drift time axis of the spectrum in Figure 6.10 top is divided into 145 bins, and the content of each bin is projected on the distance (y) axis. Figure 6.10 (bottom) shows such a projection for the bin with $t = 80$ ns. A Gaussian function is fitted to both arms of the projected spectrum and the averaged mean of both fit functions is taken as the probable r value for the corresponding drift time bin. The same procedure is applied for all drift time bins which eventually make a new $r(t)$ curve. In the autocalibration method the new $r(t)$ curve is again used in the same procedure in order to minimize the track residuals. The residual is defined as the difference of the track to wire distance from the fitted track and the isochrone radius predicted from the previous $r(t)$ curve. The procedure is terminated when the mean residual is distributed around zero at all radii of the straw tube with a precision of $30 \mu\text{m}$. The relation between the drift time and the most probable isochrone radius typically converges after 5 – 6 iterations and is shown in Figure 6.11.

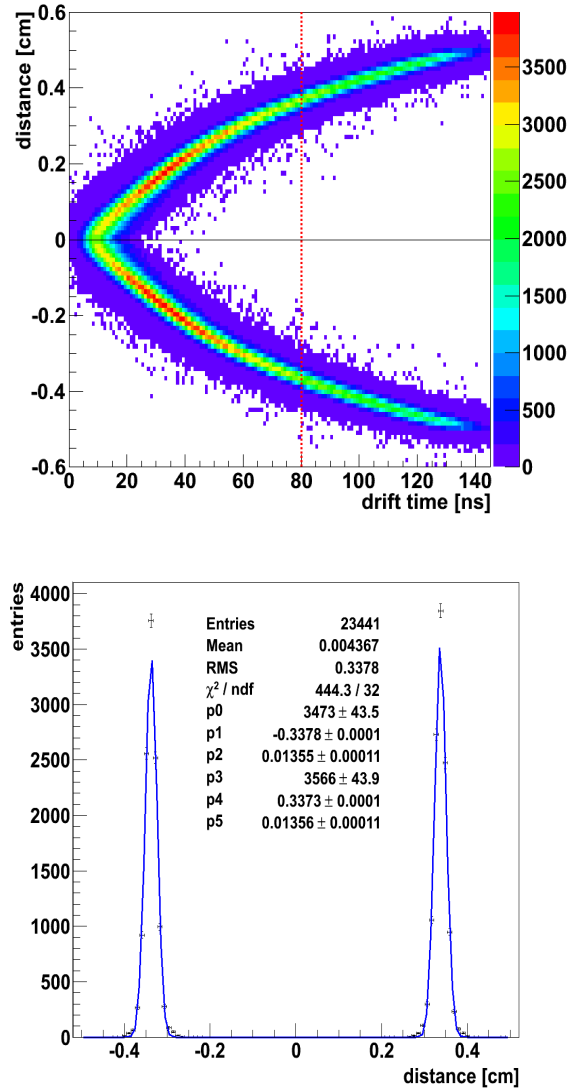


Figure 6.10: (Top) track to wire distance vs. the measured drift time for reconstructed tracks for double layer 9. The two arms of this figure are related to the right and left side of the straw wire. The distance distribution shows a symmetric behavior for the right and left side of the straw wire. (Bottom) distance (y-axis) projection of contents in the drift time bin indicated by the dashed red line in the top plot. The blue line shows the Gaussian functions fitted to the projection distribution for both left and right peaks.

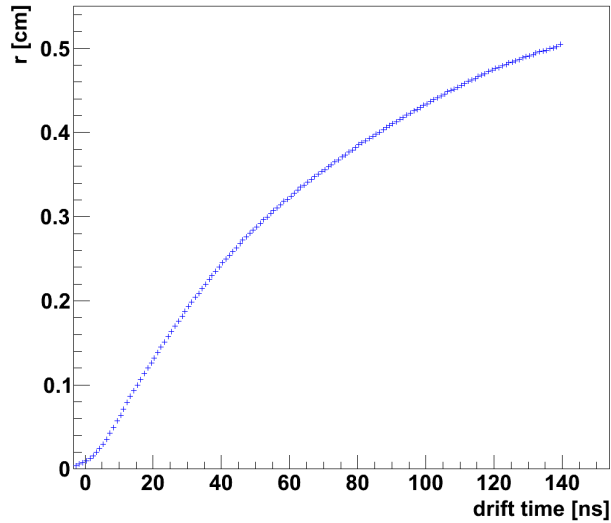


Figure 6.11: The most probable correlation between the drift time and the isochrone radius for double layer 9 after five iterations of the autocalibration process.

6.3 Mean Residual of the STT

The mean residual is zero at all radii for the most probable $r(t)$ curve. Figure 6.12 (top) shows the residual distribution as a function of the drift time for the reconstructed tracks. In order to determine the residual distribution precisely, the spectrum is divided into 145 bins in the drift time and the projection of each bin content onto the y-axis is fitted with a Gaussian function, as showed in Figure 6.12 (bottom). The mean and the width of the Gaussian fit function determines the mean residual and the resolution of the double layer in each drift time bin, respectively. By repeating this procedure for all drift time bins and using the most probable $r(t)$ curves from the last iteration, the residual and resolution distribution curves as a function of isochrone radius for each double layer are generated. The mean residual distribution for all double layers of straws is found close to zero, as shown in Figure 6.13 for double layer 9 after 5 iterations of the autocalibration method and applying the geometry calibration (see Section 6.4). The distribution of the width of the fitted Gaussian function is presented in Section 6.5.

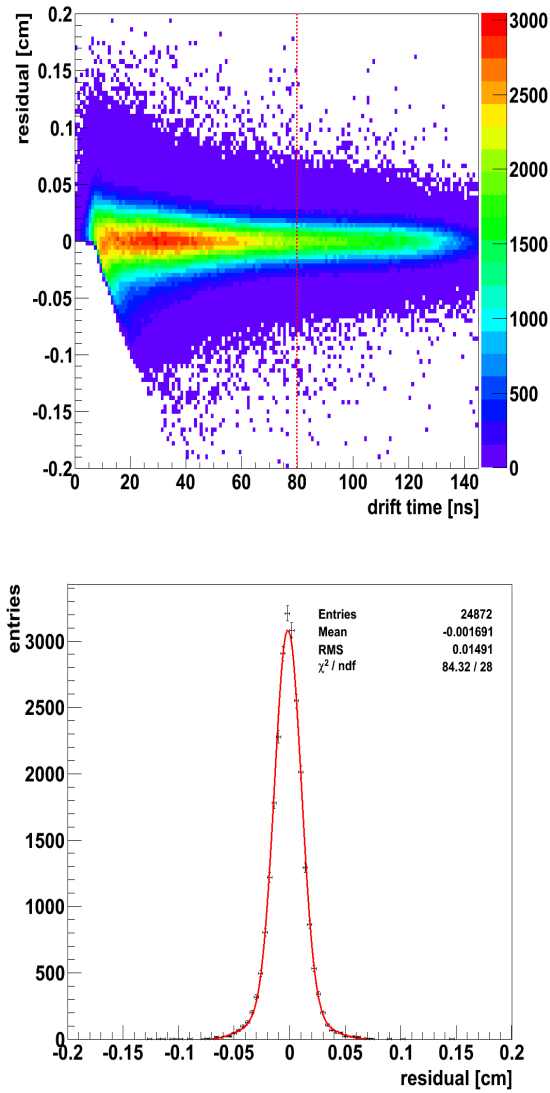


Figure 6.12: (Top) distribution of the residuals as a function of the measured drift time after five iterations of the autocalibration process for double layer 9. (Bottom) distribution of the projected residuals for a drift time bin indicated by the dashed red line in the top plot. The red line is a fit with a Gaussian function.

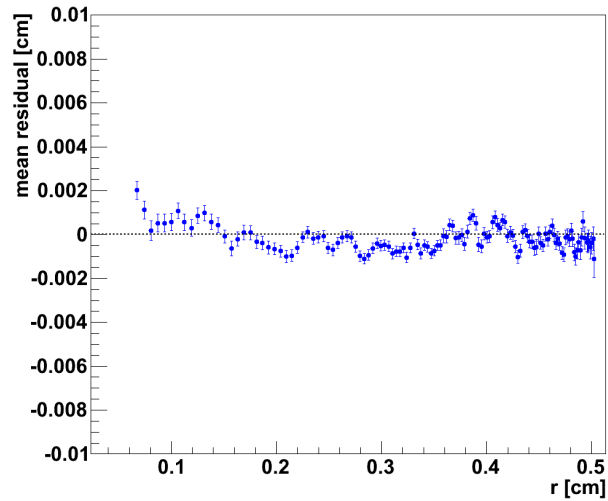


Figure 6.13: The mean residual as a function of isochrone radius after five iterations of the autocalibration process for double layer 9. The autocalibration process is terminated if the mean residuals for all double layers deviate less than $30\ \mu\text{m}$ from zero.

6.4 Calibration of the Straw Geometry

Precise determination of the track parameters depends on the accuracy in geometry of the straw double layers. The relative position of the straws in each double layer is known very well due to its structure in which 208 straw tubes are glued to each other and the self supporting property of the straws. Therefore, the main uncertainty is the position and rotation error of the double layers.

6.4.1 Calibration of the Double Layer Positions

In order to find the exact position of each double layer, the track reconstruction is done with an “unbiased” method. In this method, the double layer which is studied is not taken into account for the track reconstruction. Hence the track is fit with the information from other double layers. The track to wire distance information for the double layer under consideration is calculated for this fitted track, and this process is repeated for all double layers. This distance information is the most appropriate track parameter to study the shifts in the position of the double layer perpendicular to the wire and the beam direction. Any shift in the double layer positions can be seen in the track to wire distance at the right and left sides of the straw wire [71]. Hence, the closest tracks to wire distance for each double layer

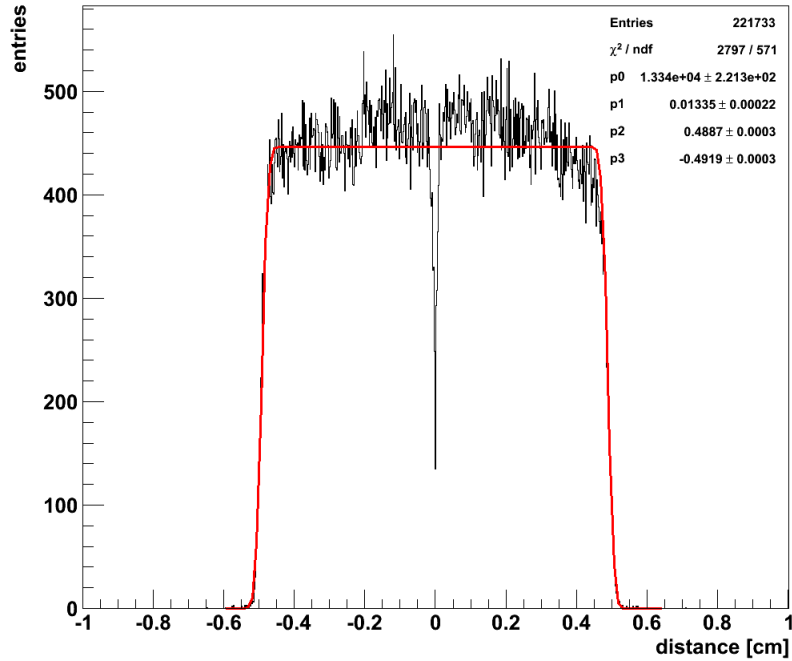


Figure 6.14: The distribution of the closest track to wire distance, fitted with the convolution of a box and Gaussian function (red line). The displacement of the straw double layer is seen as a deviation of the left and right edges from the straw radius (0.5 cm).

is plotted and a box function convoluted with a Gaussian function is fit to the distribution, as shown in Figure 6.14. The distribution in Figure 6.14 shows that there is a reduction in the number of entries at zero. This reduction is due to the minimum isochrone radius around the wire for which tracks cannot be recorded. When the tracks pass too close to the wire in the avalanche area, the ionization electrons do not have sufficient path length to produce secondary ionization pairs. This minimum is usually in the range of $10 - 20 \mu\text{m}$. The difference in the fit parameters of the left and right side of the distribution is used to calculate the shift of each straw double layer. In addition, the shift between the mean values of the Gaussian fit to the two arms in Figure 6.10 (top) is calculated for each bin of drift time or corresponding radius to find the direction of the position correction of each double layer. Any displacement in the shift plot from zero is clearly visible and its deviation from zero determines the sign of the position correction. Figure 6.15 (left) shows the shift plot for a double layer before applying the position correction. The shift distribution is above zero, so the correction value which is precisely determined from the distance distribution plot

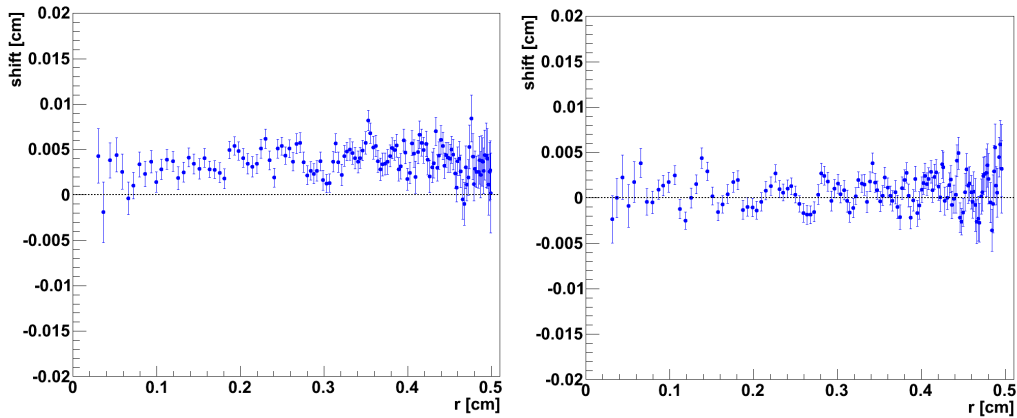


Figure 6.15: Difference in the track to wire distance for the right and left side of the wire for a double layer before (left) and after (right) the position correction. The corrected plot shows that the shift distribution is around zero for all radii.

should have a minus sign to bring the shift distribution to zero. The shift plot after applying the position correction on this double layer is shown in Figure 6.15 (right).

The straw position correction is an iterative process which takes the geometry information of the mechanical installation of STT at the beginning and starts with a correction of the double layer with the highest shift. In the iteration procedure the corrections are done until the shifts of all double layers are less than $50 \mu\text{m}$. By this method, the precision of positioning of the STT is two times improved compared to the previous calibration corrected up to $100 \mu\text{m}$ [57].

6.4.2 Calibration of the Double Layer Rotations

The rotation correction of each double layer is done in the same way by studying the residual distribution along the straw wire. Any misalignment in the double layer changes the mean residual distribution from zero. A sketch of a double layer rotation is shown in Figure 6.16. In order to correct the rotation of each double layer, a Gaussian function is fitted to the residual distribution of each straw length bin. The rotation correction angle is defined as

$$\theta = \arctan \frac{m}{l}, \quad (6.4)$$

where m is the mean residual from the Gaussian fit function and l is the length of the straw tube from the middle point of the straw double layer and determined from the center value of each bin. The rotation correction

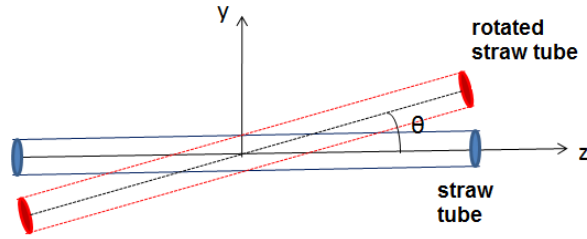


Figure 6.16: Schematic drawing of the rotation θ in a straw double layer. The straw marked as red has been rotated with θ respect to the correct direction marked in blue.

is an iterative process and continues until the angular correction of less than 0.2 mrad for each straw length bin is reached. Figure 6.17 shows the rotation angle of a double layer after correction. After this alignment of the double layers geometry, the resolution of the straws in the double layers can be determined.

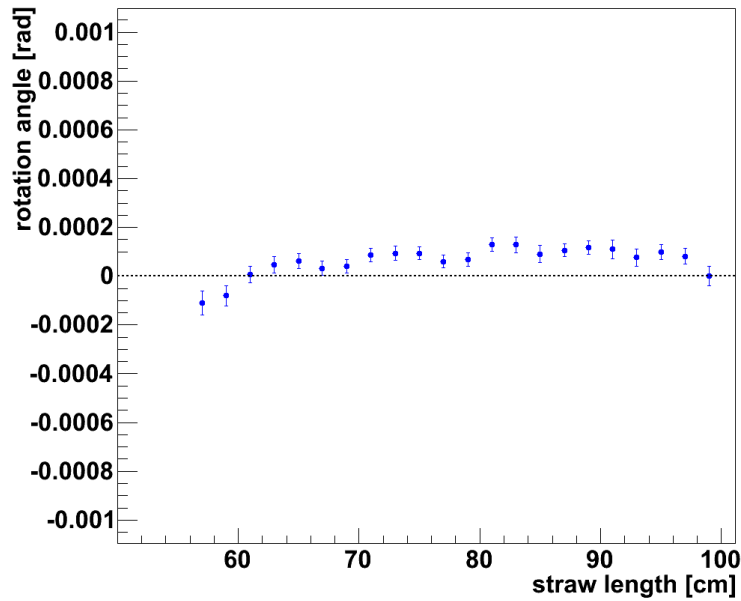


Figure 6.17: Rotation angle of a double layer as a function of the straw length from the center. Because the rotation angle is symmetric around the straw center, only half of its length is presented. The rotations are corrected up to 0.2 mrad.

6.5 Spatial Resolution of the STT

In addition to the $r(t)$ curve, which defines the most probable correlation between the drift time and the isochrone radius, the spatial resolution is another important parameter and must be determined for each double layer. The spatial resolution of the STT is the width (σ) of the Gaussian function fit to the reconstructed track residual distributions for each bin of the isochrone radius (see Figure 6.12). The resolution for the first double layer is shown in Figure 6.18.

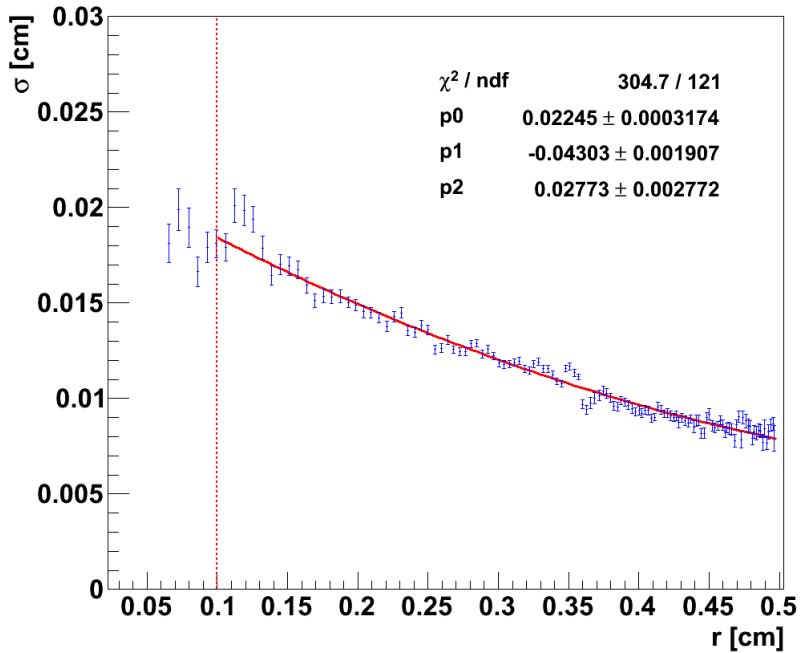


Figure 6.18: Resolution distribution as a function of the isochrone radius for double layer 1. The resolution distribution is fitted with a second order polynomial function (red line) from 0.1 cm to 0.5 cm.

The resolution is worse close to the wire than at the straw wall. This is due to the limited statistics of the primary ionization clusters (see section 2.1) and high drift velocity close to the wire. Both of these effects are reduced far from the straw wire [10, 72] and the resolution improves near to the straw tubes wall to $80 \mu\text{m}$. This value is limited by the diffusion of the electrons. The resolution distribution is fit with a second order polynomial function $\sigma(r) = p_0 + p_1 \cdot r + p_2 \cdot r^2$. The results of the fit to each double layer are collected in Appendix B, and they are used in the Monte Carlo simulation and further analysis of the experimental data. For comparison,

Table 6.1: Spatial resolution of the straw double layers at 0.25 cm.

Double layer	1	2	3	4	5	6	7	8	9	10	11	12	13
resolution [μm]	134	146	128	140	139	151	148	151	139	141	142	122	131

the resolutions at 0.25 cm radius for each double layer are summarized in Table 6.1.

The average spatial resolution over all double layers at a straw radius of 0.25 cm is $(139.4 \pm 8.8) \mu\text{m}$ with this calibration which is an improvement of about 20% compared to the average resolution of $(174 \pm 18) \mu\text{m}$ with the previous calibration at the same beam momentum [57]. The improvement is obtained due to the more precise calibration process in different steps.

Chapter 7

Analysis of pp Elastic Scattering and $\vec{p}p \rightarrow pK^+\Lambda$ with COSY-TOF STT Data

The $pp \rightarrow pK^+\Lambda$ reaction is well suited for studies of the strangeness production since the strange quark does not exist as constituent in the nucleon. To study the details of this reaction in the near-threshold region different models based on strange and non-strange meson exchange mechanisms have been developed [73, 74]. Moreover, different $pp \rightarrow pK^+\Lambda$ measurements have been done with polarized and unpolarized proton beams at different momenta from 2.7 to 3.3 GeV/ c with the COSY-TOF and other experiments [54, 75, 76].

The large acceptance of the COSY-TOF detector covers the full phase space of the $pK^+\Lambda$ reaction. Therefore, different physical effects involved in this reaction such as excitation of nucleon resonances (N^*), $N\Sigma$ - $p\Lambda$ coupled channel effects ($N\Sigma$ cusp) and the $p\Lambda$ Final State Interaction (FSI) close to threshold can be analyzed. Furthermore, the investigation of the associated strangeness production of $K^+\Lambda$ close to threshold results in a better insight into the dynamics of the $\bar{s}s$ production [54, 55, 57, 61]. The new measurement with the COSY-TOF detector presented here are done with high statistics and a polarized proton beam at 2.95 GeV/ c to study the $\vec{p}p \rightarrow pK^+\Lambda$ reaction mechanism. The large acceptance of the detector in addition to the outstanding tracking capability of the straw tube tracker allows a complete measurement of the $pK^+\Lambda$ final states and analysis of the Dalitz plot over the full phase space. The reconstruction of the pp and $pK^+\Lambda$ final states in this study is done only with the straw tube tracker since the momentum resolution of the reconstructed primary particles with the STT alone is better than that from the time of flight analysis [57].

7.1 pp Elastic Scattering Analysis

Before the analysis of the $pK^+\Lambda$ channel, the pp elastic scattering events are analyzed in order to determine the experimental conditions of the measurement such as the target position and its dimensions for $pK^+\Lambda$ events reconstruction, the beam direction for the calculation of the $pK^+\Lambda$ event kinematics, and determination of the beam polarization for the analyzing power determination.

7.1.1 pp Elastic Events Selection

In order to select the pp elastic events, the data taken with the elastic trigger are used. An elastic trigger condition is defined by a charged particle multiplicity of two in both the start and stop counters. The events are reconstructed with the tof++ reconstruction software [77] developed for the STT (see Ref.[57]). The reconstruction software is based on the C++ programming language and has a connection to the analysis framework ROOT [78]. The package MINUIT [79] is used for minimizing the χ^2 of the fits in the various steps in the reconstruction process. The tof++ software requires the geometrical information of the detector and a calibration file in order to reconstruct the events. The process is done only with the STT due to the higher resolution of the STT compared to other subdetectors. In the first step, finding the tracks is done from the isochrone radius information of the straw hits by the Hough Transformation method [80] described in more detail in Ref. [57, 61]. The tracks are combined to find the vertex as the point of closest approach of the tracks. The events are reconstructed using the vertex fit [57] and the event kinematics are calculated from the event geometry information (for more detail see Ref. [57, 61]). Due to momentum conservation, there is the relation $\vec{p}_{beam} = \vec{p}_1 + \vec{p}_2$ connecting the beam momentum \vec{p}_{beam} and the two scattered proton momenta $\vec{p}_{1,2}$. The transverse (p_t) and longitudinal (p_l) momenta of the scattered protons are calculated using the angle between the protons and the beam direction ($\theta_{1,2}$) as follow:

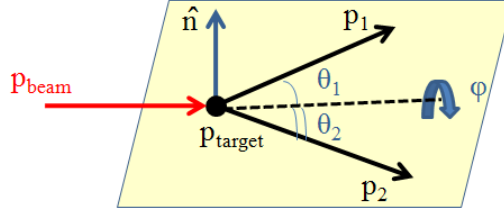
$$p_t = |\vec{p}_{beam}| \frac{\tan \theta_1 \tan \theta_2}{\tan \theta_1 + \tan \theta_2}, \quad (7.1)$$

$$p_{l_{1,2}} = \frac{p_t}{\tan \theta_{1,2}}. \quad (7.2)$$

The absolute momenta of the scattered protons are calculated by

$$|p_{1,2}| = \sqrt{p_t^2 + p_{l_{1,2}}^2}. \quad (7.3)$$

The pp elastic events selected with the elastic trigger include some background events. These background events are due to other reactions with

Figure 7.1: Geometry of the pp elastic scattering events.

two charged particles or incorrectly reconstructed events with two tracks in the final state. The main background in the pp elastic event sample includes $d\pi^+$, $pp\pi^0$, $pn\pi^+$ and $pp\pi^+\pi^-$ where the $\pi^+\pi^-$ are out of the acceptance of the detector. In order to select the true pp elastic scattering events and remove the background, in a first step a threshold is set on the reduced chi-square χ^2/ndf of the vertex fit (see Ref. [57]). Events with $\chi^2/\text{ndf} < 5$ are selected as candidates for the pp elastic scattering events for the further analysis. In addition, the pp elastic events are required to satisfy the condition $|\text{coplanarity}| < 5 \text{ mrad}$. Based on the geometry of pp elastic events (Figure 7.1) and demand to satisfy momentum conservation, the scattered protons and the beam have to be in the same plane. Therefore, the angle

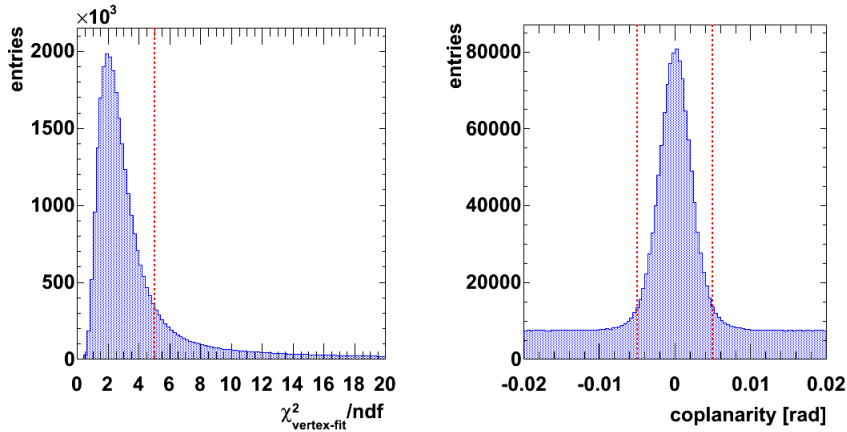


Figure 7.2: (Left) χ^2/ndf distribution of the vertex fit for possible pp elastic scattering events. The red dashed line indicates the maximum allowed value of 5 applied as an selection criterium for events. (Right) coplanarity distribution of pp elastic scattering events. The selection criterion of $\pm 5 \text{ mrad}$ is shown by the red dashed lines.

between the normal vector of the scattered protons plane and the beam must be around 90° . This geometrical parameter is called coplanarity angle and

it is given by

$$\text{coplanarity} = \arccos \left| \left(\frac{\vec{p}_1 \times \vec{p}_2}{|\vec{p}_1||\vec{p}_2|} \right) \cdot \frac{\vec{p}_{beam}}{|p_{beam}|} \right|. \quad (7.4)$$

For simplicity the coplanarity angle is subtracted from 90° to have a distribution around zero. The χ^2/ndf distribution of the vertex fit and the coplanarity distribution are shown in Figure 7.2.

The kinematics of the pp elastic scattering events results in an ellipse in the distribution of transverse versus longitudinal momenta of the scattered protons. The transverse versus longitudinal momentum distribution of the selected pp elastic events after the selection on the χ^2/ndf of the vertex fit and the coplanarity is shown in Figure 7.3.

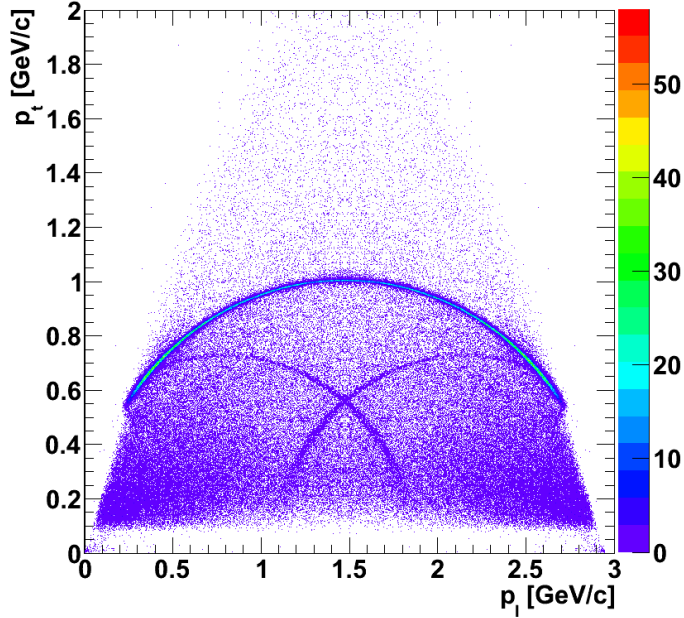


Figure 7.3: Transverse versus longitudinal momentum distribution of the pp elastic events after applying the constraint on χ^2/ndf of the vertex fit and the coplanarity. The top intensive ellipse is related to the pp elastic events and the two other elliptic bands are related to $d\pi^+$ events. Other background events are seen as the scattered points in the distribution.

Figure 7.3 shows that there are still some background events included in the pp elastic scattering event sample after applying the two selection criteria. If one proton scatters in forward direction with polar angle below 26° , the second scattered proton with higher polar angle cannot be triggered.

Using the momentum and the mass of the scattered protons, the four-vector (\mathbb{P}) of the particles are calculated and the sum of the four-vectors in

the entrance and exit channel have to be equal $\mathbb{P}_{beam} + \mathbb{P}_{target} = \mathbb{P}_{p_1} + \mathbb{P}_{p_2}$. The missing four-vector is defined as $\mathbb{P}_{miss} = (\mathbb{P}_{beam} + \mathbb{P}_{target}) - \mathbb{P}_{p_1} - \mathbb{P}_{p_2}$. Due to the kinematics of the pp elastic scattering events, the energy component of \mathbb{P}_{miss} which is called the missing energy should be around zero. Therefore, the missing energy is taken into account as the last selection criterion and a limit of $< \pm 10$ MeV is applied to the pp elastic scattering event sample. The missing energy distribution of the pp elastic scattering events is shown in Figure 7.4.

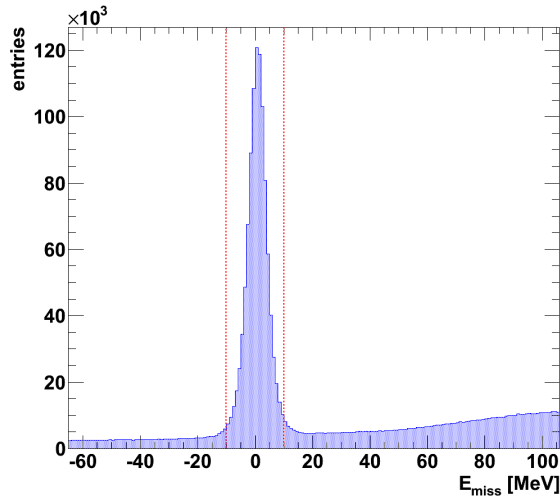


Figure 7.4: Missing energy distribution of the pp elastic scattering events selected by the χ^2/ndf and coplanarity constraints. The dashed red line indicates the selection.

The transverse versus longitudinal momentum of the pp elastic scattering events is plotted in Figure 7.5 after applying all three selection criteria on χ^2/ndf of the vertex fit, coplanarity and missing energy. A clean sample of pp elastic scattering events is observed.

7.1.2 Beam Direction Measurement

The calculation of the pp elastic scattering as well as the $pK^+\Lambda$ kinematics requires a precise knowledge of the beam direction. Because the STT is the main detector to determine the track information, the beam direction is determined relative to the STT geometry. Based on the pp elastic scattering geometry, the beam direction is perpendicular to the normal vector of the scattered protons. Therefore, any deviation of the coplanarity distribution from zero as a function of the azimuthal angle ϕ is related to a non-parallel direction of the beam to the z-axis of the STT and must be corrected. In

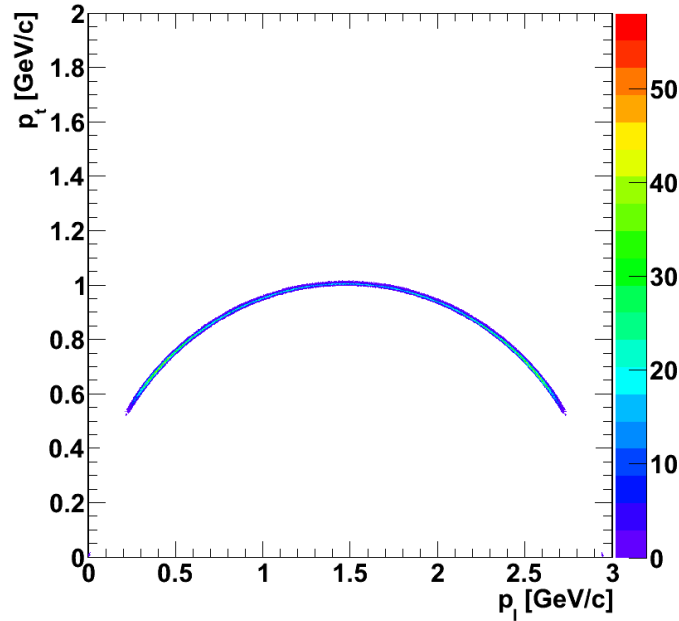


Figure 7.5: The transverse vs. longitudinal momentum of the selected pp elastic events after applying all three selection criteria.

order to determine the beam direction, a function of the azimuthal angle (ϕ) is fit to the profile of the coplanarity distribution as

$$f(\phi) = -\theta_{fit} \cdot \cos(\phi - \phi_{fit}). \quad (7.5)$$

The fit parameters $\theta_{fit} = -3.21 \pm 0.05$ mrad and $\phi_{fit} = -0.75 \pm 0.01$ rad are used to determine the (x, y, z) components of the beam momentum for the further analysis. Figure 7.6 shows the coplanarity distribution of the selected pp elastic scattering events as a function of the azimuthal angle ϕ before and after the correction.

7.1.3 Vertex and Target Measurement

Distribution of vertex in the pp elastic scattering events is used to determine the beam-target overlap region. The spatial distribution of the pp elastic scattering event vertex in the x-y and z-x planes is shown in Figure 7.7. Figure 7.7 (right) shows that the vertex distribution along the z-axis has a plateau which is related to the length of the liquid hydrogen target. Projections of the vertex distribution of pp elastic scattering events along the x and y axes are shown in Figure 7.8. The vertex projections are fit with Gaussian functions. The fit parameters show that the beam spot has a width of (805 ± 2) μm and (552 ± 1) μm along the x and y-axis, respectively.

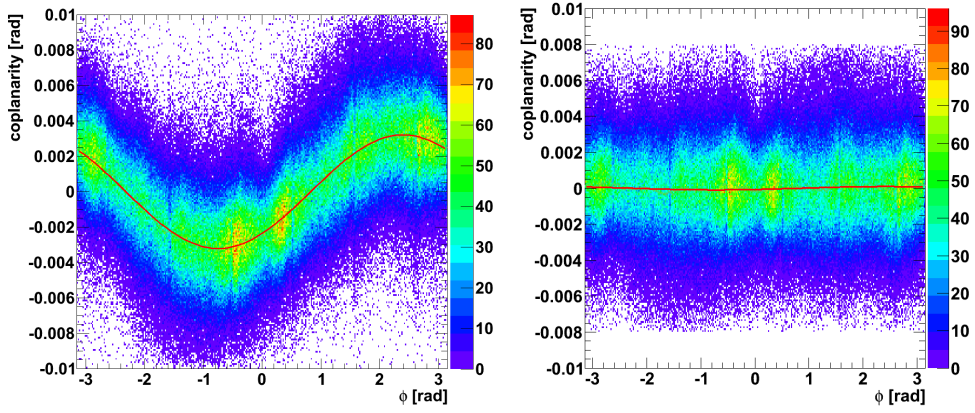


Figure 7.6: The coplanarity distribution versus azimuthal angle ϕ ; (left) before correction, (right) after correction. The red lines show the function fitted to the distributions.

The width of the Gaussian fit function of the x-projection is larger than the projection along the y-axis due to the stochastic extraction of the beam into the external beam line of the accelerator in this direction and different focus of the beam at the target.

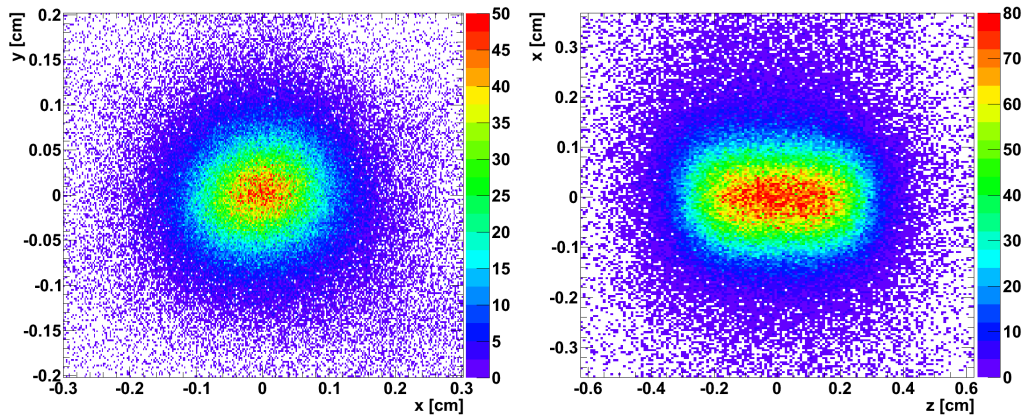


Figure 7.7: The vertex distribution of pp elastic events in the x-y plane (left) and z-x plane (right).

The projection of the vertex position distribution along the z-axis is shown in Figure 7.9 and it is fit with a box function convoluted with a Gaussian function. The box function determines the target length to be (5.16 ± 0.008) mm. This result is about 1 mm longer than the nominal length of the target, due to bending of the target foils. The Gaussian function has

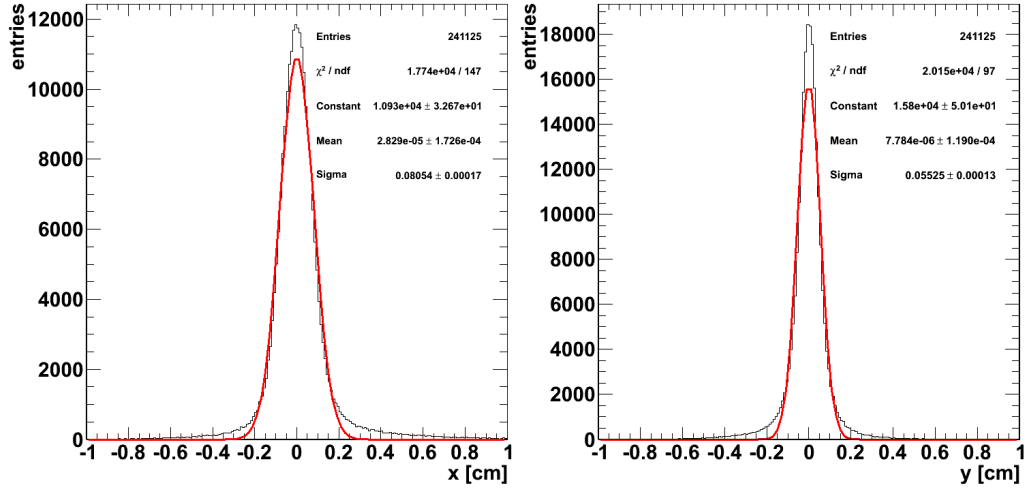


Figure 7.8: Projection of vertex distribution of the pp elastic scattering events onto the x-axis (left) and the y-axis (right) fitted with Gaussian functions (solid red lines).

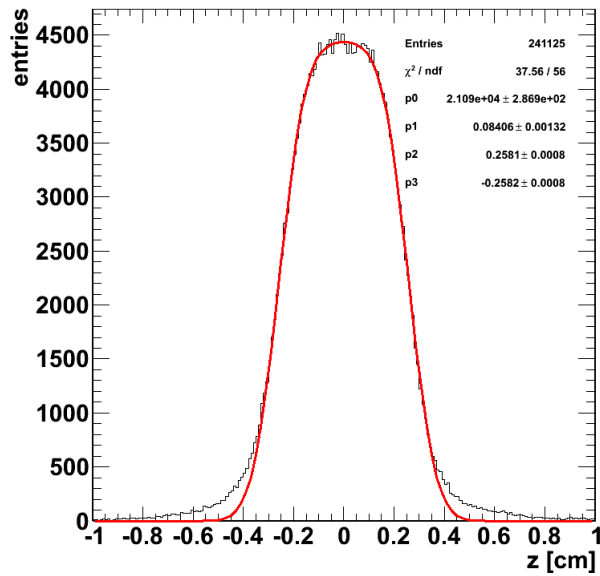


Figure 7.9: The distribution of the pp elastic events vertex projection along the z-axis fitted with a box function convoluted with a Gaussian function (solid red line).

a width of $(840 \pm 13) \mu\text{m}$.

Since the primary vertex distribution is affected by the beam properties and the extension of the target, it is not a suitable parameter to study the reconstruction accuracy of the pp elastic scattering events. In contrast, the minimum distance of the two scattered proton tracks is related to the STT reconstruction precision and it is independent of the beam properties. Therefore, the minimum distance of the two protons is an appropriate parameter to determine the reconstruction accuracy. The distribution of the minimum distance between two scattered protons is shown in Figure 7.10. The FWHM of this distribution is $2040 \mu\text{m}$, which corresponds to $\sigma \approx 860 \mu\text{m}$.

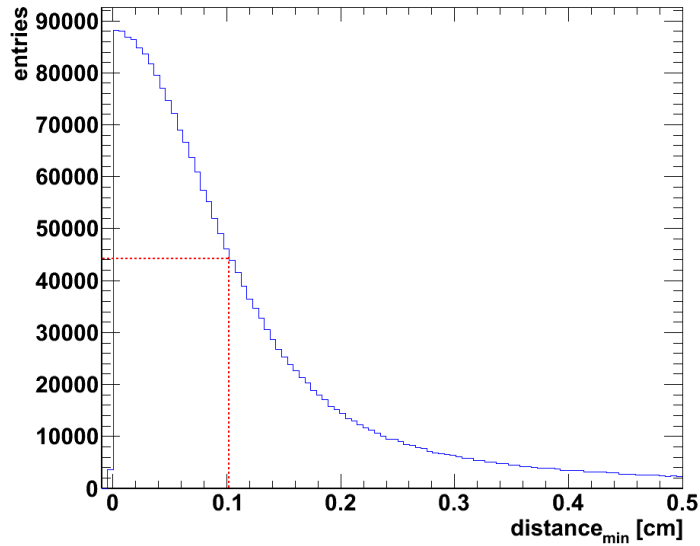


Figure 7.10: The minimum distance distribution between the two reconstructed tracks of the elastic scattering events. This distribution is related to the STT reconstruction precision. The red dotted line indicates the half of the FWHM which corresponds to $\sigma \approx 860 \mu\text{m}$.

7.1.4 Beam Polarization

In order to analyze the polarization observables for the $pK^+\Lambda$ events, the beam polarization is required. The beam polarization is determined from the left-right asymmetry of the scattered protons of the pp elastic scattering events and it is given by [81]

$$P_b = \frac{asy(\theta^{CMS}, \phi)}{A_N(\theta^{CMS}) \cos(\phi)}, \quad (7.6)$$

where $A_N(\theta^{CMS})$ is the analyzing power which is known from the SAID database [82], and $asy(\theta^{CMS}, \phi)$ is the asymmetry calculated by

$$asy(\theta^{CMS}, \phi) = \frac{L(\theta^{CMS}, \phi) - R(\theta^{CMS}, \phi)}{L(\theta^{CMS}, \phi) + R(\theta^{CMS}, \phi)} \quad \phi \in \left(-\frac{\pi}{2}, \frac{\pi}{2}\right), \quad (7.7)$$

$$\begin{aligned} L(\theta^{CMS}, \phi) &= \sqrt{N^+(\theta^{CMS}, \phi)N^-(\theta^{CMS}, \phi + \pi)}, \quad \text{and} \\ R(\theta^{CMS}, \phi) &= \sqrt{N^-(\theta^{CMS}, \phi)N^+(\theta^{CMS}, \phi + \pi)}, \end{aligned} \quad (7.8)$$

where N^+ and N^- are the numbers of events with spin up (+) and down (-) of the beam protons in the Center of Mass System (CMS). The left and right definitions include the number of events at opposite detector sides with

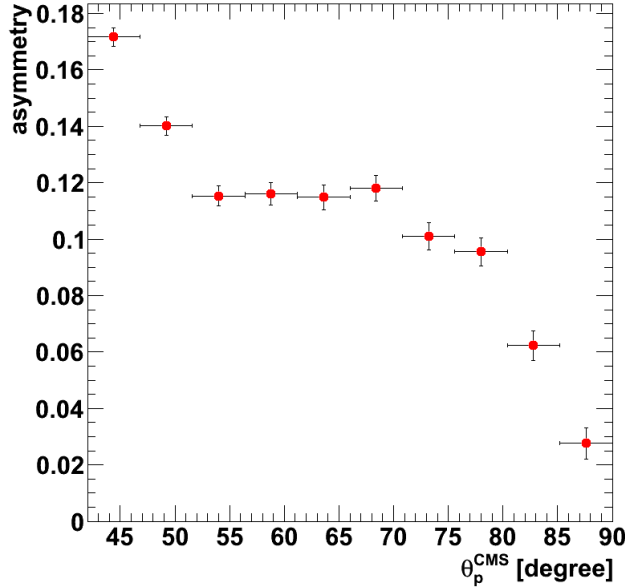


Figure 7.11: Asymmetry distribution of the pp elastic events for the proton scattering angle in the CMS.

different spin state to remove any asymmetry in the azimuthal acceptance of the STT detector in the first order [56, 57].

To determine the mean polarization of the beam, the scattering angle in the CMS in the range of $[40^\circ, 90^\circ]$ is divided into 10 bins and the azimuthal angle of the pp elastic scattering events is divided into 8 bins for each θ bin. Due to the acceptance loss of the STT at large polar angles the θ angular range chosen for this analysis is above 40° . Then the asymmetry for each ϕ and θ bin is calculated using Equation 7.7. Since the analyzing power for each θ bin is known from Ref. [82], the value $P \cdot A_N = asy(\theta^{CMS}, \phi) / \cos(\phi)$

is a constant for a given θ bin which is called the average asymmetry $ASY(\theta)$. Therefore, the asymmetry distribution is fit with the $ASY(\theta) \cdot \cos(\phi)$ function to determine the average asymmetry for each θ bin. Figure 7.11 shows the achieved average asymmetry $ASY(\theta)$ for all θ bins. The beam polarization is then determined for each θ bin using the average asymmetry and the known analyzing power. Averaging over all θ bins, a beam polarization of $(87.5 \pm 2.0)\%$ is obtained for this measurement. This beam polarization is rather high for the COSY accelerator for the present high proton beam momentum.

7.2 $\vec{p}p \rightarrow pK^+\Lambda$ Analysis

The $\vec{p}p \rightarrow pK^+\Lambda$ reaction is triggered by a charged particle multiplicity of two in the start counter and four in the stop counters. The reconstruction of $\vec{p}p \rightarrow pK^+\Lambda \rightarrow pK^+p\pi^-$ events is done in several steps (see Ref. [57, 61]). In the first step, the tracks are found and fit by the Hough transformation method. The tracks are then combined to find out the primary vertex and the Λ decay vertex. Subsequently, a geometrical fit is performed on the events, since the $pK^+\Lambda$ event can be uniquely determined by the event geometry in the absence of time of flight information. The event geometry for the $\vec{p}p \rightarrow pK^+\Lambda$ reaction is schematically shown in Figure 7.12. Therefore, the $pK^+\Lambda$ events should fulfill the geometry conditions so that the proton and pion from Λ decay combine to the same vertex called decay vertex. The tracks of the lambda and its decay products, i.e. proton and pion, have to be in the same plane. The kaon and primary proton combine in the same vertex called the primary vertex and the tracks of the kaon, primary proton and beam are in the same plane. The events are fit with MINUIT to minimize the sum of the χ^2 values of the four measured tracks.

The events that fulfill the geometry conditions are passed on to the last

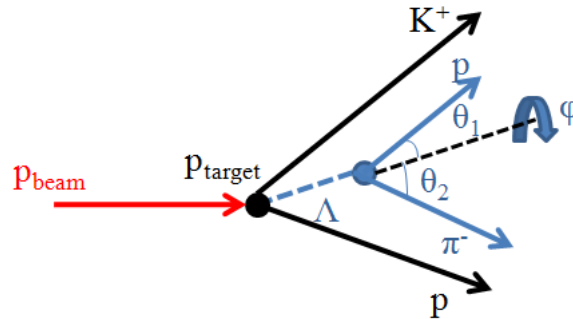


Figure 7.12: Sketch of the $pK^+\Lambda$ event geometry.

step of the event reconstruction process which is the kinematic fit. In total 20 parameters are necessary to describe events. These 20 parameters are the energy and momentum of the p , K , Λ and p and π from Λ decay. The direction (θ , ϕ) of measured particles p , K , and decay p and π and masses of all particles are used as input parameters, and hence the number of parameters reduces to 7. The masses of the decay particles can be assigned directly because the decay proton with its higher mass than the pion always has the lower angle relative to the Λ direction. For the primary particles the masses cannot be determined directly by geometry because the proton or kaon tracks are not clearly identified. Therefore, both masses are assumed in the kinematic fit and the selection with the lower χ^2 value is considered for the further analysis. The $pK^+\Lambda$ events are also constrained to satisfy both energy and momentum conservation in two vertices. Therefore, there is one over constrain to determine the parameters (for details see Chapter 4 in Ref. [57, 61]). Finally, the four-vectors of all particles are determined and different variables are calculated in both the CMS and the laboratory frame by applying Lorentz transformations.

7.2.1 $pK^+\Lambda$ Event Selection

The $pK^+\Lambda$ event selection is done by applying different selection criteria. First, a constraint on the reduced chi-square χ^2/ndf of the kinematic fit is applied and the $pK^+\Lambda$ events with $\chi^2/\text{ndf} < 5$ are chosen as candidates. With this selection one main background due to the $\bar{p}p \rightarrow pK^+\Sigma^0 \rightarrow pK^+\Lambda\gamma$ reaction, which has nearly the same event topology as the $pK^+\Lambda$ events, is strongly reduced. Moreover, the angle between the direction of the Λ hyperon and its decay proton is taken into account in order to select the $pK^+\Lambda$ events and reject background events.

Some of the background events with a fake delayed vertex make the angle between the Λ and the decay proton close to zero, which cannot be true for kinematical reasons. Therefore, only the $pK^+\Lambda$ events which satisfy the condition $\angle(\Lambda, p) > 2^\circ$ are selected. Figure 7.13 (left) shows the χ^2/ndf distribution of the kinematic fit of the data and the distribution of the angle between the Λ and decay proton for both data and Monte Carlo simulation (right).

Furthermore, another criterion on the z component of the Λ decay vertex is applied to reduce background events. The primary particles can produce background events by interacting with the detector material (hadronic interaction). However, most of these background events cannot satisfy the condition on the z component of Λ decay vertex. Because the Λ proper life time ($c\tau$) is 7.89 cm [83] it decays mainly after the SQT, therefore applying

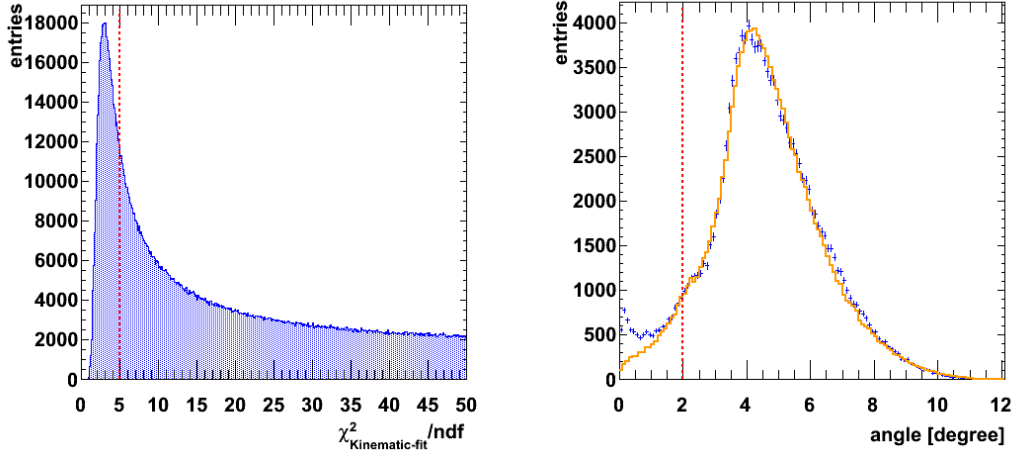


Figure 7.13: (Left) χ^2/ndf distribution of the kinematic fit for the measured $pK^+\Lambda$ event candidates. (Right) distribution of the angle between the direction of the Λ hyperon and its decay proton for the experimental data and MC reconstructed events (solid red line). The dashed lines show the applied thresholds.

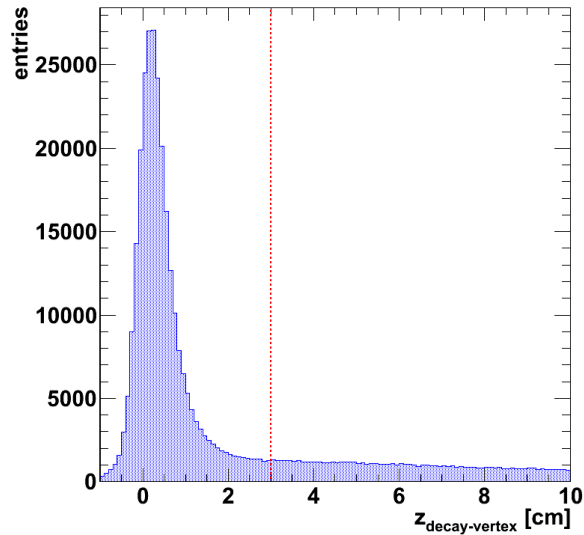


Figure 7.14: Distribution of the z component of the Λ decay vertex. The red dashed line shows the applied threshold constraint which is after the SQT position.

a constraint on the z component of the decay vertex rejects most of the background events. Figure 7.14 shows the distribution of the z component of the Λ decay vertex of the selected events.

The threshold is chosen so that events with $z < 3$ cm are rejected. The 3 cm threshold applied on the data is related to the position of the SQT detector which is located in front of the STT. After applying all three selection criteria a total number of about 130,000 $pK^+\Lambda$ events is obtained.

In order to evaluate the effectiveness of the applied selection criteria for choosing the true $pK^+\Lambda$ events with less background, the missing energy distribution of the selected events at the primary vertex is determined. The missing energy is calculated by $E_{miss} = (E_{beam} + E_{target}) - (E_p + E_K + E_\Lambda)$ before applying any selection criteria and after different steps as shown in Figure 7.15 for both measured data and Monte Carlo reconstructed events. As Figure 7.15 shows the missing energy is well distributed around zero after applying all three selection criteria. There is also very good agreement

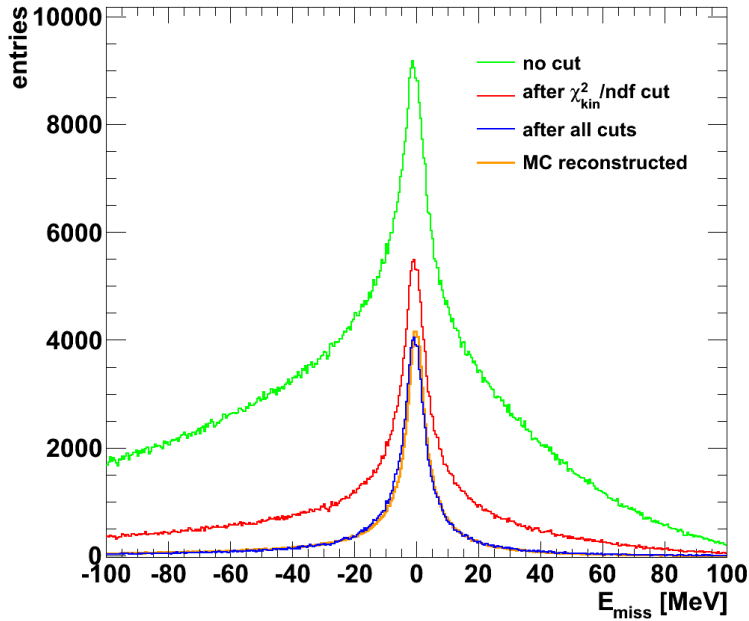


Figure 7.15: The missing energy distribution of the reconstructed $pK^+\Lambda$ events for the experimental data after applying different selection criteria. In addition, the distribution for reconstructed events from a Monte Carlo simulation is shown with the same selection criteria.

between the missing energy of the selected $pK^+\Lambda$ events of the data and the Monte Carlo simulation, which indicates an effective removal of background events. A conservative upper limit for the surviving fraction of the dominant

background channel $\vec{p}p \rightarrow pK^+\Sigma^0$ is given to be $< 5\%$ in Ref. [57, 84]. Therefore, the background is assumed to be negligible in the further analysis.

7.2.2 Reconstruction Efficiency and Precision

The reconstruction efficiency and precision of the $pK^+\Lambda$ events are determined after applying the geometrical and kinematical fit and using the selection criteria. The reconstruction precision is determined as the resolution of the different parameters involved in the $pK^+\Lambda$ event reconstruction process including primary and decay vertices, the momentum of the final state particles and the $p\Lambda$ invariant mass. For this aim, 10^6 $\vec{p}p \rightarrow pK^+\Lambda \rightarrow pK^+p\pi^-$ events are simulated with Monte Carlo. The Monte Carlo program generated $pK^+\Lambda$ events and tracked them based on the detector configuration including inefficiencies, and the physical processes involved in the detection of particles. The spatial resolution functions obtained for each straw double layer are used in the reconstruction process of the Monte Carlo simulated events.

7.2.2.1 $pK^+\Lambda$ Event Reconstruction Efficiency

After applying the same selection criteria to the reconstructed $pK^+\Lambda$ events of the Monte Carlo simulation, the ratio of reconstructed to generated $pK^+\Lambda$ events is defined as the reconstruction efficiency including the detector acceptance. In this study an overall reconstruction efficiency of $(32.0 \pm 0.06)\%$ is obtained. Because the Λ particle decays to $p\pi^-$ with a branching ratio of 63.8%, the obtained reconstruction efficiency has to be corrected with this corresponding ratio, in order to achieve the correct efficiency for the measured data. Thus, the reconstruction efficiency for the $pK^+\Lambda$ events is $(20.4 \pm 0.05\%)$. The result shows that the reconstruction efficiency is improved by about 20% compared to the former measurement at the same beam momentum. The improvement is achieved by applying the new calibration and optimizing the Hough space binning in the track finding process.

Furthermore, the integrated luminosity of this measurement is calculated as

$$L = \frac{N_{reco.}}{\sigma \cdot Ac \cdot Eff} \quad (7.9)$$

where $N_{reco.}$ is the number of reconstructed $pK^+\Lambda$ events, σ is the total cross section of the reaction at 2.95 GeV/ c beam momentum which was determined from other experiments [54] to be $(23.9 \pm 2.8) \mu\text{b}$, and $Ac \cdot Eff$ is the detector acceptance and efficiency. Using this information, an integrated luminosity of $(27 \pm 3) \text{nb}^{-1}$ is obtained for this measurement.

7.2.2.2 Vertex Resolution

The vertex resolution along all three axes (x , y , z) is determined as the difference between the vertex positions of the reconstructed MC events and the MC generated events $v(x, y, z) = v_{\text{mcreco.}} - v_{\text{mc.}}$. Figure 7.16 shows the distributions of the vertices for the $pK^+\Lambda$ events. The distributions are fit with a Gaussian function to determine the resolution of the vertex reconstruction. The sigma value of the fit indicates the resolution of the primary and decay vertex which are collected in Table 7.1. The resolutions of the decay vertex along the x and y axis are comparable with the primary vertex. However, the resolution along the z axis is less precise for the decay vertex than that for the primary vertex.

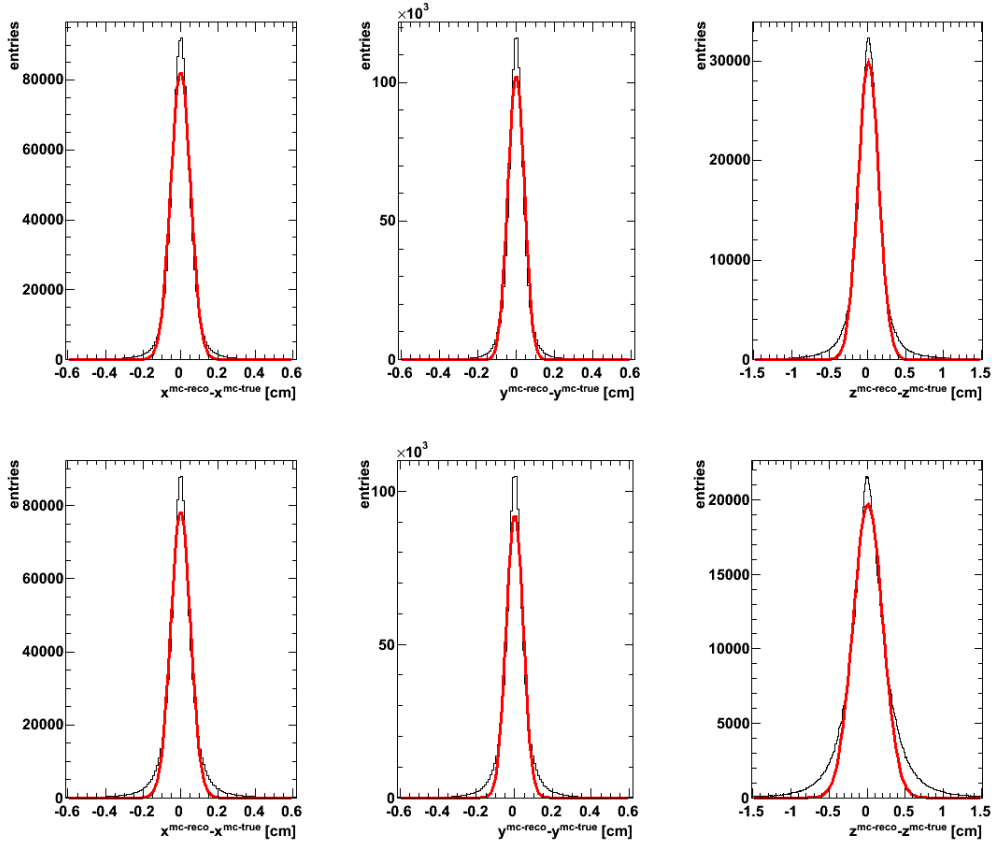


Figure 7.16: The resolution of the primary vertex (top) and the Λ decay vertex (bottom) along the three axes (x , y , z) from left to right, respectively. The red lines are Gaussian fits to the distributions.

Table 7.1: Primary and decay vertex resolution in the $\vec{p}p \rightarrow pK^+\Lambda$ reaction.

Vertex type	x [μm]	y [μm]	z [μm]
Primary vertex	529.3 ± 0.5	421.6 ± 0.4	1365 ± 1
Λ decay vertex	525.7 ± 0.6	438.5 ± 0.5	1947 ± 3

7.2.2.3 Momentum Resolution

The momentum resolution of the particles is usually expressed as the relative resolution by $(p_{mcreco.} - p_{mc})/p_{mc}$. Figure 7.17 shows the simulated momentum resolution of the final state particles in the $\vec{p}p \rightarrow pK^+\Lambda \rightarrow pK^+p\pi^-$ reaction. The Lorentzian function is fit to the distributions and the half width at half maximum (HWHM) of the fit functions are used to specify the momentum resolution. The Lorentzian function is given by

$$f(x) = \frac{p_0}{\pi} \frac{p_1}{(x - p_2)^2 + p_1^2} \quad (7.10)$$

where p_0 is the amplitude, p_2 is the mean and p_1 is the HWHM. The relative momentum resolution of the final state particles is summarized in Table 7.2.

Table 7.2: Momentum resolution of the particles in the $\vec{p}p \rightarrow pK^+\Lambda$ reaction.

Parameter	p	K^+	Λ	decay p	π^-
HWHM [%]	0.60	0.87	0.51	0.62	0.69

7.2.2.4 $p\Lambda$ Invariant Mass Resolution

The $p\Lambda$ invariant mass resolution is an important parameter which determines the resolution of the experiment to find narrow structures of different physics phenomena in the $p\Lambda$ subsystem. The $p\Lambda$ invariant mass resolution is given by $(m_{mcreco.}^{p\Lambda} - m_{mc}^{p\Lambda})$, and it is shown in Figure 7.18 fitted with the Lorentzian function. The Figure 7.18 shows that the $p\Lambda$ invariant mass resolution is $\approx 1.018 \text{ MeV}/c^2$. The high achieved resolution of the $p\Lambda$ invariant mass is mainly due to the performance of the high resolution straw tube tracker in the COSY-TOF spectrometer which improved the mass resolution by a factor of ~ 3 compared to the previous setup of the COSY-TOF detector without the STT [85].

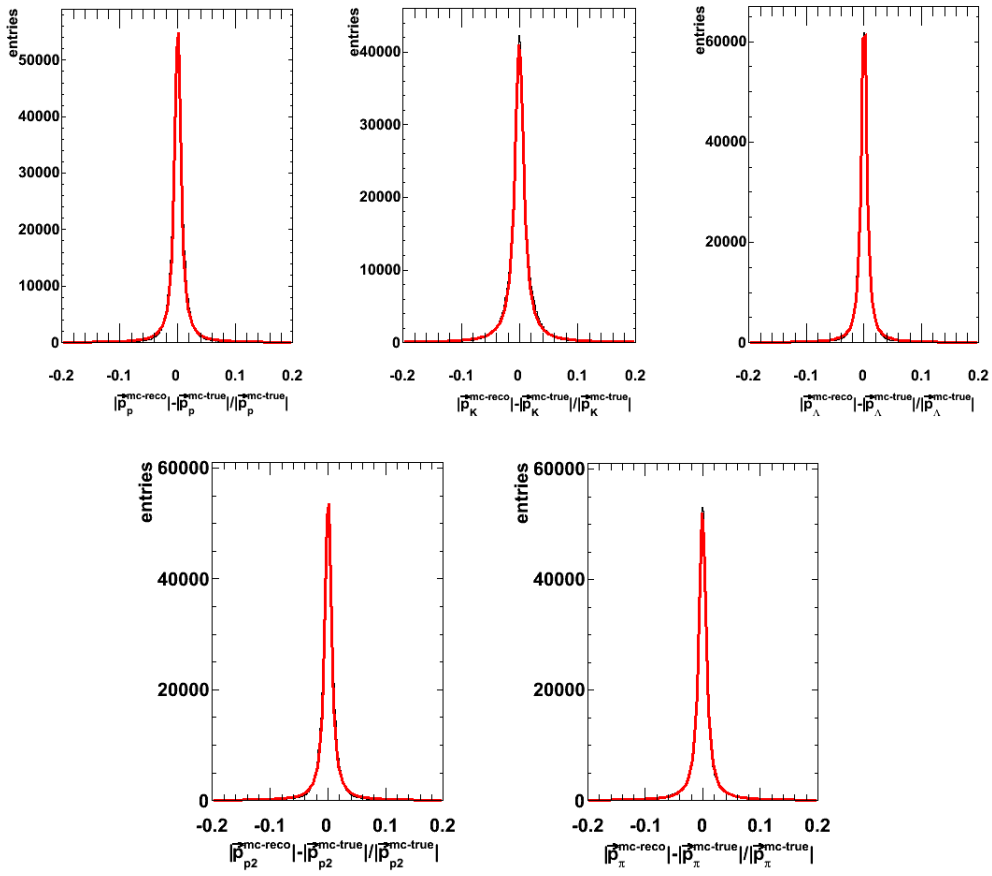


Figure 7.17: The momentum resolution of the primary particles (top) and the Λ decay particles (bottom) in the $\bar{p}p \rightarrow pK^+\Lambda \rightarrow pK^+p\pi^-$ reaction. The red lines indicate Lorentzian fits to the distributions.

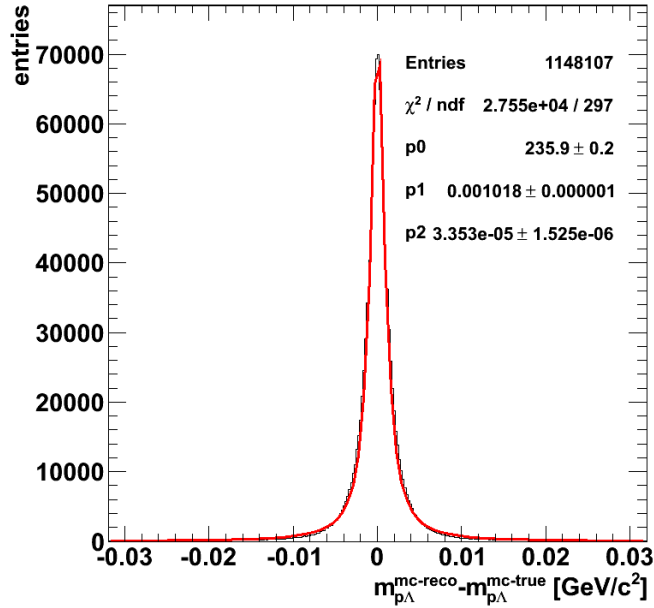


Figure 7.18: Simulated $p\Lambda$ invariant mass resolution. The red line shows a Lorentzian fit to the distribution.

7.2.3 Physical Observables

The $pK^+\Lambda$ events are analyzed to determine different physical observables in the reaction. Some of these observables are spin independent such as angular distributions and the Dalitz plot, and some of them are spin dependent like the analyzing power. The behavior of these observables is discussed in the following sections of this chapter.

7.2.3.1 Angular Distribution

The angular distribution for each of the three primary particles in the CMS is shown in Figure 7.19. All three distributions are corrected for the detector acceptance and reconstruction efficiency. The detector acceptance times efficiency which is shown below of each angular distribution plots is determined by comparing the reconstructed spectrum with the generated distribution from the Monte Carlo simulation. Since the particles in the entrance channel are identical (proton beam and proton target), the angular distribution of the particles in the CMS must be symmetric around zero. The symmetric behavior is seen in all three distributions in Figure 7.19. However, there is also some asymmetric behavior especially in the forward and backward direction. This is due to the incomplete description of the detector at small angles in the Monte Carlo simulation.

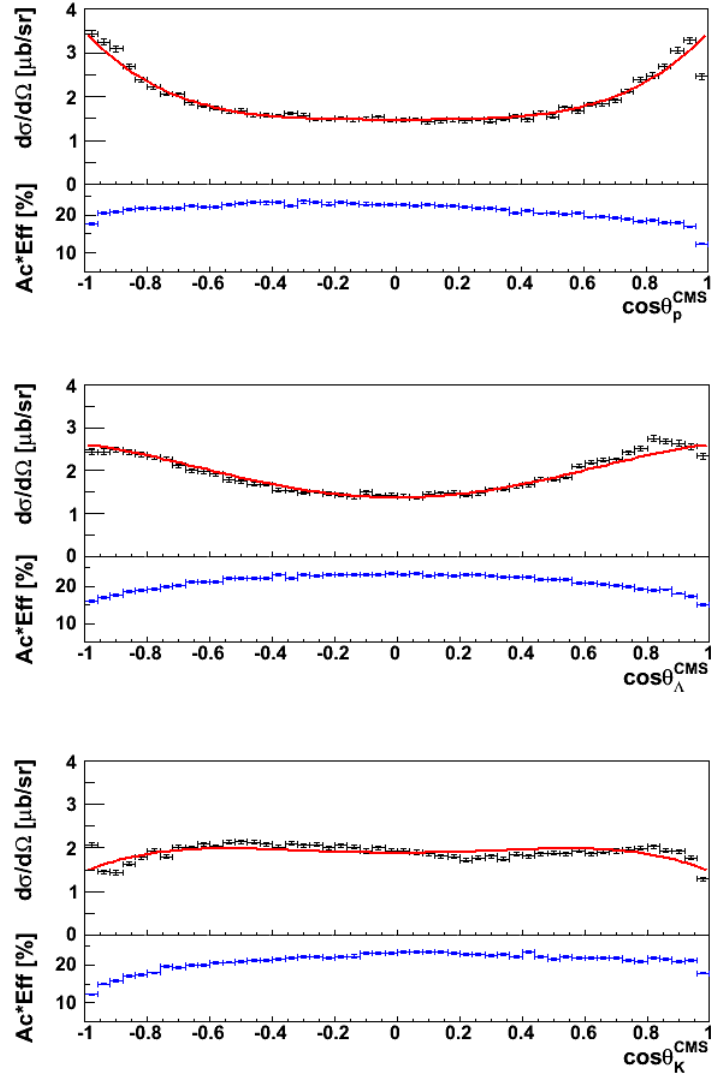


Figure 7.19: Angular distributions of the primary particles in the CMS for the selected $pK^+\Lambda$ events. The distributions are corrected for the detector acceptance and reconstruction efficiency. The detector acceptance and efficiency distribution is shown below each angular distribution. The red lines show fits (described in the text) to the p , Λ and K distributions for the top, center and bottom, respectively.

The angular distribution of scattered particles can be described in terms of Legendre polynomials $P_l(\cos \theta)$, $d\sigma/d\Omega = |\sum_{l=0}^{\infty} (2l+1)a_l P_l(\cos \theta)|^2$ where a_l is the corresponding partial wave amplitude. This formulation contains many cross terms. In general, the angular distributions of the particles are very complicated, but in the low energy region it is a good approximation to describe the distributions by expanding the Legendre polynomials based on $\cos^n \theta$ which gives the following fit function

$$\frac{d\sigma}{d\Omega} = C_0 + C_1 \cos^2 \theta + C_2 \cos^4 \theta + \text{higher_orders.} \quad (7.11)$$

The higher order terms can be neglected at low energies. The $\cos \theta$ and $\cos^3 \theta$ terms are not allowed here due to the asymmetric behavior. The coefficients of the function fitted to the angular distributions of the primary particles in the CMS are collected in Table 7.3.

Table 7.3: The coefficients of the function fitted to the angular distributions of primary particles in the CMS.

cos	C_0 [$\mu\text{b/sr}$]	C_1 [$\mu\text{b/sr}$]	C_2 [$\mu\text{b/sr}$]
θ_p^{CMS}	1.585 ± 0.011	-0.116 ± 0.088	2.533 ± 0.119
θ_Λ^{CMS}	1.452 ± 0.011	2.005 ± 0.088	-0.547 ± 0.115
θ_K^{CMS}	1.954 ± 0.013	0.651 ± 0.087	-1.076 ± 0.106

These coefficients are related to the squared amplitudes of different partial waves. The C_0 represents the squared partial wave amplitude of the S-wave and a cross term of S and D-waves and higher orders which are neglected here. The C_1 represents the squared amplitude of the P-wave and a cross term of P and D-waves. Finally, C_2 is related to the squared amplitude of the D-wave and cross terms of higher orders. The total cross section can also be formulated as

$$\sigma_{tot} \approx 2\pi(2C_0 + 2/3C_1 + 2/5C_2) + \text{higher_orders.} \quad (7.12)$$

The fitting coefficients show that both S and D-wave contributions are dominant for the proton distribution, whereas in the Λ distribution all S, P and D-waves play an important role. The fitting coefficients of the kaon distribution indicate the dominant interference of the S and D-waves.

The angular distributions of the primary particles in the CMS are not directly related to the different contributions to the reaction mechanism. This can be seen in the angular distributions in the Helicity frames. In a three body reaction $a + b \rightarrow 1\ 2\ 3$, the Helicity angle is defined as the angle between particle 1 and particle 2 or 3 in the CMS of $\{23\}$ subsystem called

$\{23\}$ rest frame. Therefore, three different Helicity angles can be defined for the three body final state reaction. As shown in Figure 7.20, these angles are θ_{Kp} in the $\{p\Lambda\}$ and $\{K\Lambda\}$ rest frames and for $\theta_{\Lambda p}$ in the $\{pK\}$ rest frame. The distributions are corrected for the detector acceptance and reconstruction efficiency shown below the angular distributions. The Helicity angular distributions are simply the distributions in the two body subsystems, and they are influenced by the physical effects from other subsystems. In the absence of any dynamical effects, the Helicity angular distributions are isotropic. However, physical effects involved in the reaction distort the isotropic distributions. The Helicity angle distributions are a special type of Dalitz plot projection.

The influence of resonances decaying into the $\{K\Lambda\}$ subsystem is revealed in the $\{p\Lambda\}$ and $\{pK\}$ subsystems [86]. The sum of the $N^*(1650)$ and $N^*(1720)$ resonances involved in the $\vec{p}p \rightarrow pK^+\Lambda$ reaction introduces an enhancement at $\cos\theta_{Kp}^{Rp\Lambda} = -1$ in the $\{p\Lambda\}$ rest frame and at the center of the $\{pK\}$ rest frame (Figure 7.20 top and bottom). The $p\Lambda$ final state interaction is also seen as a strong enhancement at $\cos\theta_{Kp}^{RK\Lambda} = -1$ in the $\{K\Lambda\}$ rest frame and $\cos\theta_{\Lambda p}^{RpK} = 1$ in the $\{pK\}$ rest frame in Figure 7.20 (center and bottom).

7.2.3.2 Dalitz Plot

The Dalitz plot is a useful tool to understand the reaction mechanism for reactions with three or more particles in the final state. The Dalitz plot is usually shown as a two dimensional plot of two invariant masses squared of two body subsystems. The Dalitz plot of the selected $pK^+\Lambda$ events at the excess energy $\varepsilon = 204$ MeV plotted as $m_{p\Lambda}^2$ vs. m_{pK}^2 , $m_{p\Lambda}^2$ vs. $m_{K\Lambda}^2$ and m_{pK}^2 vs. $m_{K\Lambda}^2$ is presented in Figure 7.21.

The double differential cross section of the $m_{p\Lambda}^2$ vs. $m_{K\Lambda}^2$ Dalitz plot is given by [73]

$$\frac{d\sigma}{dm_{p\Lambda}^2 dm_{K\Lambda}^2} = \frac{|M(S, m_{p\Lambda}^2, m_{K\Lambda}^2)|^2}{2^8 \pi^3 S \lambda(S, m_b^2, m_t^2)^{1/2}}, \quad (7.13)$$

where m_{ij} is the invariant mass of the $\{ij\}$ subsystem, S is the invariant mass squared of the initial channel, λ is the Källén function as $\lambda(x, y, z) = (x - y - z)^2 - 4yz$ and m_b and m_t are the masses of the beam and the target particles, respectively. $|M|^2$ is the amplitude of the reaction and contains all the dynamics. Therefore, the Dalitz plot is useful to understand the reaction mechanism. If there is no physical effect in the reaction, $|M|^2$ is a constant, hence the kinematically allowed region of the Dalitz plot is populated uniformly. Any variation from an isotropic population results from dynamical effects involved in the reaction.

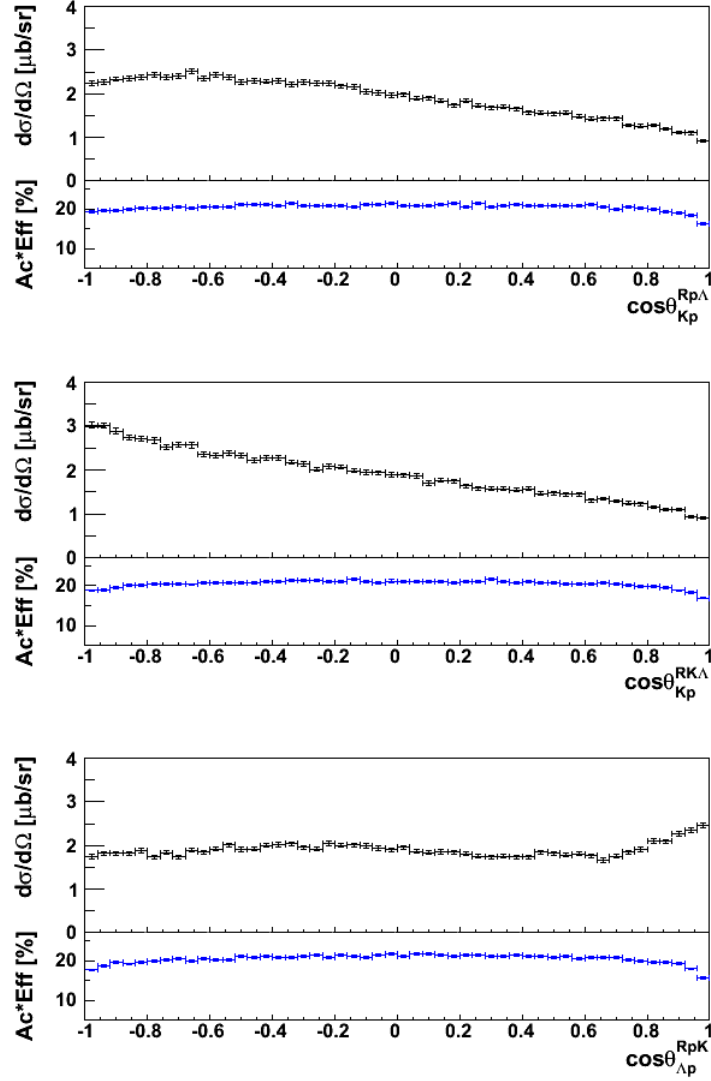


Figure 7.20: Angular distributions of the three Helicity angles of $\theta_{Kp}^{Rp\Lambda}$, $\theta_{Kp}^{RK\Lambda}$ and $\theta_{\Lambda p}^{RpK}$ from top to bottom, respectively. The distributions are corrected for the detector acceptance and reconstruction efficiency which are shown below each angular distribution.

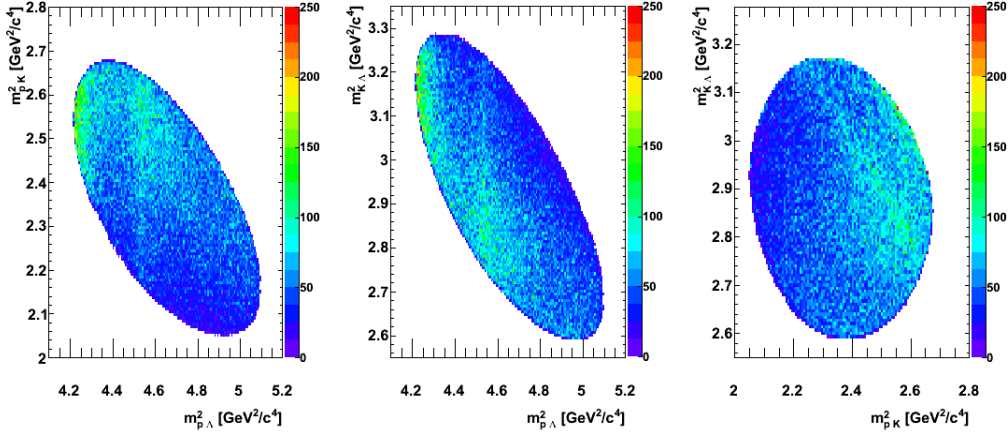


Figure 7.21: Acceptance corrected Dalitz plot of the selected $pK^+\Lambda$ events with three different combinations of the invariant mass squared on the axes.

The Dalitz plot in $m_{p\Lambda}^2$ vs. $m_{K\Lambda}^2$ is more suitable for the analysis of the reaction mechanism since different physical effects are seen in $\{p\Lambda\}$ and $\{K\Lambda\}$ subsystems. The measured Dalitz plot is compared with Monte Carlo simulation in Figure 7.22. Both plots are corrected for the detector acceptance and efficiency by comparing the reconstructed and generated phase space distribution of the Monte Carlo simulation. The Dalitz plot distribution shows that the COSY-TOF detector covers the complete kinematically allowed region of the $\bar{p}p \rightarrow pK^+\Lambda$ reaction. Since the Monte Carlo event generator produces uniform phase space distribution, the Dalitz plot from the simulation is homogeneously populated. In contrast, the Dalitz plot of the data deviates from homogeneity, so that significant enhancements are seen on the left side and in the center of the Dalitz plot.

The strong enhancement at the center of the Dalitz plot is due to the so called cusp effect which is seen in the $\{p\Lambda\}$ subsystem. There are two $N\Sigma$ cusp effects, a cusp at the $p\Sigma^0$ threshold ($4.54 \text{ GeV}^2/c^4$) and another cusp at the $n\Sigma^+$ threshold ($4.53 \text{ GeV}^2/c^4$). The difference of these two cusp thresholds is about $1.98 \text{ MeV}/c^2$ which cannot be separated with the available statistics even with invariant mass resolution of about $1 \text{ MeV}/c^2$. Another strong enhancement is seen on the left side of the Dalitz plot due to the $p\Lambda$ final state interaction at low $p\Lambda$ invariant masses. Furthermore, there are some other effects in the $\{K\Lambda\}$ subsystem that influence the Dalitz plot distribution. The $N^*(1650)$, $N^*(1710)$ and $N^*(1720)$ resonances are the main effects in $\{K\Lambda\}$ subsystem, however they are not seen as narrow structures in the Dalitz plot distribution due to their large width of about 100 MeV . In addition, at the $K\Sigma^0$ threshold ($2.84 \text{ GeV}^2/c^4$) in the $\{K\Lambda\}$ subsystem a

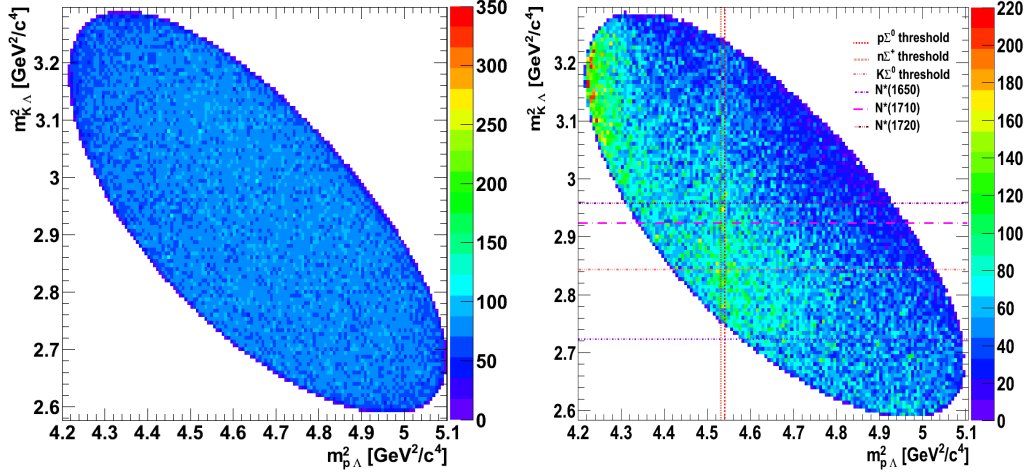


Figure 7.22: Acceptance corrected Dalitz plot for uniform phase space distribution from the Monte Carlo simulation (left) and for the measured $pK^+\Lambda$ events at the excess energy $\varepsilon = 204$ MeV as a function of $m_{p\Lambda}^2$ and $m_{K\Lambda}^2$. The measured Dalitz plot clearly deviates from an isotropic distribution. The colored lines on the Dalitz plot show different effects involved in the reaction.

cusps can be predicted.

The x and y axis projections of the Dalitz plot are the spectra of the invariant mass squared distribution of the $\{p\Lambda\}$ and $\{K\Lambda\}$ subsystems and they are shown in Figure 7.23. The solid curves indicate the phase space distribution normalized to the data distribution. In comparison to the uniform phase space distribution, the measured spectra show different physical effects involved in the reaction.

Because the cross section is a function of both $m_{p\Lambda}^2$ and $m_{K\Lambda}^2$, different physical structures in each subsystem can interfere with each other. The resonances in the $\{K\Lambda\}$ subsystem interfere with the final state interaction and the cusp effects in the $\{p\Lambda\}$ subsystem. Therefore, it is not possible to analyze each of these effects separately. However, it is possible to examine the influence of the resonances on other physical effects by applying constraints on the Dalitz plot. The Dalitz plot constraint is done using the Helicity angle $\cos\theta_{pK}^{Rp\Lambda}$ in the $\{p\Lambda\}$ rest frame which is given by [73, 87]

$$\cos\theta_{pK}^{Rp\Lambda} = \frac{2m_{K\Lambda}^2(m_p^2 + m_\Lambda^2 - m_{p\Lambda}^2) + (S - m_{K\Lambda}^2 - m_p^2)(m_{K\Lambda}^2 + m_\Lambda - m_K)}{\lambda^{1/2}(S, m_{K\Lambda}^2, m_p^2)\lambda^{1/2}(m_{K\Lambda}^2, m_\Lambda^2, m_K^2)}, \quad (7.14)$$

where m_{ij} is the invariant mass of the $\{ij\}$ subsystem, S is the invariant mass squared of the initial channel and λ is the Källén function. For any fixed

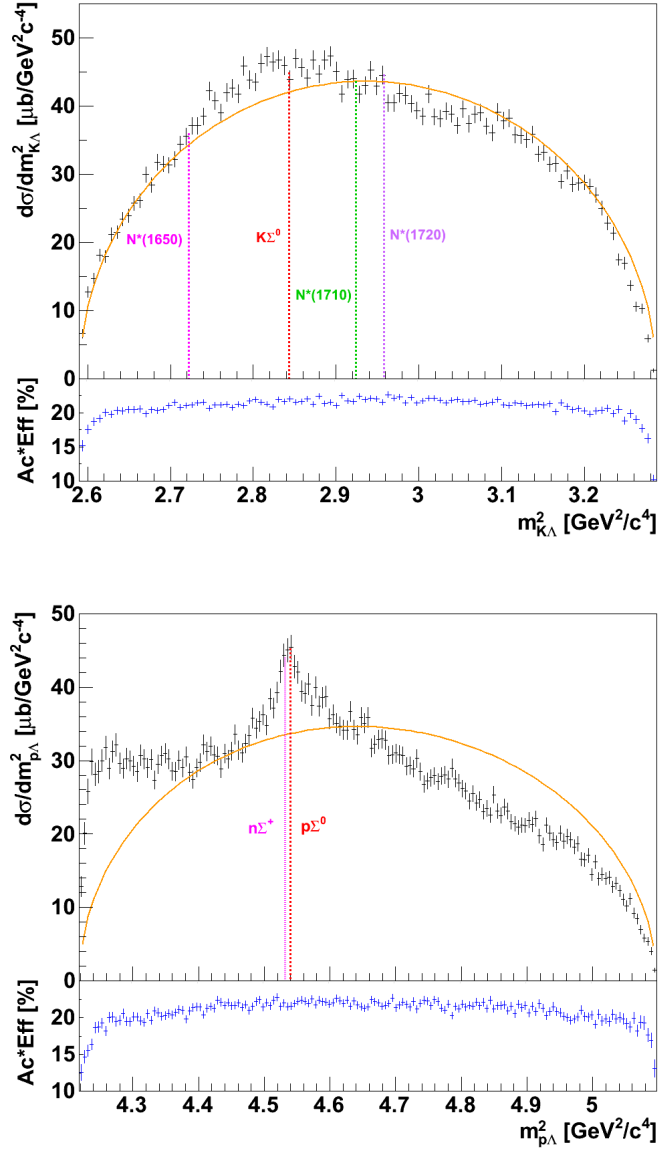


Figure 7.23: Dalitz plot projections along the $m_{K\Lambda}^2$ (top) and $m_{p\Lambda}^2$ (bottom) axes. The solid lines show the phase space distributions normalized to the data. Different physical effects are indicated by the vertical lines. The detector acceptance and reconstruction efficiency is shown below each distribution. In the $\{p\Lambda\}$ subsystem the strong enhancements are due to the $N\Sigma$ cusp effect and the $p\Lambda$ final state interaction. In the $\{K\Lambda\}$ subsystem the Breit-Wigner mass of different N^* resonances and the $K\Sigma^0$ threshold are indicated.

value of $m_{p\Lambda}^2$, the Helicity angle $\cos\theta_{pK}^{Rp\Lambda}$ defines the allowed range of $m_{K\Lambda}^2$. Therefore, equal bins of $\cos\theta_{pK}^{Rp\Lambda}$ between ± 1 divide the Dalitz plot into different sections with equal phase space volume. Figure 7.24 (top) shows the divided Dalitz plot into three sections of equal phase space volume by a constraint on $\cos\theta_{pK}^{Rp\Lambda}$. From left to right these constraints are $\cos\theta_{pK}^{Rp\Lambda} \geq 0.33$, $-0.33 < \cos\theta_{pK}^{Rp\Lambda} < 0.33$ and $\cos\theta_{pK}^{Rp\Lambda} \leq -0.33$. The projections of these three sections of the Dalitz plot on the $m_{p\Lambda}^2$ axis are shown in Figure 7.24 (bottom).

It is expected that the influence of the N^* resonances in the upper section of the Dalitz plot with $\cos\theta_{pK}^{Rp\Lambda} \geq 0.33$ is reduced. The $m_{p\Lambda}^2$ distribution in Figure 7.24 (bottom) shows that indeed the distribution for $\cos\theta_{pK}^{Rp\Lambda} \geq 0.33$ is in the full mass range lower than the distributions of the other sections. The other sections contain a higher contribution from excitation of N^* resonances to the reaction mechanism and to the cross section. Furthermore, the $m_{p\Lambda}^2$ plot exhibits that the cusp effect enhances significantly in the lower part of the Dalitz plot $\cos\theta_{pK}^{Rp\Lambda} \leq -0.33$, so that it may distort the FSI enhancement.

The same study is done for the $\{K\Lambda\}$ subsystem by dividing the Dalitz plot according to the Helicity angle $\cos\theta_{pK}^{RK\Lambda}$ in the $\{K\Lambda\}$ rest frame which is given by [73, 87]

$$\cos\theta_{pK}^{RK\Lambda} = \frac{2m_{p\Lambda}^2(m_K^2 + m_\Lambda^2 - m_{K\Lambda}^2) + (S - m_{p\Lambda}^2 - m_K^2)(m_{p\Lambda}^2 + m_\Lambda - m_K)}{\lambda^{1/2}(S, m_{p\Lambda}^2, m_K^2)\lambda^{1/2}(m_{p\Lambda}^2, m_\Lambda^2, m_p^2)}, \quad (7.15)$$

Similar to the $\{p\Lambda\}$ channel, three constraints are applied on the Dalitz plot using $\cos\theta_{pK}^{RK\Lambda} \geq 0.33$, $-0.33 < \cos\theta_{pK}^{RK\Lambda} < 0.33$ and $\cos\theta_{pK}^{RK\Lambda} \leq -0.33$. Figure 7.25 (top) shows the three sections of the Dalitz plot. The y-axis projections of these sections on the $\{K\Lambda\}$ subsystem are shown in Figure 7.25 (bottom). The $m_{K\Lambda}^2$ plots show that the section with $\cos\theta_{pK}^{RK\Lambda} \geq 0.33$ has less contribution to the total cross section, while significant enhancements are seen in $\cos\theta_{pK}^{RK\Lambda} \leq -0.33$. The enhancements in this section are mainly due to N^* resonances decaying to the $\{K\Lambda\}$ channel and the reflection of physical effects from the $\{p\Lambda\}$ subsystem. The center bump is the reflection of the $N\Sigma$ cusp effect, and the $p\Lambda$ FSI reflection is clearly seen on the right. The N^* resonances generally exhibit band structures in the Dalitz plot projections, however, due to their width of more than 100 MeV they do not appear as narrow structures in this channel. The $m_{K\Lambda}^2$ plot in $\cos\theta_{pK}^{RK\Lambda} \leq -0.33$ shows that the N^* resonances are in the position of the cusp reflection. Therefore, the N^* resonances may be responsible for the enhancements of the cusp effect in the $\{p\Lambda\}$ channel for $\cos\theta_{pK}^{Rp\Lambda} \leq -0.33$ section of the Dalitz plot. However, the reason for such a significant intensification of the cusp

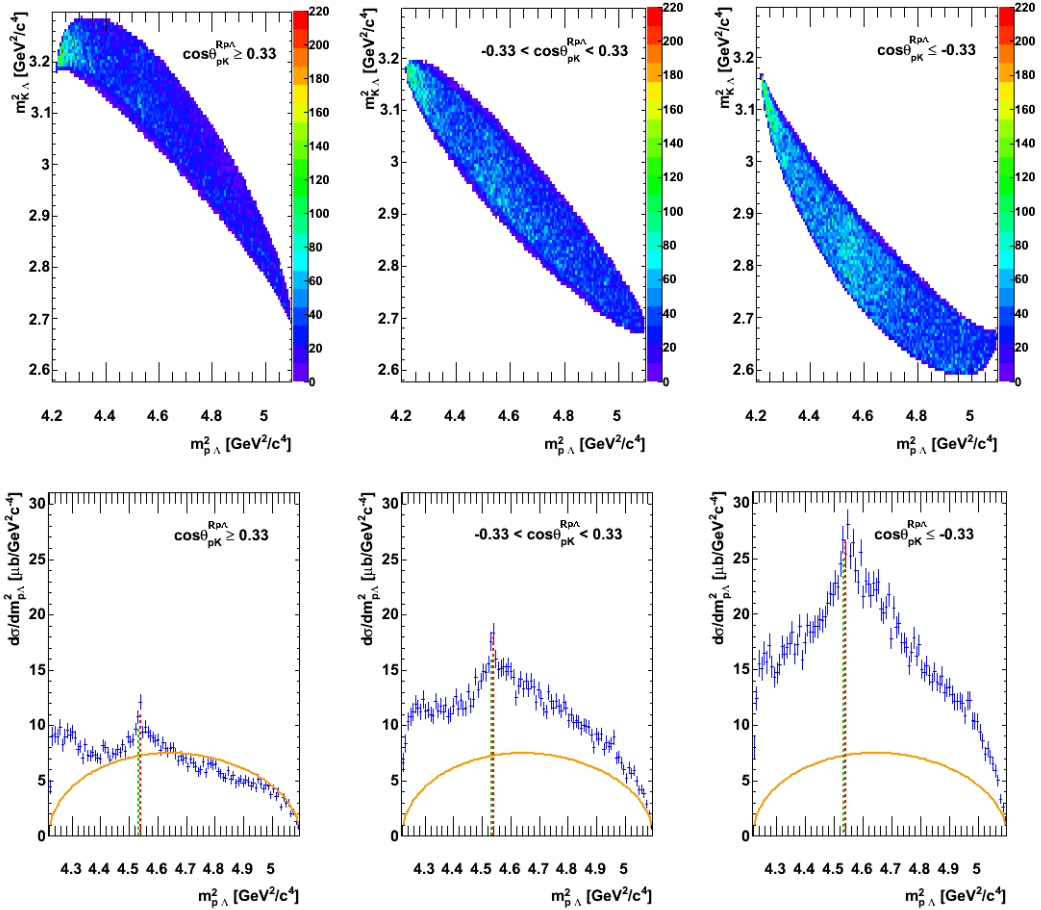


Figure 7.24: (Top) three sections of the Dalitz plot with equal phase space volume with the constraints $\cos\theta_{pK}^{Rp\Lambda} \geq 0.33$ (left), $-0.33 < \cos\theta_{pK}^{Rp\Lambda} < 0.33$ (center) and $\cos\theta_{pK}^{Rp\Lambda} \leq -0.33$ (right). (Bottom) the three sections of the Dalitz plot projected onto the $m_{p\Lambda}^2$. The solid curves indicate the phase space distributions normalized in area to the data with $\cos\theta_{pK}^{Rp\Lambda} \geq 0.33$. The dashed lines show the $n\Sigma^+$ and $p\Sigma^0$ thresholds for the cusp effect.

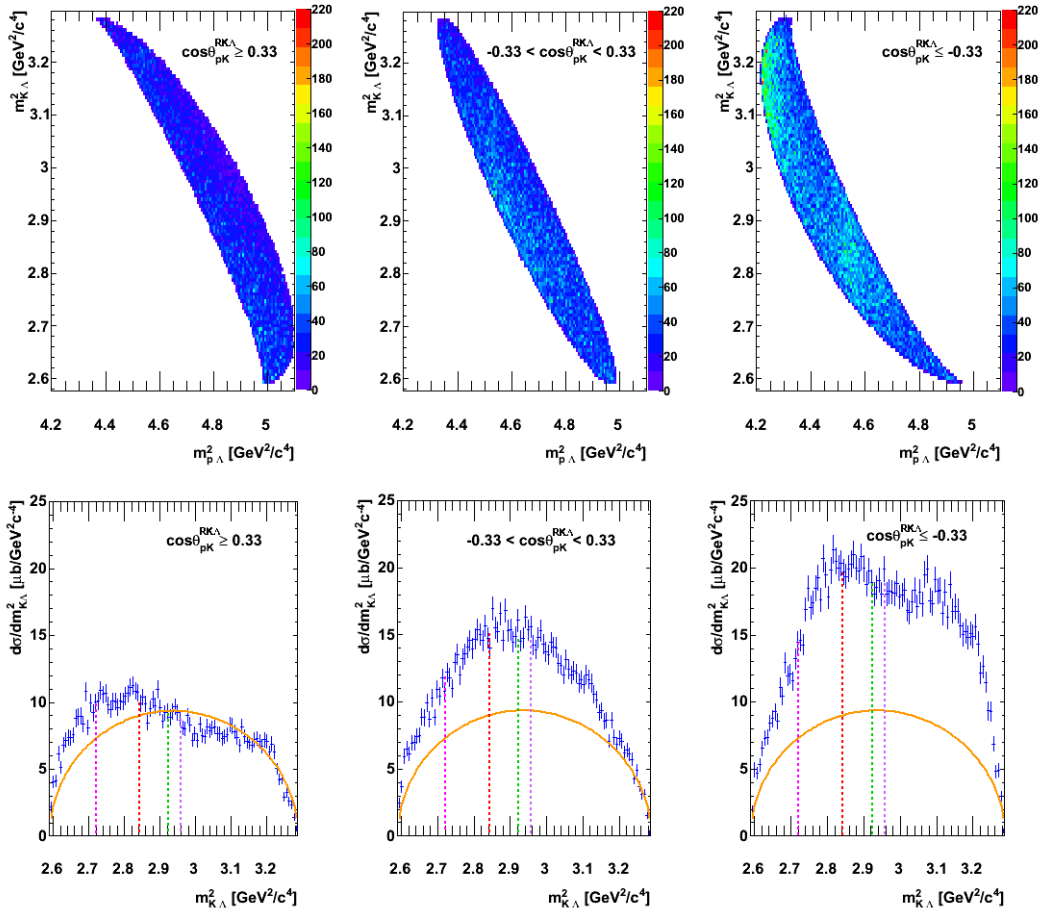


Figure 7.25: (Top) three sections of the Dalitz plot with equal phase space volume with the constraints $\cos\theta_{pK}^{RK\Lambda} \geq 0.33$ (left), $-0.33 < \cos\theta_{pK}^{RK\Lambda} < 0.33$ (center) and $\cos\theta_{pK}^{RK\Lambda} \leq -0.33$ (right). (Bottom) The three sections of the Dalitz plot projected onto the $m_{K\Lambda}^2$ axis. The solid curves indicate the phase space distributions normalized to the area of the data with $\cos\theta_{pK}^{RK\Lambda} \geq 0.33$. The dashed lines show the position of the $N^*(1650)$, $K\Sigma^0$ threshold, $N^*(1710)$ and $N^*(1720)$, from left to right.

effect in the $\{p\Lambda\}$ channel is still unclear. A similar analysis of the Dalitz plot and its projections is done for the $\{pK\}$ subsystem, but any significant structure is not found. This behavior is predicted due to the strong repulsive coulomb force between the proton and kaon.

7.2.3.3 $p\Lambda$ Invariant Mass

The high mass resolution of $\approx 1 \text{ MeV}/c^2$ achieved in this work, makes it possible to apply a small binning of $2 \text{ MeV}/c^2$ in the linear invariant mass distribution $m_{p\Lambda}$ to study the involved physical effects in this subsystem. Therefore, the $m_{p\Lambda}$ distribution for all three sections of the Dalitz plot are determined. For better comparison they are plotted in the same graph, as shown in Figure 7.26. All distributions are corrected for the detector acceptance and reconstruction efficiency. As Figure 7.26 shows the FSI shape at lower $p\Lambda$ invariant masses is not distorted by the cusp effect up to $30 \text{ MeV}/c^2$ above threshold. On the other hand, Figure 7.26 shows that the cusp shape changes in the three sections of the Dalitz plot.

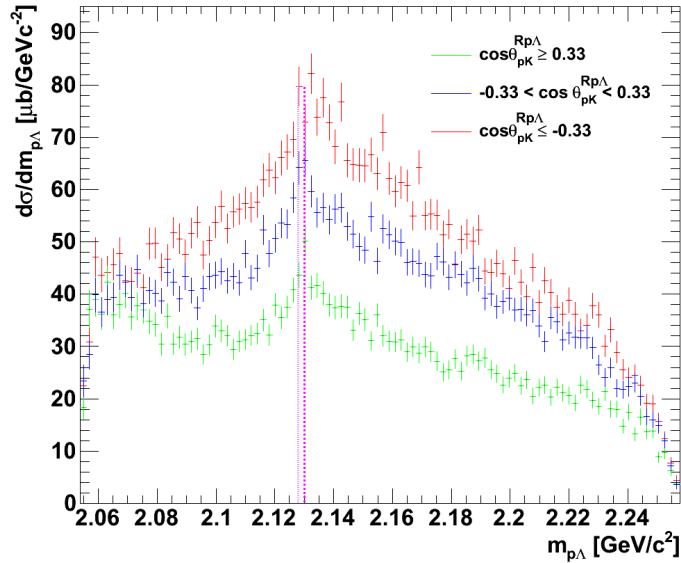


Figure 7.26: The $p\Lambda$ invariant mass distributions for the three sections of the Dalitz plot based on the applied constraints on $\cos \theta_{pK}^{Rp\Lambda}$ in the $\{p\Lambda\}$ rest frame. The FSI enhancement is on the left and the cusp effect is seen as an enhancement in the center. The dashed lines exhibit the $N\Sigma$ thresholds.

The $p\Lambda$ -FSI effect has been studied in detail in a previous work and the effective scattering length is determined from the shape of the FSI [57, 61].

Therefore, only the position, the shape and the angular distribution of the cusp are studied here.

7.2.3.4 $N\Sigma$ Cusp

The enhancement at the center of the $m_{p\Lambda}$ close to the $N\Sigma$ threshold can be explained as a coupled channel effect between the $N\Sigma$ and $p\Lambda$ systems. In order to analyze the shape of the enhancement, two relativistic Breit-Wigner distributions are fit incoherently to the data at the cusp range chosen between 2.11 to 2.18 GeV/c^2 , as shown in Figure 7.27. The fitting results show that the cusp shape is different in the three sections of the Dalitz plot, and it is wider in the $\cos\theta_{pK}^{Rp\Lambda} \leq -0.33$ section. In addition, a shoulder is visible at $p\Lambda$ invariant masses above the $N\Sigma$ threshold in the cusp range. Shoulder is more pronounced in the lower section of the Dalitz plot with $\cos\theta_{pK}^{Rp\Lambda} \leq -0.33$. Such a shoulder has also been seen in some other experiments [88].

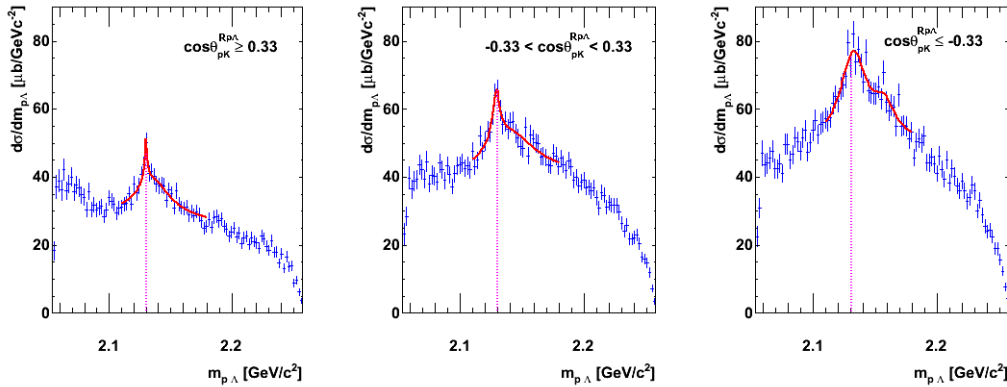


Figure 7.27: The $p\Lambda$ invariant mass distribution for the three sections of the Dalitz plot fit with two relativistic Breit-Wigner functions to the cusp range from 2.11 to 2.18 GeV/c^2 . The dashed line shows the $p\Sigma^0$ threshold.

The fitting parameters for the two Breit-Wigner functions are collected in Table 7.2. The results show that the mean of the first Breit-Wigner distribution is close to the $p\Sigma^0$ threshold at 2.1309 GeV/c^2 for all three sections, but the width clearly increases in the lower sections of the Dalitz plot. Because there is no known structure for the shoulder part in the $\{p\Lambda\}$ subsystem, a possible explanation is the presence of a resonance. The existence of a narrow resonance in the $\{p\Lambda\}$ subsystem at 2.140 GeV/c^2 is predicted theoretically [88, 89], however, it has not been confirmed yet. Similar in this analysis such a resonance at 2.140 GeV/c^2 cannot be confirmed, since the

mean of the second Breit-Wigner distribution depends on the cusp range, especially for $\cos\theta_{pK}^{Rp\Lambda} \leq -0.33$ it deviates strongly from $2.140 \text{ GeV}/c^2$.

Table 7.4: The fit parameters obtained by fitting the cusp area with two Breit-Wigner distributions.

Parameter	fitting values		
	$\cos\theta_{pK}^{Rp\Lambda} \geq 0.33$	$-0.33 < \cos\theta_{pK}^{Rp\Lambda} < 0.33$	$\cos\theta_{pK}^{Rp\Lambda} \leq -0.33$
χ^2/ndf	0.526	0.927	0.959
$m_1 [\text{GeV}/c^2]$	2.130 ± 0.001	2.129 ± 0.001	2.132 ± 0.001
$\Gamma_1 [\text{GeV}/c^2]$	0.0032 ± 0.0022	0.0069 ± 0.0034	0.0256 ± 0.0050
$m_2 [\text{GeV}/c^2]$	2.135 ± 0.003	2.14 ± 0.01	2.157 ± 0.003
$\Gamma_2 [\text{GeV}/c^2]$	0.0355 ± 0.0126	0.0588 ± 0.0208	0.0314 ± 0.0252

In addition to the Breit-Wigner distribution, the $N\Sigma$ cusp effect is fit with a Flatté distribution [85, 88] which has a different behavior below and above the $N\Sigma$ threshold, in order to compare the data with a similar analysis in Ref. [85]. However, this distribution can only produce a single peak and cannot generate the shoulder which is seen in the distributions. Moreover, there is no parameter to extract the cusp width from the Flatté distribution. In general, it is questionable if a Flatté distribution is suited for the description of the enhancement at the $N\Sigma$ threshold because Flatté assumes a resonance which should couple to the $p\Lambda$ and $N\Sigma$ channels. However, such an resonance is unknown from theoretical study.

Since there is no theoretical description for the cusp effect in the $pp \rightarrow pK^+\Lambda$ reaction, it is not possible to extract precisely the parameters of the $N\Sigma$ cusp in this channel at this stage. However, from Figure 7.27 it seems that the cusp shape changes in the different sections of the Dalitz plot although the reason for that is unclear.

$N\Sigma$ Cusp Angular Distribution In order to calculate the angular distribution of the events in the cusp enhancement, the $p\Lambda$ invariant mass distribution is plotted for eight equal angular bins of $d\cos\theta_K^{CMS}$. The polar angle of the kaon in the CMS (θ_K^{CMS}) is used, since the kaon and $\{p\Lambda\}$ subsystem have the same polar angle distribution, $\theta_K^{CMS} = 180^\circ - \theta_{\{p\Lambda\}}^{CMS}$. Like in the last section, the cusp study is limited to the range from 2.11 to 2.18 MeV/c^2 in the $\{p\Lambda\}$ subsystem. The cusp angular distribution is determined by subtracting the background from the cusp enhancement in each bin of the kaon polar angle. The background is estimated by the phase space distribution. The difference of the integration of the phase space distribution and the data in the limited range of the cusp gives the differential cross

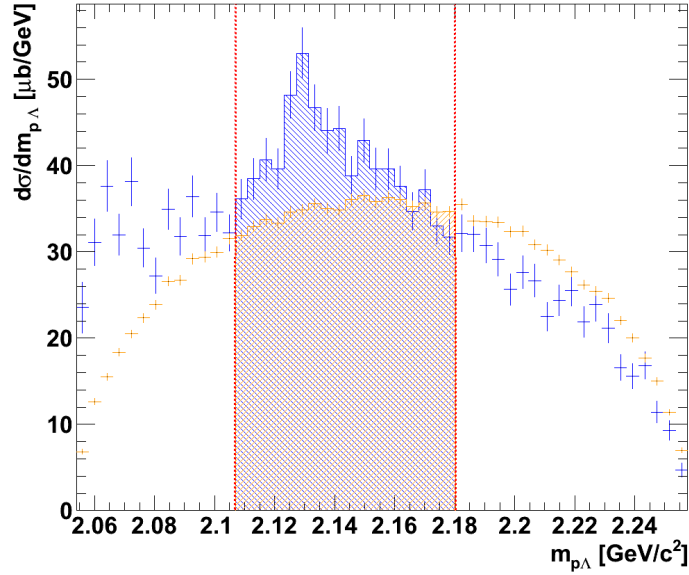


Figure 7.28: The invariant mass distribution in a bin of $\cos\theta_K^{CMS}$. The red dashed lines show the interesting area to study the cusp effect. The hatched areas indicate the area of the cusp and background.

section for the corresponding $d\cos\theta_K^{CMS}$ bin. In Figure 7.28 the invariant mass spectrum is shown together with the integration of phase space and data indicated by the hatched areas between the integration limits marked by the red dashed lines. The same study is done for the three sections of the Dalitz plot in order to identify any changes in the behavior of the $N\Sigma$ cusp effect. Figure 7.29 shows the angular distribution of the cusp obtained for the full data and the three sections of the Dalitz plot.

Because the $N\Sigma$ cusp is produced exactly at the threshold of the $\{N\Sigma\}$ system, the Σ and N are in relative S-wave and the spin-parity of the $N\Sigma$ system is $J_p = 0^+$ or 1^+ at the threshold. Therefore, the $p\Lambda$ resulting from the $N\Sigma$ can only be in relative S or D-waves due to momentum and parity conservation [85]. Hence, the cusp distribution is fit with Legendre polynomial functions of zeroth and second order as

$$\frac{d\sigma}{d\cos\theta_K^{CMS}} = 2\pi|a_0P_0(\cos\theta) + 5a_2P_2(\cos\theta)|^2 = p_0 + p_1\cos^2\theta + p_2\cos^4\theta. \quad (7.16)$$

The results show that the angular distribution of the cusp has a symmetric behavior. Considering the errors, the obtained fit parameters show the strong influence of the p_0 term compared to the other parameters. Therefore, a dominant S-wave contribution can be considered. The behavior of the angular distribution is the same for the Dalitz plot subsamples determined

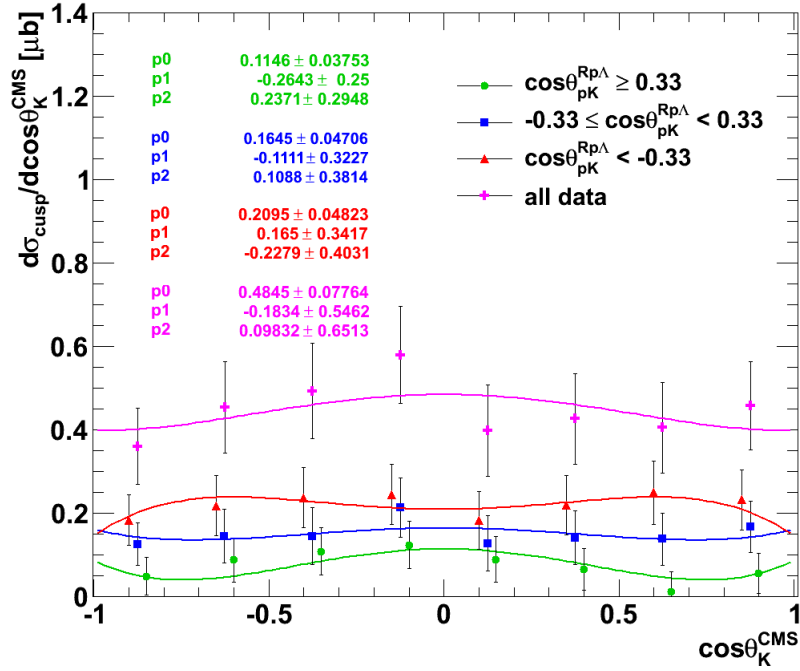


Figure 7.29: Angular distribution of the $N\Sigma$ cusp as a function of the kaon polar angle in the CMS obtained for the full data and the three sections of the Dalitz plot. The points belonging to the same bins are shifted on the x axis for clarity. The solid lines indicate the fits to the distributions.

by the constraints on the Helicity angle. This behavior is also confirmed by the Helicity angular distribution study (see Figure 7.20), where no structure is seen in different rest frames for the $N\Sigma$ cusp effect.

7.2.3.5 Analyzing Power

The analyzing power of the primary particles is an important spin dependent observable which can be determined in the $\vec{p}p \rightarrow pK^+\Lambda$ reaction with the COSY-TOF detector due to the polarized beam. In the $\vec{p}p \rightarrow pK^+\Lambda$ reaction at $p_{beam} = 2.95 \text{ GeV}/c$ the primary particles with different values of angular momentum l are produced, and the interference between different l -values can be seen in their analyzing power distribution. The analyzing power of particles is determined with the same method used to extract the beam polarization with pp elastic scattering events discussed in Section 7.1.4. In order to characterize the analyzing power the cosine of the polar angle and the ϕ distribution of the particles are divided into 8 bins and the asymmetry for each $\cos\theta$ bin is determined. The mean asymmetry is then divided by the beam polarization to obtain the analyzing power of the particles.

Kaon Analyzing Power The result for the kaon analyzing power as a function of $\cos\theta_K$ in the CMS is shown in Figure 7.30. The analyzing power in forward and backward directions has to go to zero due to the non defined left-right asymmetry in these two regions. At $p_{beam} = 2.95$ GeV/ c the kaon has enough momentum so that the (S,P) and (S,D)-wave interference contributions can be seen in its analyzing power. Ignoring higher order contributions of partial waves, the kaon analyzing power is given by [57, 90]

$$A_N = \frac{\Im(S, P) \sin\theta + \Im(S, D) \sin 2\theta}{|S|^2 + |P|^2 + |D|^2} \approx \alpha P_1^1(\cos\theta) + \beta P_2^1(\cos\theta) \quad (7.17)$$

where $\Im(i, j)$ is the imaginary part of the partial wave amplitudes for the contributions i and j . The interference of (S,P) is symmetric in the cosine of the kaon polar angle in the CMS, whereas the (S,D) interference is antisymmetric. Therefore, the analyzing power distribution is fit using the associated Legendre polynomial functions of $P_l^m(\cos\theta)$ as shown in Figure 7.30. The $P_1^1(\cos\theta)$ describes the (S,P) interference while the (S,D) interference is characterized by $P_2^1(\cos\theta)$ and higher orders are ignored. As Figure 7.30 shows the kaon analyzing power is well fitted with both the (S,P) and (S,D) interference terms.

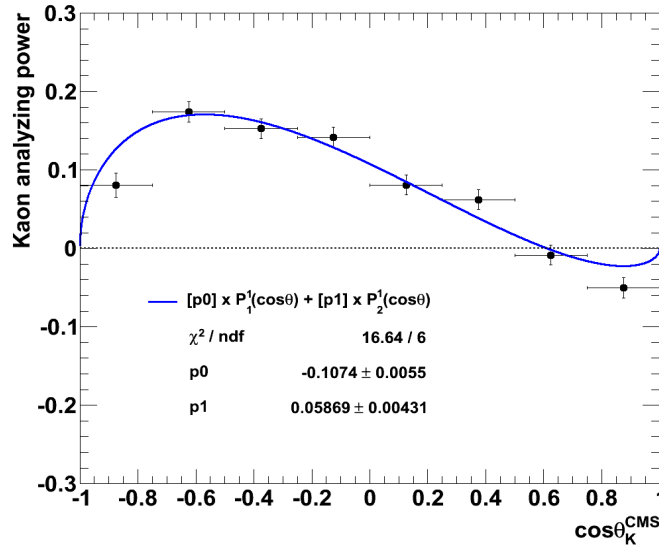


Figure 7.30: Analyzing power of kaon as a function of its polar angle in CMS. The solid line indicates a fit with the associated Legendre polynomials $P_1^1(\cos\theta)$ and $P_2^1(\cos\theta)$.

The kaon analyzing power distribution is also determined for different bins of the $p\Lambda$ invariant mass in order to investigate the modification of the

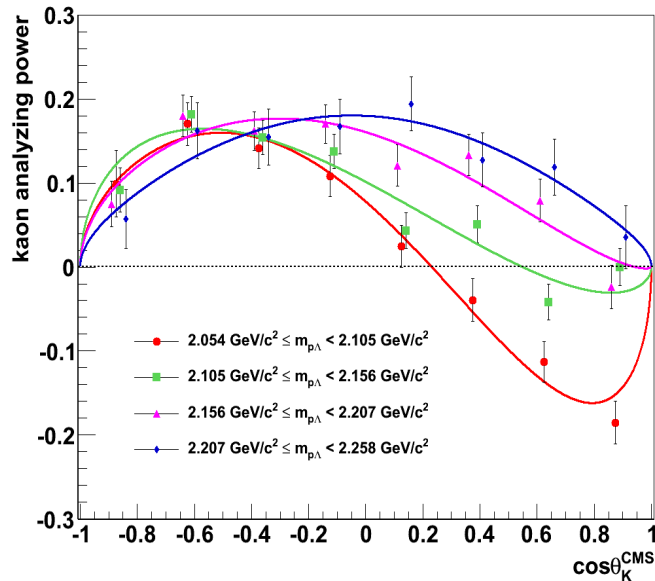


Figure 7.31: Kaon analyzing power in four bins of the $p\Lambda$ invariant mass. The solid lines indicate the associated Legendre polynomial fit. The points belonging to the same $\cos\theta$ bins are shifted on the x axis for clarity.

kaon analyzing power due to changes of the kaon momentum. The results are seen in Figure 7.31 for four bins of $m_{p\Lambda}$. As Figure 7.31 shows the kaon analyzing power is more symmetric for higher $m_{p\Lambda}$ invariant masses. This behavior is expected since the kaon momentum is low for high $m_{p\Lambda}$ so that the contribution of D wave vanishes.

The results of the kaon analyzing power in six bins of $m_{p\Lambda}$ is summarized in Figure 7.32 for the (S,P) contribution on the left and the (S,D) contribution on the right. It is seen that the (S,D) contribution decrease with increasing $m_{p\Lambda}$ due to the reduction of the kaon momentum. The (S,P) contribution of the kaon for low $m_{p\Lambda}$ where the $\{p\Lambda\}$ system is in S-wave can be used to extract the $p\Lambda$ spin-triplet scattering length from the $p\Lambda$ final state interaction (for more details see Ref. [57, 61, 90]). The results show that the (S,P) contribution for low $m_{p\Lambda}$ is non zero with 2σ confidence, which could not be observed in the previous $pK^+\Lambda$ analysis at the same beam momentum [57].

Proton Analyzing Power The analyzing power of the proton is determined in the same way as described in the last section. The proton analyzing power distribution versus cosine of the proton polar angle in the CMS and its fit with associated Legendre polynomials are shown in Figure 7.33. Figure 7.33 depicts that the analyzing power of the proton has a symmetric behav-

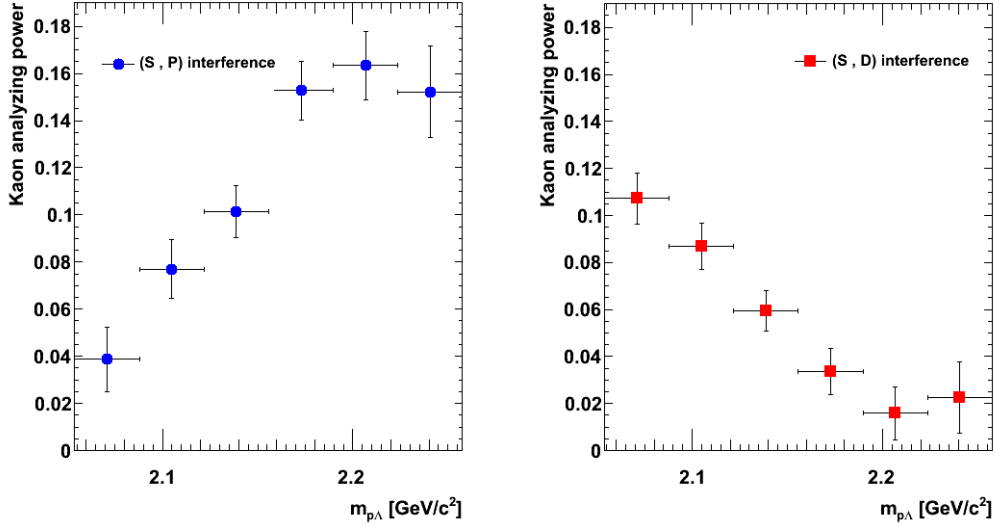


Figure 7.32: The (S,P) contribution coefficient (left) and the (S,D) contribution coefficient (right) as a function of $m_{p\Lambda}$ extracted from fits of associated Legendre polynomials to the kaon analyzing power.

ior over the full range of $\cos\theta_p^{CMS}$. The fit parameters show that $P_2^1(\cos\theta)$ does not have a significant effect in the proton analyzing power distribution, and the symmetric term of $P_1^1(\cos\theta)$ is more dominant.

The analyzing power of the proton is determined in different bins of the $K\Lambda$ invariant mass (Figure 7.34). As Figure 7.34 shows, the analyzing power of the proton decreases toward zero with increasing $m_{K\Lambda}$. A simple explanation for this behavior is a vanishing of P and D-wave contributions at high $m_{K\Lambda}$ since the the proton momentum is low. However, a complete explanation needs the partial wave analysis taking into account the behavior of the analyzing power and the angular distribution.

Lambda Analyzing Power The Λ analyzing power is determined in the same way as described for the kaon and proton. The lambda analyzing power distribution as a function of cosine of the lambda polar angle in the CMS is shown in Figure 7.35. The distribution is fit with associated Legendre polynomial functions. The fit parameters show that both the (S,P) and (S,D) contributions are dominant in the lambda analyzing power distribution.

The Λ analyzing power is determined for different bins of the Kp invariant mass which is shown in Figure 7.36. The results in Figure 7.36 for four bins of m_{Kp} shows that the Λ analyzing power significantly decreases

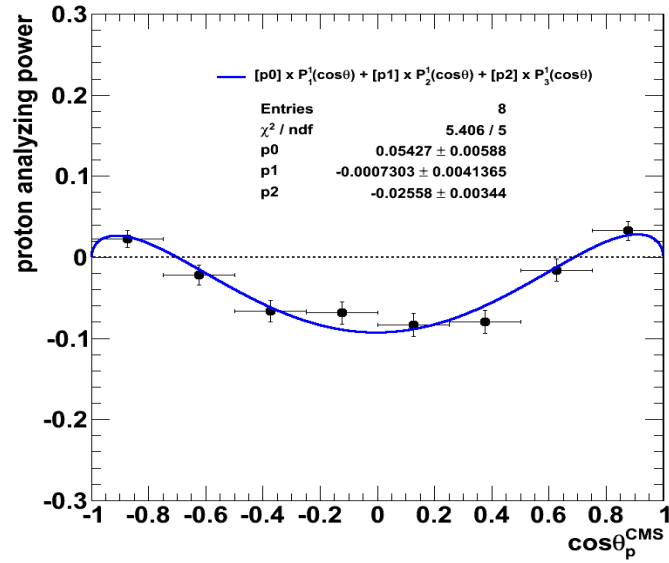


Figure 7.33: Proton analyzing power as a function of the polar angle in the CMS. The solid line indicates a fit with associated Legendre polynomials. In order to obtain a better χ^2/ndf , the polynomial $P_3^1(\cos\theta)$ has been added.

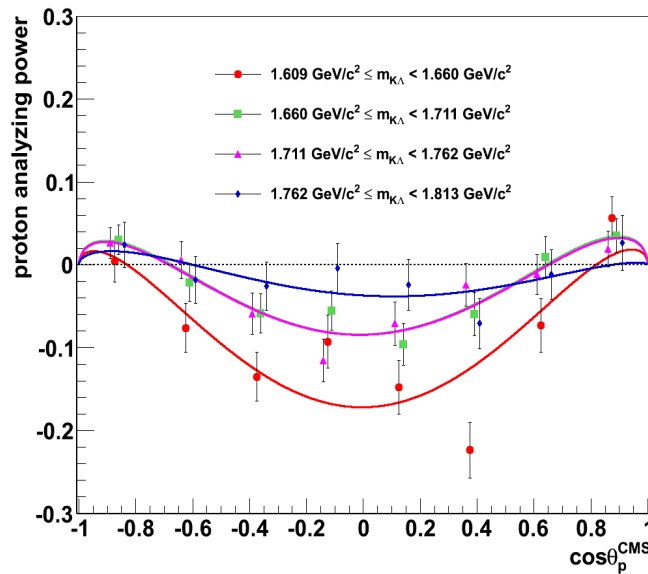


Figure 7.34: Proton analyzing power in four bins of the $K\Lambda$ invariant mass. The solid lines indicate the fit with the associated Legendre polynomials. The analyzing power of the proton at the middle range of $m_{K\Lambda}$ shows similar fitting result. The points belonging to the same $\cos\theta$ bins are shifted on the x axis for clarity.

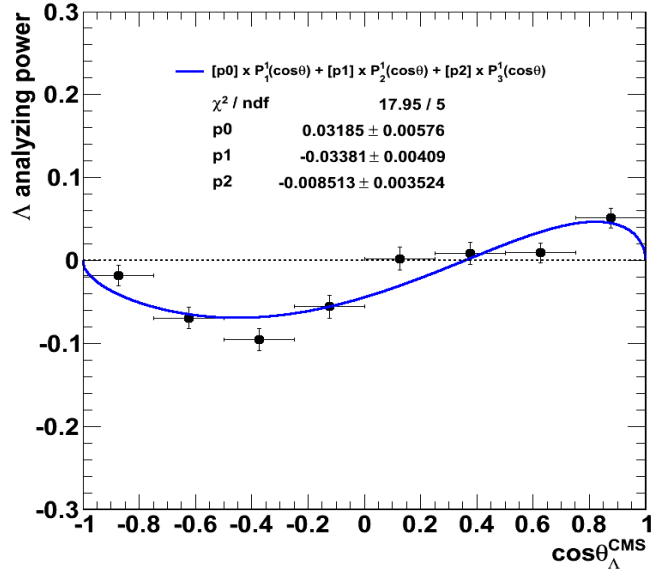


Figure 7.35: Analyzing power of Λ particles as a function of the Λ polar angle in CMS. The solid line indicates the fit with the associated Legendre polynomials.

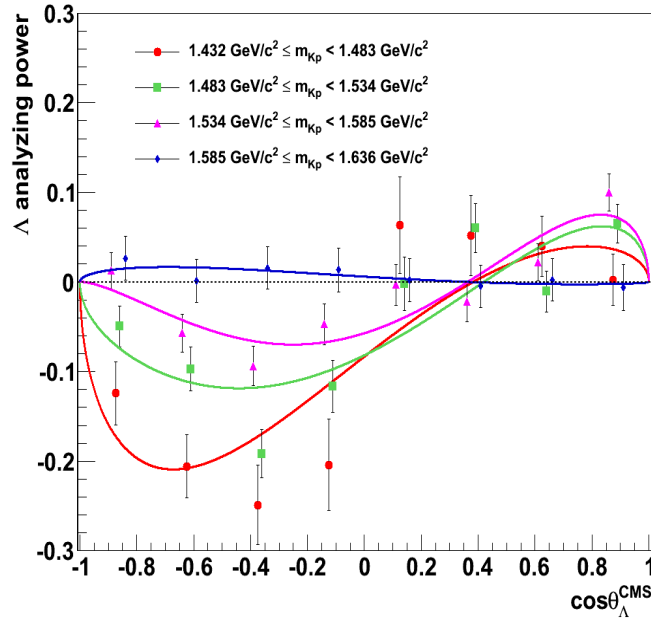


Figure 7.36: Analyzing power of Λ for different bins of the Kp invariant mass. The solid lines indicate the fits with the associated Legendre polynomials. The points belonging to the same $\cos\theta$ bins are shifted on the x axis for clarity.

with increasing the m_{Kp} , so that the contribution of P and D-wave vanishes at high m_{Kp} corresponding to low lambda momentum. However, a precise explanation needs the partial wave analysis.

Summary and Outlook

Straw tube detectors of the self-supporting type are used in the COSY-TOF experiment for tracking of charged particles. The same type of detector was proposed for the PANDA experiment planned for high luminosity measurements with antiproton beam at the FAIR accelerator complex. In the presented work, operation of the straw tube detectors and their capability for particle identification in the PANDA experiment was simulated with the Garfield program. Furthermore, the tracking performance of the straw detector was studied with the analysis of measured data for the $\vec{p}p \rightarrow pK^+\Lambda$ reaction from the COSY-TOF experiment.

The gas gain in the straw tube, measured as a function of the anode wire voltage for a gas mixture of Ar + CO₂ (90 : 10) was well reproduced by the simulation with the Magboltz and Garfield program after including a 34% Penning transfer rate. Moreover, the straw tube output signals were convoluted with the transfer function of the designed front-end readout electronics for the PANDA straw tube tracker, in order to analyze the applicability of the straws for PID and to optimize the readout electronics parameters. The front-end electronics parameters were set with a ⁵⁵Fe source to remove the ion tail in the output signals. The tail cancelation reduced the pile-up and base line fluctuation. Therefore, the straw signals are suitable for high counting rates in the PANDA experiment, which reach 800 kHz for the straw tubes in the innermost STT layers. The particle identification based on the charged particle energy losses in a straw tube tracker comprising 24 straw tube layers was studied using the time over threshold and the integrated charge information corrected for the track distance to the anode wire. A truncated average was calculated by removing 30% of the highest values. Subsequently, the values were used to calculate the separation of protons, charged pions and kaons in the momentum range below 0.6 GeV/c, which is a requirement for the PANDA straw tube tracker. The separation powers based on the TOT and charge integration methods are comparable and satisfy the PANDA requirements.

Since the PANDA detector is not yet ready for measurements, the COSY-TOF detector is used to study the straw tube detector performance in

charged particle tracking. The $\vec{p}p \rightarrow pK^+\Lambda$ reaction measured with a polarized proton beam at 2.95 GeV/c momentum was reconstructed and analyzed using only straw tube tracker information. For this aim, the straw tube tracker was precisely calibrated and its average spatial resolution was determined to be 146 μm . The Monte Carlo simulation displayed a high reconstruction efficiency of $(20.4 \pm 0.05)\%$ with only the STT for the $\vec{p}p \rightarrow pK^+\Lambda$ final state after applying selection criteria and suppressing background events. A high $p\Lambda$ invariant mass resolution of $\approx 1.0 \text{ MeV}/c^2$ was achieved using the straw tube tracker, which is about three times better than the previous setup of the COSY-TOF detector without the STT. The beam polarization was determined to be $(87.5 \pm 2.0)\%$ from the analysis of pp elastic scattering events.

A high statistics data sample of about 130,000 $pK^+\Lambda$ events was obtained for the further analysis of the observables. The COSY-TOF detector kinematically covers the full phase space for the $\vec{p}p \rightarrow pK^+\Lambda$ reaction and the Dalitz plot with the selected $pK^+\Lambda$ events presented this fact. The Dalitz plot contains significant enhancements at the low $m_{p\Lambda}$ region due to the $p\Lambda$ -FSI and at $N\Sigma$ thresholds due to a $N\Sigma$ - $p\Lambda$ coupled channel effect called cusp. The enhancements are clearly seen in the $p\Lambda$ invariant mass projection, as well. The analysis of different physical effects in the $p\Lambda$ subsystem was provided with high mass resolution. For the first time the cusp shape was studied in different regions of the Dalitz plot by means of constraints on the helicity angle $\cos\theta_{pK}^{Rp\Lambda}$. The results indicated that the $N\Sigma$ cusp effect is stronger at the low region of the Dalitz plot with $\cos\theta_{pK}^{Rp\Lambda} \leq -0.33$. This might be due to the influence of N^* resonances. The study of the cusp angular distribution also showed a dominant S-wave contribution, which was confirmed by the Helicity angular distribution results.

Using the polarized beam, the analyzing power as a function of the proton, kaon and lambda scattering angle was determined. The results indicated that the proton analyzing power is more symmetric than the kaon and lambda analyzing power. Compared to the previous COSY-TOF measurement at 2.95 GeV/c beam momentum [57, 84], the (S,P)-wave interference contribution to the kaon analyzing power is non-zero at low $m_{p\Lambda}$ within 2σ . Therefore, the extraction of the $p\Lambda$ spin triplet scattering length might be possible.

For a further analysis, the straw tube spatial resolution simulation with Garfield can be done for different discrimination threshold levels. The separation power for the TOT and integrated charge methods has to be simulated for different setups of the front-end readout electronics for the PANDA STT. In addition, different discrimination threshold levels can be examined. For a more realistic study of the PANDA STT, the magnetic field should be

considered at the different steps of the simulation.

In the $pK\Lambda$ analysis the behavior of the $N\Sigma$ cusp effect has to be theoretically explained. Such a theoretical explanation is also helpful to estimate the background contribution in the $N\Sigma$ cusp and its angular distribution. In addition, the Λ polarization and spin transfer coefficient D_{NN} can be determined from the data presented in this work. The analysis of the $p\Lambda$ FSI at $2.95\text{ GeV}/c$ presented in Ref. [57, 84] has to be investigated in the new approach of different Dalitz plot regions with this high statistics data. A similar analysis has been done for the data at $2.7\text{ GeV}/c$ in Ref. [61]. The $p\Lambda$ -FSI, $N\Sigma$ cusp and the Λ polarization in the $\vec{p}p \rightarrow pK^+\Lambda$ reaction can be compared with other COSY-TOF data measured at $2.7\text{ GeV}/c$ and $3.2\text{ GeV}/c$ in order to determine any changes in the behavior of these observables with beam momentum.

Appendix A

Garfield Script

*An Example Script for the Simulation of the Straw Tube Detector Signal with Garfield

```
&CELL
Global wire = 0.002
Global volt = 1800
Tube r = 0.5   v = 0
Rows
S 1 wire 0 0 volt

&FIELD
Area -0.5 -0.5 0.5 0.5

&MAGNETIC
Components 0.0 0.0 0.0   Tesla

&GAS
Global pressure = 2*760
Global temperature = 300
Global gas-file = "ARCO2-9010-2bar.GAS"
If exist{gas-file} then
get {gas-file}
Else
Magboltz ARGON 90 CO2 10
Write {gas-file}
Endif
Heed ARGON 90 CO2 10
```

*Apply Townsend corection for Penning effect with Magboltz 8.9.5

Read-vector	E[V/cm]	v_d [cm/ μ s]	dl[cm]	dt[μ s]	α [cm ⁻¹]	attachement[cm ⁻¹]	α^{corr} [cm ⁻¹]
	30000	63.2	465.8	1141.0	65.2	6.9	155.71
	50000	86.4	752.8	1174.2	320.9	5.0	534.91
	70000	109.4	785.5	992.1	696.2	3.7	1010.60
	90000	132.1	791.9	993.9	1138.8	2.8	1541.41
	110000	153.8	795.4	1056.7	1622.2	2.1	2097.47
	130000	175.1	704.7	1007.0	2108.8	2.0	2651.22
	150000	195.5	738.2	1012.5	2616.8	1.7	3213.24
	170000	215.8	786.1	995.8	3102.0	1.4	3741.64
	190000	234.8	812.0	997.9	3615.3	1.2	4303.98
	210000	255.9	835.1	1011.2	4106.8	1.0	4836.56
	230000	274.8	909.6	1023.0	4583.0	0.9	5342.81
	250000	292.8	905.0	1026.5	5078.6	0.8	5874.93
	270000	312.0	950.3	1044.8	5544.7	0.8	6368.83
	290000	330.7	955.3	1048.7	6001.8	0.7	6853.32
	310000	350.2	997.8	1088.5	6447.0	0.6	7322.64
	320000	358.0	985.1	1057.7	6671.2	0.7	7557.31

Global E/P = E/pressure
 Global α /P = α^{corr} /pressure
 Global attachement/P = attachement/pressure
 Add drift-velocity v_d vs E/P
 Add townsend α /P vs E/P
 Add attachement attachement/P vs E/P

* Signal of Fe-55 x-Ray crossing perpendicular to the straw wire with
 0.1 cm distance to wire
 &SIGNAL
 Area -0.5 -0.5 0.5 0.5
 Window 0 0.001 1000
 Global gain = 44000
 avalanche polya-fixed {gain}
 Track 0.1 0 -50 0.1 0 50 Gamma Energy 5.9 keV
 Signal avalanche average-signal 2 new noattachement diffusion electron-pulse
 ion-pulse ion-tail
 plot-signals

Appendix B

Data Tables

Table 5: The results of the second order polynomial function fit to the resolution distribution of different straw double layers.

Double layer	p_0	p_1	p_2
1	0.0224	-0.0430	0.0277
2	0.0223	-0.0353	0.0191
3	0.0203	-0.0349	0.0194
4	0.0191	-0.0213	0.0028
5	0.0225	-0.0421	0.0295
6	0.0255	-0.0509	0.0366
7	0.0204	-0.0231	0.0028
8	0.0224	-0.0336	0.0174
9	0.0218	-0.0383	0.0268
10	0.0221	-0.0388	0.0271
11	0.0224	-0.0361	0.0139
12	0.0209	-0.0379	0.0115
13	0.0214	-0.0375	0.0171

Table 6: Acceptance corrected Dalitz plot projection on to $m_{p\Lambda}^2$, normalized to the total cross section 23.9 [μb].

$m_{p\Lambda}^2$ [GeV ² /c ⁴]	$d\sigma/dm_{p\Lambda}^2$ [$\mu\text{b}/\text{GeV}^2c^{-4}$]	error	$m_{p\Lambda}^2$ [GeV ² /c ⁴]	$d\sigma/dm_{p\Lambda}^2$ [$\mu\text{b}/\text{GeV}^2c^{-4}$]	error
4.221	12.5	1.4	4.381	30.7	1.3
4.227	20.0	1.6	4.386	28.4	1.2
4.232	25.1	1.7	4.392	27.4	1.2
4.237	30.2	1.9	4.397	29.1	1.2
4.243	28.1	1.6	4.402	29.6	1.2
4.248	29.0	1.6	4.408	32.0	1.3
4.253	29.4	1.6	4.413	31.1	1.3
4.259	31.5	1.6	4.418	32.1	1.3
4.264	28.7	1.5	4.424	30.7	1.3
4.269	30.5	1.5	4.429	31.1	1.3
4.275	32.1	1.6	4.434	29.3	1.2
4.279	29.5	1.4	4.439	31.4	1.3
4.285	28.7	1.4	4.445	30.5	1.3
4.290	29.8	1.4	4.450	31.2	1.3
4.296	30.2	1.4	4.456	33.4	1.3
4.301	29.1	1.4	4.461	31.4	1.3
4.307	28.7	1.3	4.466	31.2	1.3
4.312	30.1	1.4	4.472	32.3	1.3
4.317	29.5	1.4	4.477	33.3	1.3
4.322	28.7	1.3	4.482	35.8	1.4
4.328	30.2	1.4	4.487	34.1	1.3
4.333	27.5	1.3	4.493	35.7	1.4
4.338	29.5	1.3	4.498	36.1	1.4
4.344	30.1	1.3	4.503	34.5	1.3
4.349	30.7	1.3	4.509	39.0	1.5
4.354	30.0	1.3	4.514	36.6	1.4
4.359	28.9	1.3	4.519	39.7	1.5
4.365	28.6	1.3	4.525	42.0	1.6
4.370	30.2	1.3	4.530	44.1	1.6
4.376	28.9	1.3	4.535	44.4	1.6

$m_{p\Lambda}^2$ [GeV ² /c ⁴]	$d\sigma/dm_{p\Lambda}^2$ [$\mu\text{b}/\text{GeV}^2 c^{-4}$]	error	$m_{p\Lambda}^2$ [GeV ² /c ⁴]	$d\sigma/dm_{p\Lambda}^2$ [$\mu\text{b}/\text{GeV}^2 c^{-4}$]	error
4.541	45.0	1.6	4.700	31.1	1.3
4.546	42.6	1.6	4.706	30.4	1.2
4.551	42.0	1.5	4.711	30.7	1.2
4.557	39.2	1.4	4.716	29.6	1.2
4.562	39.3	1.5	4.722	29.5	1.2
4.567	40.8	1.5	4.727	29.0	1.2
4.573	37.5	1.4	4.732	30.2	1.2
4.578	39.6	1.5	4.738	28.8	1.2
4.583	37.6	1.4	4.743	27.0	1.1
4.589	38.8	1.5	4.748	27.1	1.1
4.594	38.9	1.5	4.754	27.8	1.8
4.599	35.8	1.4	4.759	28.1	1.2
4.605	36.2	1.4	4.764	27.2	1.2
4.609	34.7	1.3	4.769	27.8	1.2
4.615	34.9	1.3	4.775	28.1	1.2
4.621	34.1	1.3	4.780	27.4	1.2
4.626	34.3	1.3	4.786	29.3	1.3
4.631	36.5	1.4	4.791	28.0	1.2
4.637	34.1	1.3	4.796	26.9	1.2
4.642	33.5	1.3	4.802	25.9	1.1
4.647	36.1	1.4	4.807	25.7	1.1
4.652	34.8	1.4	4.812	24.3	1.1
4.658	36.6	1.4	4.817	25.1	1.1
4.663	31.6	1.3	4.823	24.4	1.1
4.668	32.2	1.3	4.828	24.8	1.1
4.674	32.7	1.3	4.833	22.9	1.0
4.679	33.0	1.3	4.839	23.7	1.1
4.684	32.6	1.3	4.844	22.6	1.0
4.689	30.8	1.2	4.849	25.6	1.1
4.695	30.8	1.2	4.855	23.3	1.1

$m_{p\Lambda}^2$ [GeV ² /c ⁴]	$d\sigma/dm_{p\Lambda}^2$ [μb/GeV ² c ⁻⁴]	error	$m_{p\Lambda}^2$ [GeV ² /c ⁴]	$d\sigma/dm_{p\Lambda}^2$ [μb/GeV ² c ⁻⁴]	error
4.860	22.8	1.1	4.982	16.9	0.9
4.865	23.8	1.1	4.988	16.6	0.9
4.871	23.1	1.1	4.993	17.1	0.9
4.876	21.9	1.0	4.998	14.2	0.8
4.881	21.7	1.0	5.004	16.3	0.9
4.887	20.8	1.0	5.009	14.2	0.9
4.892	21.3	1.0	5.014	14.0	0.9
4.897	21.3	1.0	5.019	14.1	0.9
4.903	22.2	1.1	5.025	14.1	0.9
4.908	21.4	1.0	5.030	13.0	0.8
4.913	22.0	1.1	5.036	13.5	0.9
4.919	20.0	1.0	5.041	12.5	0.8
4.924	18.6	1.0	5.046	11.1	0.8
4.929	21.3	1.1	5.052	10.3	0.7
4.935	19.9	1.0	5.057	11.2	0.8
4.939	19.4	1.0	5.062	9.10	0.7
4.945	19.1	1.0	5.068	8.60	0.7
4.951	20.3	1.0	5.073	7.10	0.6
4.956	19.3	1.0	5.078	5.90	0.6
4.961	19.8	1.0	5.084	5.30	0.5
4.967	19.5	1.0	5.089	4.10	0.5
4.972	18.0	1.0	5.094	1.40	0.3
4.977	18.5	1.0			

Table 7: Acceptance corrected Dalitz plot projection on to $m_{K\Lambda}^2$, normalized to the total cross section 23.9 [μb].

$m_{K\Lambda}^2$ [GeV ² /c ⁴]	$d\sigma/dm_{K\Lambda}^2$ [$\mu\text{b}/\text{GeV}^2c^{-4}$]	error	$m_{K\Lambda}^2$ [GeV ² /c ⁴]	$d\sigma/dm_{K\Lambda}^2$ [$\mu\text{b}/\text{GeV}^2c^{-4}$]	error
2.593	6.70	0.6	2.803	43.7	1.3
2.600	12.8	0.8	2.809	45.7	1.4
2.607	14.8	0.8	2.817	47.4	1.4
2.614	18.0	0.9	2.824	46.6	1.4
2.621	17.6	0.9	2.830	46.8	1.4
2.628	21.2	1.0	2.837	46.2	1.4
2.635	21.7	1.0	2.844	44.1	1.3
2.642	23.2	1.0	2.851	46.4	1.4
2.649	23.7	1.0	2.858	45.6	1.4
2.656	25.6	1.0	2.865	43.9	1.3
2.663	26.3	1.0	2.872	47.1	1.4
2.670	29.8	1.1	2.879	45.4	1.3
2.677	28.4	1.1	2.886	46.2	1.4
2.684	31.5	1.2	2.893	47.2	1.4
2.691	31.5	1.2	2.900	45.2	1.4
2.698	31.1	1.1	2.907	41.8	1.3
2.705	32.0	1.1	2.914	44.0	1.3
2.712	34.1	1.2	2.921	44.1	1.3
2.719	35.6	1.2	2.928	41.8	1.3
2.726	36.7	1.2	2.935	42.8	1.3
2.733	37.9	1.3	2.942	46.0	1.4
2.739	38.8	1.3	2.949	42.7	1.3
2.747	42.0	1.4	2.956	44.7	1.4
2.754	40.6	1.3	2.963	40.3	1.2
2.761	39.1	1.3	2.969	40.3	1.2
2.768	41.7	1.3	2.977	42.2	1.3
2.775	43.0	1.4	2.983	41.8	1.3
2.782	41.8	1.3	2.991	40.6	1.3
2.789	45.9	1.4	2.998	39.3	1.3
2.796	43.7	1.3	3.005	38.3	1.2

$m_{K\Lambda}^2$ [GeV ² /c ⁴]	$d\sigma/dm_{K\Lambda}^2$ [$\mu\text{b}/\text{GeV}^2c^{-4}$]	error	$m_{K\Lambda}^2$ [GeV ² /c ⁴]	$d\sigma/dm_{K\Lambda}^2$ [$\mu\text{b}/\text{GeV}^2c^{-4}$]	error
3.012	41.6	1.3	3.151	33.1	1.2
3.019	38.7	1.2	3.158	31.6	1.1
3.026	38.2	1.2	3.165	31.2	1.2
3.033	38.9	1.2	3.172	29.2	1.1
3.039	38.8	1.2	3.179	30.7	1.1
3.047	37.1	1.2	3.186	28.4	1.1
3.054	39.1	1.3	3.193	28.5	1.1
3.061	37.6	1.2	3.200	29.0	1.1
3.068	38.5	1.2	3.207	28.0	1.1
3.074	39.2	1.3	3.214	27.1	1.1
3.081	36.9	1.2	3.221	24.8	1.0
3.088	36.1	1.2	3.228	22.9	1.0
3.095	39.0	1.3	3.235	21.5	1.0
3.102	38.2	1.3	3.242	17.7	0.8
3.109	37.9	1.3	3.249	16.8	0.9
3.116	35.7	1.2	3.256	14.0	0.8
3.123	36.4	1.2	3.263	10.3	0.6
3.130	34.7	1.2	3.269	10.0	0.7
3.137	35.7	1.2	3.277	5.80	0.5
3.144	32.6	1.1	3.284	1.20	0.3

Table 8: Acceptance corrected angular distribution of the proton in the CMS, normalized to the total cross section 23.9 [μb].

$\cos(\theta_p^{CMS})$	$d\sigma/d\Omega$ [$\mu\text{b}/\text{sr}$]	error	$\cos(\theta_p^{CMS})$	$d\sigma/d\Omega$ [$\mu\text{b}/\text{sr}$]	error
-0.98	3.438	0.075	0.02	1.476	0.037
-0.94	3.248	0.067	0.06	1.479	0.038
-0.90	3.091	0.065	0.10	1.418	0.036
-0.86	2.685	0.057	0.14	1.450	0.037
-0.82	2.387	0.05	0.18	1.469	0.037
-0.78	2.224	0.050	0.22	1.442	0.037
-0.74	2.067	0.047	0.26	1.484	0.038
-0.70	2.049	0.047	0.30	1.441	0.037
-0.66	1.868	0.044	0.34	1.494	0.039
-0.62	1.788	0.043	0.38	1.554	0.040
-0.58	1.734	0.042	0.42	1.475	0.038
-0.54	1.669	0.040	0.46	1.620	0.042
-0.50	1.687	0.040	0.50	1.546	0.040
-0.46	1.579	0.038	0.54	1.752	0.044
-0.42	1.573	0.038	0.58	1.671	0.042
-0.38	1.563	0.038	0.62	1.822	0.046
-0.34	1.619	0.039	0.66	1.839	0.046
-0.30	1.572	0.038	0.70	1.914	0.048
-0.26	1.480	0.037	0.74	2.125	0.051
-0.22	1.485	0.037	0.78	2.382	0.057
-0.18	1.509	0.037	0.82	2.482	0.058
-0.14	1.476	0.037	0.86	2.679	0.062
-0.10	1.496	0.037	0.90	3.051	0.068
-0.06	1.534	0.038	0.94	3.283	0.074
-0.02	1.457	0.037	0.98	2.462	0.069

Table 9: Acceptance corrected angular distribution of the Λ in the CMS, normalized to the total cross section 23.9 [μb].

$\cos(\theta_{\Lambda}^{CMS})$	$d\sigma/d\Omega$	error	$\cos(\theta_{\Lambda}^{CMS})$	$d\sigma/d\Omega$	error
	[$\mu\text{b}/\text{sr}$]			[$\mu\text{b}/\text{sr}$]	
-0.98	2.445	0.061	0.02	1.403	0.036
-0.94	2.444	0.059	0.06	1.374	0.035
-0.90	2.496	0.059	0.10	1.465	0.037
-0.86	2.421	0.057	0.14	1.468	0.037
-0.82	2.388	0.056	0.18	1.487	0.037
-0.78	2.308	0.054	0.22	1.421	0.036
-0.74	2.278	0.053	0.26	1.473	0.037
-0.70	2.114	0.049	0.30	1.564	0.039
-0.66	2.002	0.047	0.34	1.565	0.039
-0.62	1.983	0.047	0.38	1.643	0.040
-0.58	1.924	0.046	0.42	1.669	0.041
-0.54	1.788	0.043	0.46	1.799	0.043
-0.50	1.751	0.042	0.50	1.794	0.043
-0.46	1.687	0.041	0.54	1.846	0.044
-0.42	1.687	0.041	0.58	2.107	0.049
-0.38	1.547	0.038	0.62	2.193	0.051
-0.34	1.548	0.039	0.66	2.246	0.051
-0.30	1.475	0.037	0.70	2.252	0.052
-0.26	1.507	0.038	0.74	2.419	0.055
-0.22	1.457	0.037	0.78	2.518	0.058
-0.18	1.430	0.036	0.82	2.754	0.062
-0.14	1.387	0.035	0.86	2.681	0.060
-0.10	1.499	0.037	0.90	2.641	0.061
-0.06	1.411	0.036	0.94	2.560	0.061
-0.02	1.433	0.036	0.98	2.339	0.061

Table 10: Acceptance corrected angular distribution of the K^+ in the CMS, normalized to the total cross section 23.9 [μb].

$\cos(\theta_{K^+}^{CMS})$	$d\sigma/d\Omega$ [$\mu\text{b}/\text{sr}$]	error	$\cos(\theta_{K^+}^{CMS})$	$d\sigma/d\Omega$ [$\mu\text{b}/\text{sr}$]	error
-0.98	2.062	0.062	0.02	1.938	0.044
-0.94	1.451	0.045	0.06	1.902	0.044
-0.90	1.432	0.043	0.10	1.870	0.043
-0.86	1.636	0.046	0.14	1.812	0.042
-0.82	1.783	0.048	0.18	1.799	0.043
-0.78	1.934	0.049	0.22	1.718	0.041
-0.74	1.796	0.046	0.26	1.769	0.042
-0.70	2.013	0.049	0.30	1.810	0.043
-0.66	2.001	0.048	0.34	1.742	0.042
-0.62	2.086	0.050	0.38	1.849	0.044
-0.58	2.032	0.049	0.42	1.807	0.042
-0.54	2.132	0.049	0.46	1.864	0.044
-0.50	2.140	0.050	0.50	1.881	0.045
-0.46	2.132	0.049	0.54	1.864	0.044
-0.42	2.088	0.049	0.58	1.935	0.046
-0.38	2.014	0.047	0.62	1.864	0.045
-0.34	2.108	0.048	0.66	1.907	0.045
-0.30	2.059	0.047	0.70	1.930	0.046
-0.26	2.077	0.048	0.74	1.957	0.046
-0.22	2.001	0.047	0.78	1.995	0.047
-0.18	2.054	0.047	0.82	2.027	0.047
-0.14	2.022	0.047	0.86	1.937	0.046
-0.10	1.932	0.045	0.90	1.924	0.046
-0.06	2.005	0.046	0.94	1.774	0.044
-0.02	1.943	0.046	0.98	1.284	0.038

Table 11: Analyzing power A_N of K^+ as a function of the K^+ polar angle in the CMS.

$\cos(\theta_{K^+}^{CMS})$	A_N	error	$\cos(\theta_{K^+}^{CMS})$	A_N	error
-0.875	0.081	0.015	0.125	0.081	0.012
-0.625	0.174	0.013	0.375	0.062	0.013
-0.375	0.153	0.012	0.625	-0.008	0.012
-0.125	0.142	0.012	0.875	-0.050	0.013

Table 12: Analyzing power A_N of proton as a function of the proton polar angle in the CMS.

$\cos(\theta_p^{CMS})$	A_N	error	$\cos(\theta_p^{CMS})$	A_N	error
-0.875	0.023	0.011	0.125	-0.084	0.014
-0.625	-0.022	0.012	0.375	-0.079	0.014
-0.375	-0.066	0.013	0.625	-0.016	0.013
-0.125	-0.068	0.014	0.875	0.033	0.012

Table 13: Analyzing power A_N of Λ as a function of the Λ polar angle in the CMS.

$\cos(\theta_\Lambda^{CMS})$	A_N	error	$\cos(\theta_\Lambda^{CMS})$	A_N	error
-0.875	-0.018	0.012	0.125	0.002	0.014
-0.625	-0.069	0.012	0.375	0.009	0.013
-0.375	-0.096	0.013	0.625	0.009	0.012
-0.125	-0.055	0.014	0.875	0.051	0.012

Acronyms

ADC	Analog to Digital Converter
CMS	Center of Mass System
COSY	COoler SYnchrotron
COSY-TOF	COSY-TOF Detector
DIRC	Detection of Internally Reflected Cherenkov
EMC	ElectroMagnetic Calorimeter
FAIR	Facility for Antiproton and Ion Research
FS	Forward Spectrometer
FSI	Final State Interaction
FT	Forward Tracker
GEM	Gas Electron Multiplier
HESR	High Energy Storage Ring
MCP PMT	Micro Channel Plate Photo Multiplier
MDT	Mini Drift Tube
MVD	Micro Vertex Detector
PANDA	antiProton Annihilation at Darmstadt
PID	Particle IDentification
RICH	Ring Imaging CHerenkov
SQT	Silicon Quirl Telescope
STT	Straw Tube Tracker
TDC	Time to Digital Converter
TOF	Time Of Flight
TOT	Time Over Threshold
TS	Target Spectrometer

Bibliography

- [1] G. Charpak *et al.*, “The use of multiwire proportional counters to select and localize charged particles”, *Nucl. Instr. and Meth.* **62** (1968) 262-268.
- [2] E. Abat *et al.*, “The ATLAS transition radiation tracker (TRT) proportional drift tube: design and performance”, *Journal of Instrumentation* **3** (2008). DOI: 10.1088/1748-0221/3/02/P02013
- [3] P.R. Barbosa *et al.*, “LHCb outer tracker technical design report”, CERN/LHCC 2001-024, LHCb TDR 6 (2001).
- [4] The FAIR official website: http://www.fair-center.eu/no_cache.html
- [5] PANDA Collaboration, “Technical design report for the PANDA tracking system of PANDA experiment”, (2011). <http://www-panda.gsi.de/html/reports.php>
- [6] J. Smyrski, “Overview of the PANDA experiment”, *Physics Procedia* **37** (2012) 85-95.
- [7] PANDA collaboration, “Technical progress report for PANDA strong interaction studies with antiprotons”, (2005). http://www-panda.gsi.de/archive/public/panda_tpr.pdf
- [8] PANDA official website, <http://www-panda.gsi.de/>
- [9] PANDA collaboration, “Targets Technical Design Report of PANDA experiment”, (2012). <http://www-panda.gsi.de/html/reports.php>
- [10] PANDA Collaboration, “Technical design report for the PANDA Straw Tube Tracker”, *Eur. Phys. J. A* **49** (2013) 25. DOI: 10.1140/epja/i2013-13025-8
- [11] L. Zotti on behalf of the PANDA-MVD Group, “The Micro-Vertex Detector for the PANDA experiment”, *J. Phys. Conf. Ser.* **426** (2013).

- [12] P. Wintz for the COSY-TOF collaboration, “A large tracking detector in vacuum consisting of self-supporting straw tubes”, *American Institute of Physics Conf. Proc.* **698** (2004) 789. <http://dx.doi.org/10.1063/1.1664352>
- [13] P. Gianotti, S. Jowzaee *et al.*, “The Straw Tube Trackers of the PANDA Experiment”, *IEEE Xplore publication*, (2013). arXiv:1307.4537v1
- [14] A. Neiser *et al.*, “TRB3: A 264 channel high precision TDC platform and its applications”, <http://indico.cern.ch/event/228972/session/9/contribution/27/material/poster/0.pdf>
- [15] P. Wintz, “The central straw tube tracker in the PANDA experiment”, *Hyperfine Interactions* (2014). DOI: 10.1007/s10751-014-1035-6
- [16] <http://en.wikipedia.org/wiki/ASIC>
- [17] S. Jowzaee *et al.*, “Particle identification using the time-over-threshold measurements in straw tube detectors”, *Nucl. Instr. and Meth. A* **718** (2013) 573–574.
- [18] http://en.wikipedia.org/wiki/Low-voltage_differential_signaling
- [19] A. Ucar, “Developments for the TOF straw tracker”, PhD Dissertation, University of Bonn (2006).
- [20] F. Sauli, “Principles of Operation of Multi-wire Proportional and Drift Chambers”, CERN European Organization for Nuclear Physics (1977).
- [21] K. Nakamura *et al.*, “Passage of particles through matter”, *J. Phys. G* **37**, 075021 (2010). pdg.lbl.gov/2011/reviews/rpp2011-rev-passage-particles-matter.pdf
- [22] A. Sharma, “Properties of some gas mixtures used in tracking detectors”. *SLAC-JOURNAL-ICFA* **16-3**.
- [23] W. Blum, W. Riegler and L. Rolandi, “Particle detection with drift chambers”, Springer-Verlag Berlin Heidelberg (2008).
- [24] B.J. Arnold, “An affordable particle detector for education”, Bristol University (2005).
- [25] R. Veenhof, “Choosing a gas mixture for the ALICE TPC”, European organization for nuclear research, ALICE-INT-2003-29 version 1.0, (2003).

- [26] GARFIELD program webpage, <http://garfield.web.cern.ch/garfield/>
- [27] Magboltz program webpage, <http://magboltz.web.cern.ch/magboltz/>
- [28] Heed program webpage, <http://heed.web.cern.ch/heed/>
- [29] R.Y. Pal, H.W. Ellis and E.W. McDaniel. “Transport properties of gaseous ions over a wide energy range”, *At. Data and Nucl. Data Tables* **17** (1976) 177-210.
- [30] P. Cwetanski, “Straw performance studies and quality assurance for the ATLAS transition radiation tracker”, PhD Dissertation, University of Helsinki (2006).
- [31] O. Sahin *et al.*, “Penning transfer in argon-based gas mixtures”, *Journal of Instrumentation* **5** (2010).
- [32] A. Kashchuk *et al.*, “Measurement of the absolute gas gain and the gain variations study in straw-tube detectors”, Laboratori Nazionali di Frascati (2011). [https://www.lnf.infn.it/sis/preprint/pdf/getfile.php?filename=LNF-11-5\(P\).pdf](https://www.lnf.infn.it/sis/preprint/pdf/getfile.php?filename=LNF-11-5(P).pdf)
- [33] M. Deptuch, “Mnozenia lawinowe elektronow w licznickach proporcjonalnych wypelnionych mieszanina na bazie Ar + CO₂”, Diploma Thesis, Akademia Gorniczo-Hutnicza im. Stanislawia Staszica w Krakowie (2001).
- [34] T. Akesson *et al.*, “Particle identification using the time-over-threshold method in the ATLAS Transition Radiation Tracker”, *Nucl. Instr. and Meth. A* **474** (2001) 172-187.
- [35] A. Manara, “Particle identification using time-over-threshold measurements in the ATLAS Transition Radiation Tracker”, PhD Dissertation, Indiana University (2000).
- [36] M. Traxler *et al.*, “TRBv2: A platform for miscellaneous DAQ/TDC tasks for HADES and FAIR-experiments”, *Instruments-Methods-55*, <http://www-alt.gsi.de/informationen/wti/library/scientificreport2007/PAPERS/INSTRUMENTS-METHODS-55.pdf>
- [37] E. Nappi, “Advances in charged particle identification techniques”, *Nucl. Instr. and Meth. A* **628** (2011) 1-8.

- [38] K.Th. Brinkmann, “Physics program at COSY”, *11th International Conference on Meson-Nucleon Physics and the Structure of the Nucleon*, Forschungszentrum Jülich, Germany (2007).
- [39] R. Maier *et al.*, “Cooler synchrotron COSY”, *Nucl. Phys. A* **626** (1997) 395-403.
- [40] A. Kacharava, “Physics program at COSY-Jülich with polarized hadronic probes”. http://collaborations.fz-juelich.de/ikp/anke/proceedings/Andro_Kacharava.pdf
- [41] R. Maier, “Cooler synchrotron COSY-performance and perspectives”, *Nucl. Instr. and Meth. A* **390** (1997) 1-8.
- [42] http://www.fz-juelich.de/ikp/EN/Forschung/Beschleuniger/_doc/COSY.html
- [43] D. Grzonka and K. Kilian, “Applications and potential of COSY in the field of strangeness”, *Nucl. Phys. A* **639** (1998) 569c-577c.
- [44] D. Grzonka and K. Kilian, “Experiments at COSY”, *Nucl. Phys. A* **670** (2000) 241c-248c.
- [45] U. Bechstedt *et al.*, “The cooler synchrotron COSY in Jülich”, *Nucl. Instr. and Meth. B* **113** (1996) 26-29.
- [46] J. Dietrich *et al.*, “Status of the cooler synchrotron COSY-Jülich and future plans”, *Proceeding of RuPAC XIX*, Dubna (2004). <http://www.jinr.dubna.su/RuPAC2004/>; <http://accelconf.web.cern.ch/AccelConf/r04>
- [47] H. Stockhorst *et al.*, “The cooler synchrotron COSY facility”, *IEEE* (1998). cern.ch/AccelConf/pac97/papers/pdf/7W023.PDF
- [48] D. Prasuhn *et al.*, “Status of the cooler synchrotron COSY Jülich”, *Particle Accelerator Conference*, Chicago, USA (2001). DOI: 10.1109/PAC.2001.988107
- [49] H. Stockhorst *et al.*, “The medium energy proton synchrotron COSY”, *Proceeding of EPAC*, Vienna, Austria (2000). <http://accelconf.web.cern.ch/accelconf/e00/PAPERS/MOP4B19.pdf>
- [50] H. Machner, “Recent physics at COSY-a review”, *J. Phys.* **66-5** (2006) 867-876.

- [51] D. Grzonka and K. Kilian, “Future physics program at COSY”. http://theory.gsi.de/hirscheegg/2001/Proceedings/Kilian_134.94.100.100_hirscheegg01.pdf
- [52] S. Abdel-Samad *et al.*, “Hyperon production in the channel $pp \rightarrow pK^+\Lambda$ near the reaction threshold”, *Phys. Lett. B* **632** (2006) 27-34.
- [53] R. Bilger *et al.*, “Strangeness production in the reaction $pp \rightarrow pK^+\Lambda$ in the threshold region”, *Phys. Lett. B* **420** (1998) 217.
- [54] S. Abd El-Samad *et al.*, “Influence of N^* -resonances on hyperon production in the channel $pp \rightarrow pK^+\Lambda$ at 2.95, 3.20 and 3.30 GeV/ c beam momentum”, *Phys. Lett. B* **688** (2010) 142-149.
- [55] The COSY-TOF Collaboration, “Strangeness Physics at COSY-TOF-A proposed program to Investigate Nucleon Resonances and the Hyperon-Nucleon Interaction”, Forschungszentrum Jülich (2007).
- [56] R. Dzhygadlo, “Differential cross section distribution and polarization observables in the reaction $pp \rightarrow pK^0\Sigma^0$ at $p = 2.95$ GeV/ c ”, PhD Dissertation, University of Bonn (2012).
- [57] M. Roeder, “Final state interaction and polarization variables in the reaction $pp \rightarrow pK^+\Lambda$ ”, PhD Dissertation, University of Bochum (2011).
- [58] C. Pizzolotto, “Measurement of Λ polarization observables at the COSY-TOF spectrometer”, PhD Dissertation, University of Erlangen-Nürnberg (2007).
- [59] C. Pizzolotto, “Measurement of Λ polarisation observables at the COSY-TOF spectrometer”, PhD Dissertation, Friedrich-Alexander-University (2007).
- [60] S. Abdel-Samad, M. Abdel-Bary and K. Kilian, “New developments in cryo-target for the external COSY experiments”, *Nucl. Instr. and Meth. A* **495** (2002) 1-7.
- [61] F. Hauenstein, “Proton-Lambda final state interaction and polarization observables measured in the $\vec{p}p \rightarrow pK^+\Lambda$ reaction at 2.7 GeV/ c beam momentum”, PhD Dissertation, University of Erlangen-Nürnberg (2014).
- [62] S. Marcello *et al.*, “Associated strangeness production at threshold”, *Nucl. Phys. A* **691** (2001) 344c-352c.

- [63] A. Boehm *et al.*, “The COSY-TOF barrel detector”, *Nucl. Instr. and Meth. A* **443** (2000) 238-253.
- [64] M. Dahmen *et al.*, “A three layer circular scintillator hodoscope”, *Nucl. Instr. and Meth. A* **348** (1994) 97-104.
- [65] K. Ehrhardt, “Measurement of the reaction $pp \rightarrow pK^+\Lambda$ and its analysis with a new analysis program: typeCase”, PhD Dissertation, University of Tuebingen (2011).
- [66] http://en.wikipedia.org/wiki/Archimedean_spiral
- [67] <http://www.fz-juelich.de/ikp/EN/Forschung/ExperimentelleEntwicklungen/DriftrohrKammern/DriftrohrKammern.html>
- [68] K. Nuenighoff *et al.*, “A light straw tracker detector working in vacuum”, *Nucl. Instr. and Meth. A* **477** (2002) 410-413.
- [69] S. Jowzaee, “Calibration of the COSY-TOF Straw-Tube-Tracker”, Annual report 2012 Jülich Center for Hadron Physics and Institute for Kernphysik (IKP), Forschungszentrum Jülich, (2012). <http://www.fz-juelich.de/ikp/EN/Aktuelles/ar2012.html>
- [70] P. Voigtländer, “Kalibration des COSY-TOF Straw-Tube-Tracker”, Diploma Thesis, Ruhr-University of Bochum (2009).
- [71] S. Jowzaee, “Improvement in position and spatial resolution determination of the COSY-TOF Straw-Tube-Tracker”, Annual report 2013 Jülich Center for Hadron Physics and Institute for Kernphysik (IKP), Forschungszentrum Jülich, (2013). <http://www.fz-juelich.de/ikp/EN/Aktuelles/ar2013.html>
- [72] S. Jowzaee for the COSY-TOF collaboration, “Calibration of a Straw-Tube-Tracker for the COSY-TOF experiment”, *Acta Physica Polonica B* **6** (2013) 1067-1071.
- [73] A. Sibirtsev *et al.*, “Resonances and final state interactions in the reaction $pp \rightarrow pK^+\Lambda$ ”, *Eur. Phys. J. A* **27** (2006) 269-285.
- [74] J.M. Laget, “Strangness production in nucleon-nucleon collisions”, *Phys. Lett. B* **259** (1991) 24-28.
- [75] R. Siebert *et al.*, “High resolution study of hyperon-nucleon interactions by associated strangeness production in pp collisions”, *Nucl. Phys. A* **567** (1994) 819.

- [76] O. Grebenyuk *et al.*, “Total cross section of the $pp \rightarrow pK^+\Lambda$ reaction near threshold”, (2007). arXiv:0710.2249
- [77] COSY-TOF Collaboration, tof++ software, COSY-TOF Internal Note, Jülich (2006).
- [78] ROOT program webpage, <http://root.cern.ch/drupal/>
- [79] F. James and M. Roos, “Minuit: A System for Function Minimization and Analysis of the Parameter Errors and Correlations”, *Comput. Phys. Commun.* **10** (1975) 343-367.
- [80] R.O. Duda and P.E. Hart, “Use of the Hough transformation to detect lines and curves in pictures”, *Communications of the ACM* **15**, 1 (1972) 11-15.
- [81] B.E. Bonner *et al.*, “Spin parameter measurements in Λ and KS production”, *Phys. Rev. D* **38**, 3 (1988) 729-741.
- [82] SAID data base, www.gwdac.phys.gwu.edu/analysis/nn-analysis.html
- [83] K. Nakamura *et al.*, “Review of Particle Physics”, *J. Phys. G* **37** (2010).
- [84] M. Roeder *et al.*, “Final-state interactions in the process $pp \rightarrow pK^+\Lambda$ ”, *Eur. Phys. J. A* **49**, 157 (2013).
- [85] S. Abd El-Samad *et al.*, “On the ΣN cusp in the $pp \rightarrow pK^+\Lambda$ reaction”, *Eur. Phys. J. A*, **49** (2013) 41. DOI: 10.1140/epja/i2013-13041-8
- [86] M. Abdel-Bary *et al.*, “Production of Λ and Σ^0 hyperons in proton-proton collisions”, *Eur. Phys. J. A* **46** (2010) 27-44.
- [87] E. Byckling and K. Kajantie, “Particle Kinematics”, John Wiley & Sons (1973).
- [88] H. Machner *et al.*, “Study of the Λp interaction close to the Σ^+n and Σ^0p thresholds”, *Nucl. Phys. A* **901** (2013) 65-88. DOI: 10.1016/j.nuclphysa.2013.01.031
- [89] A. Budzanowski *et al.*, “Upper limits for a narrow resonance in the reaction $pp \rightarrow K^+ + (\Lambda p)$ ”, *Phys. Rev. D*, **84** (2011) 032002. DOI: 10.1103/PhysRevD.84.032002
- [90] A. Gasparyan *et al.*, “How to extract the ΣN scattering length from production reactions”, *Phys. Rev. C* **69** (2004) 034006.